Eidgenössische Technische Hochschule Zürich
Swiss Federal Institute of Technology Zurich

UNIS
The University Centre in Svalbard

Master Thesis

Department of Earth Sciences, ETH Zürich
Institute for Atmospheric and Climate Science

Department of Arctic Geology
The University Centre in Svalbard

Aerodynamic Roughness Length of Crevassed Tidewater Glaciers from UAV Mapping

Submitted by:
Armin Dachauer
armind@student.ethz.ch
15-710-551

First Supervisor:
Dr. Richard Hann
Department of Engineering
Cybernetics, NTNU

Second Supervisor:
Prof. Dr. Andy Hodson
Arctic Geology Department
The University Centre in Svalbard
UNIS

Third Supervisor:
Dr. Andreas Bauder
Laboratory of Hydraulics,
Hydrology and Glaciology
ETH Zürich

October 29, 2020
Zürich

Abstract

The aerodynamic roughness length (z_0) is an important parameter in the bulk approach to calculate turbulent fluxes and thereof glacial surface ice melt. However, for heavily crevassed tidewater glaciers, which are very common in Svalbard, z_0 estimations are rare or only generalized. This study used unmanned aerial vehicles (UAVs), which proved to be a cheap and reliable tool to map inaccessible tidewater glacier front areas. The applied structure-from-motion photogrammetry approach successfully managed to build digital elevation models (DEMs) out of the high-resolution UAV images using Agisoft Metashape. These DEMs were used by five different models (split in transect and raster methods) to estimate z_0 values of the mapped area. The results point out that the range of z_0 values across a glacier is large, with up to three (locally even four) orders of magnitude. The division of the mapped area into subareas (50 m x 50 m), each producing one z_0 value, takes into account the high spatial variability of z_0 across the glacier. The z_0 estimations from the transect method are in general higher (up to one order of magnitude) than the raster method estimations. Furthermore, wind direction (values parallel to ice flow direction are larger than perpendicular) and the chosen subarea grid size turned out to have a large impact on the z_0 values, again presenting a range of up to one order of magnitude each. In average, on all glaciers and for all models z_0 values between 0.08 m and 0.88 m for a down-glacier wind direction could be found. A simple energy balance model revealed that the larger z_0 values of heavily crevassed tidewater glaciers increase the surface ice melt by almost 20 % compared to an average smooth glacier.

Table of Contents

Abstract i

Table of Contents ii

Nomenclature and Abbreviations iv

1 Motivation 1

1.1 Importance of Aerodynamic Roughness Length . . . 2

1.2 Aim of Thesis . . . 4

2 Data and Methods 5

2.1 Field Sites . . . 5

2.2 Field Data Collection . . . 7

2.3 Building Digital Elevation Models . . . 10

2.3.1 Structure-from-Motion and Multi-View Stereo . . . 10

2.3.2 Parameter Settings of Agisoft Metashape . . . 11

2.3.3 Georeferencing, Drone Type and Weather . . . 15

2.4 Data Preparation for Model Calculation . . . 16

2.5 Model Calculation of Aerodynamic Roughness Length . . . 18

2.5.1 Transect Method . . . 19

2.5.2 Raster Method . . . 22

2.6 Surface Energy Balance Model . . . 25

3 Results 27

3.1 Digital Elevation Models . . . 27

3.1.1 Validation of Digital Elevation Model Accuracy . . . 29

3.2 Aerodynamic Roughness Length . . . 32

3.2.1 Model Variability . . . 33

3.2.2 Glacier Variability . . . 36

3.2.3 Wind Direction Dependency . . . 38

3.2.4 Grid Size Dependency of Subarea . . . 40

3.2.5 Temporal Variability on Nordenskiöldbreen between 2019 and 2020 . . . 43

3.2.6 Characteristic Surface Features . . . 45

3.3 Surface Energy Balance Model . . . 48

4 Discussion **49**
4.1 Digital Elevation Models 49
4.2 Aerodynamic Roughness Length 51
4.2.1 Variability of Aerodynamic Roughness Length across the Glacier 51
4.2.2 Evaluation of Model Calculations 54
4.2.3 Scale Dependency of Aerodynamic Roughness Length 57
4.3 Surface Energy Balance Model 58

5 Conclusion and Outlook **60**
5.1 Conclusion 60
5.2 Outlook 61

Acknowledgements **63**

References **68**

Appendix A Agisoft Metashape Processing Parameters **I**

Appendix B Digital Elevation Models **XII**

Appendix C Aerodynamic Roughness Length **XIV**

Declaration of Originality **XXV**

Nomenclature

α_e	Stability correction constant for humidity
α_H	Stability correction constant for heat
α_M	Stability correction constant for momentum
λ	Latent heat of vaporization [J kg^{-1}]
ω	Ratio of molecular weight of water vapour to air
Ω	Anisotropy ratio
ρ	Air density [kg m^{-3}]
σ	Standard deviation
$\wedge$	Monin-Obukhov length scale for sensible heat flux [m]
c_d	Drag coefficient
c_p	Specific heat capacity of air [J kg^{-1} K^{-1}]
e_s	Vapour pressure at glacier surface [Pa]
e_z	Vapour pressure at height z [Pa]
f	Zero-up-crossing frequency above mean transect elevation
h^*	Effective obstacle height [m]
i	Column number
j	Row number
k	Von Kármán constant
L	Monin-Obukhov length scale for latent heat flux [m]
P	Atmospheric pressure [Pa]
s	Frontal area of obstacle [m^2]
S	Horizontal ground area of obstacle [m^2]
T_z	Temperature at height z [°C]
u_z	Wind speed at height z [m/s]
X	Profile length [m]
z	Elevation [m]
z_0	Aerodynamic roughness length [m]
z_d	Displacement height [m]
z_e	Humidity scaling length [m]
z_t	Temperature scaling length [m]

Abbreviations

DCI	Debris-covered ice
DEM	Digital elevation model
FB	Tidewater glacier Fridtjovbreen
GCP	Ground control point
GNSS	Global navigation satellite system
GPS	Global positioning system
GSD	Ground sampling distance
HB	Tidewater glacier Heuglinbreen
HC	Heavily crevassed
IQR	Inter-quantile range
LHF	Latent heat flux
LiDAR	Light detection and ranging
LWR	Longwave radiation
MLT	Surface melt rate
MVS	Multi-view stereo
MWC	Melt water channel
NSB	Tidewater glacier Nordenskiöldbreen
NTNU	Norwegian University of Science and Technology
PPK	Post-processed kinematic
RTK	Real-time kinematic
SC	Slightly crevassed
SfM	Structure-from-motion
SHF	Sensible heat flux
Std	Standard deviation
SWR	Shortwave radiation
TB	Tidewater glacier Tunabreen
UAV	Unmanned aerial vehicle

Chapter 1

Motivation

About 57 % of Svalbard's land area is covered by glaciers (Nuth et al., 2013) of various types as ice caps, tidewater glaciers or cirque glaciers (Schuler et al., 2020). However, large parts of the glacierized area of Svalbard is draining through tidewater glaciers (Nuth et al., 2013). Tidewater glaciers are defined by flowing into the sea, terminating in an ice cliff and by loosing most of their mass through calving (Van Der Veen, 1996). According to an analysis of Błaszczyk et al. (2009), still 163 glaciers in Svalbard have contact with the ocean, corresponding to about 60 % of all glaciers (by area). As calving of icebergs accounts for a substantial part of ice mass loss on the archipelago (Mansell et al., 2012), tidewater glaciers are important for the mass budget of Svalbard's glaciers (Luckman et al., 2015). The terminus area of tidewater glaciers is often heavily crevassed (see Figure 1.1). Crevasses result from strain and thus are visible manifestations of stresses within the ice (Colgan et al., 2016). On tidewater glaciers, the crevasses are usually located perpendicular to the flow direction. The closer the ice gets to the terminus, the larger the longitudinal gradient of the flow velocity. This leads to larger tensile stresses and more crevasses (Błaszczyk et al., 2009).

The surface characteristics of glaciers (including crevasses) are of primary importance to their mass balance (Arnold and Rees, 2003). The surface of crevassed ice is rougher compared to glaciers without crevasses. One the one hand this roughness leads to a larger exposed surface area and on the other hand to more turbulence when the wind is blowing over the surface (Hann et al., 2019). The aerodynamic roughness of a glacier's surface influences the turbulent heat exchange between the glacier surface and the atmosphere (Rees and Arnold, 2006). Both sensible and latent heat fluxes (referred to as turbulent fluxes (Smith et al., 2020)) balance this heat exchange on the surface and therefore have a large impact on the meltwater production and the surface energy balance of glaciers (Hock, 2005). Turbulent fluxes are driven by the temperature and moisture gradient between air and ice (Hock, 2005). Therefore, rising air temperatures, that come along with climate change, increase the contribution of turbulent fluxes to ice surface mass loss due to a larger temperature gradient. This leads to an acceleration of ice melting (Braithwaite and Olesen, 1990). However, there are intrinsic properties of the crevassed ice that strongly limit our understanding of the turbulent heat transfer between the atmosphere and the ice surface (Colgan et al., 2016). Moreover, atmospheric conditions above the glacier surface are usually very complex (Rees and Arnold, 2006). Accordingly, a proper understanding of the key influences on turbulent fluxes is crucial (Smith et al., 2016b) for reducing uncertainties in future predictions of surface ice melt on glaciers and ice sheets (Fausto et al., 2016). The purpose of this study is to improve the estimation of turbulent fluxes and surface ice melt on crevassed tidewater glaciers by providing spatially distributed aerodynamic roughness length values of such glacier areas.

Figure 1.1: Drone picture of heavily crevassed tidewater glacier Nordenskiöldbreen. Photo taken by Richard Hann.

1.1 Importance of Aerodynamic Roughness Length

Any model calculating the melt of ice which considers turbulent fluxes and is not using any eddy covariance approach, has to incorporate one or several values for the aerodynamic roughness length (Chambers et al., 2020). The aerodynamic roughness length, also called z_0, is a length scale that represents the height above the surface at which the wind speed drops to zero (Chappell and Heritage, 2007). It is a constant surface characteristics (Lettau, 1969) describing the loss of wind momentum that can be attributed to surface roughness (Smith, 2014). Its significance is that it can be used as a control on the rate of turbulent heat exchange between the glacier's surface and the atmosphere (Cuffey and Paterson, 2010).

There exist three main methods to calculate turbulent fluxes (Chambers et al., 2020). First, the eddy correlation method that uses sonic anemometers to record the air movement in turbulent eddies. Second, the profile method that estimates the turbulent fluxes by interpolating near-surface wind speed profiles. And third, the bulk approach that for its calculation only requires the atmospheric measurements of a basic meteorological station (e.g. wind speed, temperature) and z_0 values which can be obtained by microtopographic measurements (Chambers et al., 2020). In other words, for the bulk approach the sensible and latent heat flux can be approximated by the potential temperature and the specific humidity. These two terms can again be derived by exchange coefficients using the aerodynamic roughness length (Hock, 2005). However, direct eddy correlation and wind profile measurements (first and second method) are usually hard to obtain, because the measurement instruments are difficult to set up and maintain in heavily crevassed glacier environments (Chambers et al., 2020). Also for the bulk method measurements are needed, but they can be set up further upstream or on a location close by. Therefore, the bulk aerodynamic method is a very popular approach due to its low requirements for data collection (Chambers et al., 2020).

Recently, a series of studies based on the bulk approach have been conducted to find methods to determine z_0 values of glacier surfaces (e.g. Irvine-Fynn et al., 2014; Miles et al., 2017; Smith et al., 2016b). All of them used digital elevation models (DEM) as a data source for their calculation.

The potential for using photogrammetry methods to produce DEMs also in the field of glaciology is not new (e.g Baltsavias et al., 2001), but is increasingly perceived recently and has become one of the major methods to do so (Uysal et al., 2015). In glaciology, DEMs are often utilized to determine ice-volume changes comparing two DEMs captured at different times (e.g. Bauder et al., 2007). However, in this thesis we focus on the usage of DEMs to estimate the aerodynamic roughness length of glaciers. Whereas airborne Light Detection and Ranging (LiDAR) systems constitute a powerful way to effectively produce DEMs, their large disadvantage is that they are very expensive (Uysal et al., 2015) and their spatial resolution is limited (Bhardwaj et al., 2016). Terrestrial LiDAR systems (used for instance in the studies of Smith et al. (2016b), Nicholson et al. (2016) or Nield et al. (2013a)), on the other hand are limited in the area they cover (Irvine-Fynn et al., 2014). Several studies used a photogrammetry approach based on pictures taken from the ground (e.g. Irvine-Fynn et al., 2014; Miles et al., 2017; Quincey et al., 2017). Thus, the mapped area is often restricted in size and the mapped roughness obstacles accordingly small. However, unmanned aerial vehicles (UAVs) provide a cheap alternative to overcome these limitations (Uysal et al., 2015). Especially, since the observed crevasses in this thesis are large-scale roughness obstacles rather than small-scale obstacles as investigated in many studies before (e.g. Irvine-Fynn et al., 2014; Nield et al., 2013a).

In recent years, UAVs have presented new opportunities for detailed mapping of earth surface and became more and more popular. Especially in glaciology it is increasingly used as an alternative to field studies (Bhardwaj et al., 2016). In Svalbard and the polar region in general, UAVs were first applied in 2007 on a study of Midtre Lovenbreen conducted by Hodson et al. (2007). The main advantage of UAVs is the possibility of collecting high temporal and spatial resolution data at low costs (Casella and Franzini, 2016). In other words, UAV-based remote sensing has the capability to overcome the gap between sparse field observations on the one side and coarse resolution space-born remote sensing data on the other side (Bhardwaj et al., 2016). Therefore, UAVs provide a good possibility to study the direct effect of crevasses on turbulent heat transfer on glacier surfaces. Accordingly, the thesis follows an approach where UAVs provide large amounts of high-resolution topographic data which then is used to build DEMs and estimate z_0 values which take into account the spatial variability of a glacier's surface roughness. Alternatively, drones could also be used to directly measure wind profiles and thereof estimate z_0 values as done in a parallel master thesis project by Garreau (2020).

Several studies already investigated the z_0 values of non-crevassed (Irvine-Fynn et al., 2014; Nield et al., 2013a), debris-covered (Quincey et al., 2017) or sparsely crevassed (Smith et al., 2016b) ice surfaces using different approaches. However, still little is known about the effect of heavily crevassed glacier areas on the turbulent heat exchange between glaciers and the atmosphere. The greatly varying size of obstacles (i.e. crevasses) and the broader-scale, heterogeneous surface topography of such crevassed ice makes it hard to define z_0 values (Quincey et al., 2017). In particular the ablation zone of glaciers contains many different surface roughness obstacles which influence the value of z_0 (Smith et al., 2016b). In other words, z_0 values of ice can vary a lot even across a small area and one ablation season (Smeets et al., 1999). Additionally, the direction of wind usually has an effect on z_0 values (Smith et al., 2016b). To conclude, there are several parameters such as detected roughness obstacle size, transect length or grid size of subarea whose sensitivity to z_0 model performance remain mostly unclear (Miles et al., 2017) and therefore need further investigation.

Typical values of z_0 on glacier ice range from 0.01 mm to 0.1 mm for smooth ice and 20 mm to 80 mm for rough glacier ice (Brock et al., 2006; Smeets et al., 1999). However, literature values for heavily crevassed glacier ice (as in Svalbard often found on tidewater glaciers) are rare. Table

Table 1.1: Published aerodynamic roughness length values for crevassed glacier areas.

Study	Method	Surface Type	z_0 (m)
Fitzpatrick et al. (2019)	Raster	Large crevasses	0.01-0.5
Obleitner (2000)	Transect	Very rough glacier ice	0.05
Smeets et al. (1999)	Transect	Very rough glacier ice	0.02-0.08
Smith et al. (2016b)	Transect	Deep crevasses	0.005-0.05
Smith et al. (2016b)	Raster	Deep crevasses	0.003-0.025

1.1 gives a closer overview of published aerodynamic roughness values for large/deep crevasses or rough glacier ice. The table shows that z_0 values of up to 0.5 m for large crevasses have been found (Fitzpatrick et al., 2019). Furthermore, most modelling studies so far only consider one single z_0 value for the whole glacier surface (commonly 1 mm (Smith et al., 2020)), regardless of any spatial and temporal variability (Quincey et al., 2017). In other words, spatially and temporally distributed z_0 values across the glacier are currently lacking in the parametrisation process of surface energy balance models (Smith et al., 2020). The aerodynamic roughness length is a key parameter for the calculation of turbulent fluxes (Chambers et al., 2020), because a change in z_0 by an order of magnitude can double the estimated turbulent fluxes (Brock et al., 2006; Munro, 1989). Therefore, an accurate approximation of z_0 especially in complex ice surfaces is crucial. In summary, the uncertainty in z_0 values presents a serious challenge for the calculation of surface ice melt (Smith et al., 2016b) and its correct parametrization is critical in surface energy balance studies (Quincey et al., 2017).

1.2 Aim of Thesis

The aim of this master thesis is to assess the application of UAVs for capturing high-resolution surveying images. A photogrammetry method is used to extract data from the aerial images and provide information about the shape of crevasses like depth, size and distribution. The data output of that processing is a DEM of the mapped glacier. These DEMs are then used to estimate the aerodynamic roughness length of crevassed tidewater glaciers in Svalbard. The following three research questions are investigated in this thesis:

1. How can drone-based topographic data be used to estimate the aerodynamic roughness length?
2. What range of aerodynamic roughness length values can be found on crevassed tidewater glaciers?
3. How do different aerodynamic roughness length values found on crevassed tidewater glaciers in Svalbard affect surface ice melt rates?

The main advantage of this approach is that drone data, which is increasingly available nowadays, can be used as a tool to build DEMs which then are utilized to estimate turbulent fluxes that are usually difficult to measure in the field. Furthermore, the chosen DEM approach allows glaciers to be divided into areas of different aerodynamic roughness length values, rather than estimating one generalized z_0 value for the whole mapped glacier. This leads to a better spatial representation of the turbulent fluxes on a glacier. The results of this thesis will also be used to show the impact of crevasses on the rate of surface ice melting using local climate data.

Chapter 2

Data and Methods

2.1 Field Sites

This thesis was written as a guest student at the University Centre in Svalbard (UNIS) and all the data was gathered on the arctic archipelago. Given the northern position of Svalbard, the mean temperature, especially during winter, is remarkably high due to the North Atlantic Current and frequent transport of milder air from lower latitudes (Liestøl, 1993). Thus, the climate in Svalbard is wetter and cloudier than usually found on this latitude. In general, a clear temperature and precipitation gradient can be observed across Svalbard. While the southwestern part of the archipelago is mild (annual temperature of about $-4°$) and wet (annual precipitation of up to 1200 mm), the northeastern part is colder ($-12°$) and drier (500 mm) (Hanssen-Bauer et al., 2019).

The goal of this thesis is to investigate the influence of crevasses on turbulent heat fluxes. Thus, only tidewater glaciers with a strongly crevassed terminus have been chosen as study sites. Moreover, only the terminus areas themselves were mapped with the drone as they are usually most crevassed and closest to access. A surveying of the whole glacier areas was impracticable due to the limited range of drone signal and battery capacity. Additionally, the tidewater glaciers were chosen in a way that they all could be visited and surveyed within one day from the settlement Longyearbyen. Therefore, all of them can be found in the central part of Spitzbergen, Svalbards main island (see Figure 2.1).

More than one glacier was surveyed in this thesis to apply our method to multiple object shapes and different crevasse widths. Thus, the high-resolution drone images were captured in three field campaigns (see Table 2.1). The first data was collected in summer 2019 on Nordenskiöldbreen in

Table 2.1: Overview of the visited tidewater glaciers with the exact location and the date of drone flight.

Glacier	Date	Location
Nordenskiöldbreen 2019	19.-22.08.2019	78°39'N, 17°00'E
Tunabreen	28.04.2020	78°27'N, 17°23'E
Heuglinbreen	04.05.2020	78°21'N, 18°47'E
Fridtjovbreen	07.05.2020	77°47'N, 14°31'E
Nordenskiöldbreen 2020	21.07.2020	78°39'N, 17°00'E

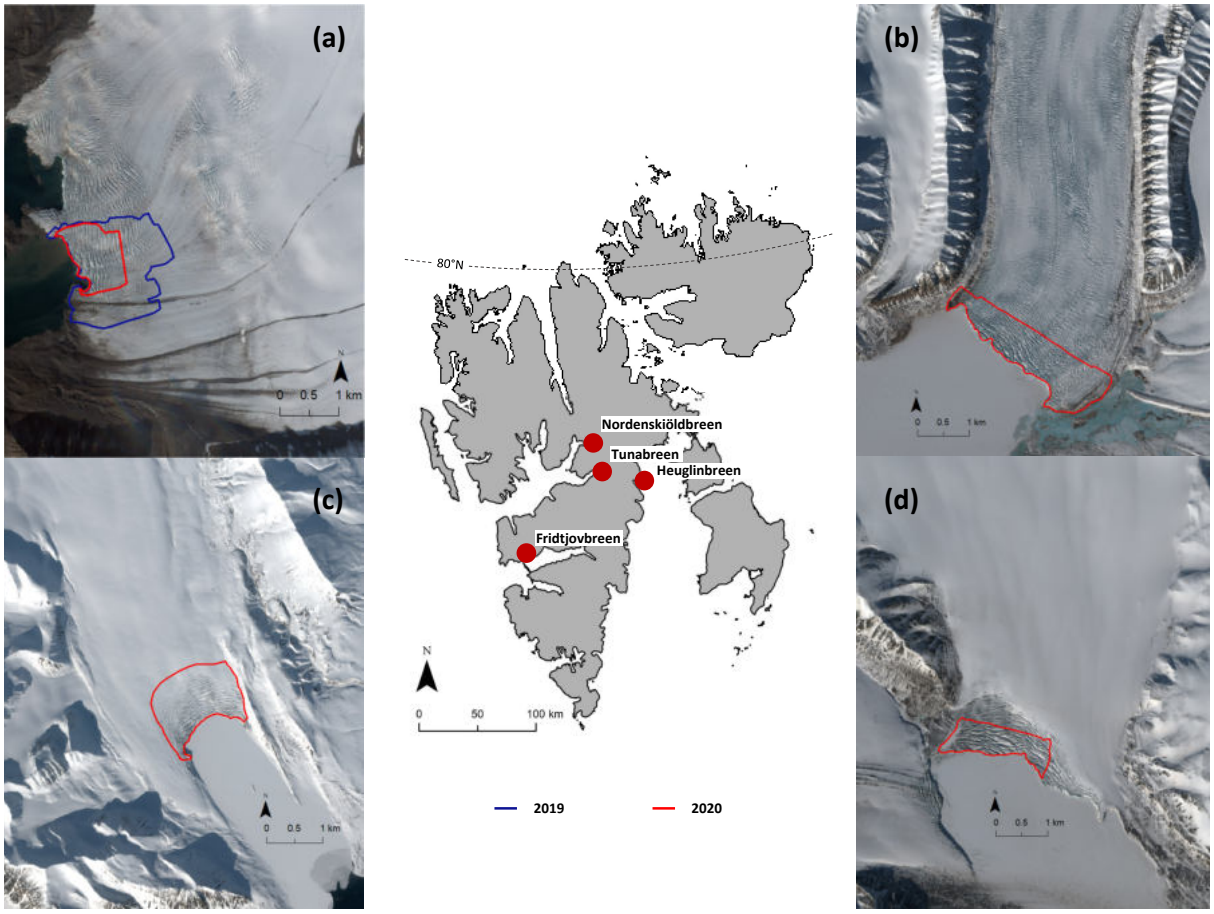

Figure 2.1: Field Sites: Map of Svalbard with marked locations of the investigated tidewater glaciers (red dots). Additionally, satellite images (ESA, 2020) of the glaciers Nordenskiöldbreen (a), Tunabreen (b), Fridtjovbreen (c) and Heuglinbreen (d) taken at the according week of fieldwork provide a closer look. The lines mark the mapped front area for each glacier in 2019 (blue) and 2020 (red).

a field campaign not related to this thesis (Hann et al., 2019). In spring 2020 further fieldwork was conducted in a second campaign on the following three glaciers (see Figure 2.1): Fridtjovbreen, Heuglinbreen and Tunabreen. All three glaciers were visited with snow scooters at the end of the snow season between end of April and beginning of May. Finally, Nordenskiöldbreen was visited a second time by boat in the third field campaign in July 2020 to get an impression of the temporal change of the aerodynamic roughness length.

With Tunabreen there was also a glacier investigated that recently surged. Surging glaciers are common in Svalbard, what makes it difficult to use the fluctuations of the glacier front as climatic indicators (Hagen et al., 1993). Tunabreen has normally a surging period of about 40 years and was surging in 2003-2005 (Flink et al., 2015). However, a bit more than 10 years later the glacier front advanced again what also was referred to as a surge (Ericson et al., 2019). At the time Tunabreen was visited for this thesis, it was not surging anymore.

Another difference between the glaciers is that Nordenskiöldbreen, Tunabreen and Heuglinbreen on one side are outlet glaciers of a large glacierized area northeast of Spitzbergen island. Fridtjovbreen on the other side is a single tidewater glacier of about 13 km length, flowing south-

Table 2.2: Specification of the two drones Phantom 4 Pro (DJI, 2017) and Mavic 2 Enterprise (DJI, 2019) used for fieldwork.

	Phantom 4 Pro	Mavic 2 Enterprise
Weight (g)	1388	899
Max. Flight Time (min)	30	31
Focal Length (mm)	8.8	4-6
Max. Image Size (px)	5472 x 3648	4000 x 3000

wards and terminating into Van Mijenfjorden. Thus, the glacier is located on the western side of Spitzbergen where precipitation and temperature are relatively high (Hanssen-Bauer et al., 2019). Both Nordenskiöldbreen and Tunabreen are outlet glacier from the large Lomonosovfonna ice cap, flowing from northeast to southwest. While Nordenskiöldbreen is a roughly 15 km long, wide tidewater glacier terminating in Billefjorden, Tunabreen is more narrow with a length of about 20km ending up in Tempelfjorden. Heuglinbreen is a tidewater glacier flowing southwards and still influenced by Hayesbreen that is flowing from a northwestern direction. The two retreating glaciers, both terminating into Mohnbukta, are about to separate. Mohnbukta is a bay in Storfjorden and actually part of the east cost of the Spitzbergen island. The east cost is known to be particularly cold and rather dry in the winter (Hanssen-Bauer et al., 2019).

2.2 Field Data Collection

The use of UAVs allowed us to stay at a safe distance but within visual line of sight to take pictures of the crevassed glacier front (see Figure 2.2). Furthermore, drones are mostly independent of cloud coverage (also for pictures taken in visible wavelengths) in contrast to conventional remote sensing satellite data as long as clouds are above flight altitude (Hann et al., 2019). To determine the flight height of the drone above the surface several factors must be considered. In general, there is an interest to fly the drone as high as possible to save battery and operation time. However, the required image resolution limits the altitude of drone flights. Therefore, the ground sampling distance (GSD) is a common measure to calculate the corresponding size of one image pixel on the ground. The following equation can be used to determine the flight altitude that still guarantees the desired image resolution (Federman et al., 2017):

$$Distance\ to\ Object = \frac{GSD * Focal\ Length}{Pixel\ Size} \tag{2.1}$$

Both the focal length and the pixel size are given prerequisites of the camera. For the fieldwork of this thesis the two drones DJI Phantom 4 Pro and DJI Mavic 2 Enterprise were used. As seen in Table 2.2, the Mavic 2 Enterprise is lighter and therefore slightly more affected by winds. On the other side the Mavic 2 Enterprise tends to deal better with GPS issues on the field as it never lost the GPS connection. Furthermore, the Phantom 4 Pro has a focal length of 8.8 mm and a pixel size of 2.53 µm (DJI, 2017). The drone is equipped with a built in camera and a gimbal system (Federman et al., 2017). The Mavic 2 Enterprise on the other hand has a focal length of 4 mm to 6 mm whereas the pixel size is about 1.55 µm (DJI, 2019).

The stated Equation 2.1 calculates the maximal distance to an object which is allowed in order to guarantee a sufficient image resolution. However, when using UAVs the maximal distance to object does not correspond to the vertical distance (i.e. flight altitude) between the lens and the surface. This is because the surface objects which are not lying exactly underneath the

(a) (b)

Figure 2.2: DJI Phantom 4 Pro drone taking off to map Tunabreen during fieldwork in spring 2020 (photo taken by Christina Hess) and (b) DJI Mavic 2 Enterprise drone just before landing on the boat after mapping Nordenskiöldbreen in summer 2020 (photo taken by Andy Hodson).

lens but a bit further to the side would not be displayed with the sufficient resolution. The theory and all the relevant parameters are illustrated in Figure 2.3. Therefore, it is important to take the distance between the furthest point which still should be detected and the camera as the 'Distance to Object' (Federman et al., 2017), what can be done with simple trigonometry (Walczykowski et al., 2016).

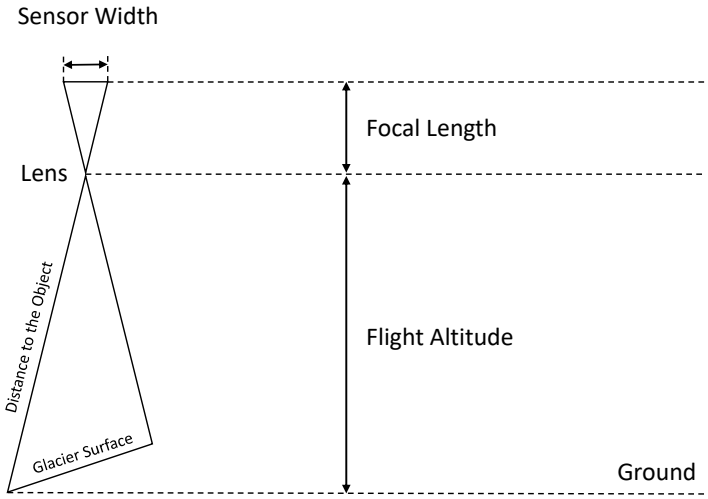

Figure 2.3: Sketch of surveying drone showing all the relevant factors used to calculate the flight altitude from the ground sampling distance (modified from Walczykowski et al. (2016)).

The goal was to get a DEM resolution of about 0.25 m/px. So the question appears, which image resolution is required to get the desired DEM resolution. This of course depends a lot on the parameter settings of the software (see Figure 2.5). On a similar study with UAVs flown above a glacier front, Chudley et al. (2019) obtained a DEM resolution that was roughly three times larger than the captured GSD. Therefore, we decided that the collected pictures should not exceed a GSD of 0.1 m/px. Given the camera prerequisites of the drone Phantom 4 Pro (Mavic 2

Enterprise, respectively) this leads to a calculated maximal allowed flight altitude of about 215 m (190 m) above the mapped glacier surface. Thus, during fieldwork the drones were operated at a vertical height of 200 m above ground level. However, the maximal flight altitude is assuming a flat area (see Figure 2.3 for illustration). As the glacier surface is increasing in altitude towards the upper part of the glacier, the effective drone height above the glacier surface decreases. Since the flight altitude was set at the lowest part of the glacier it always can be guaranteed that the required resolution is achieved regardless of the glacier's surface elevation change.

The following equation can be used to calculate the baseline distance between captured images (Federman et al., 2017):

$$Baseline\ Distance = (1 - \frac{Overlap\ in\ \%}{100}) * \frac{Distance\ to\ Object * Sensor\ Width}{Focal\ Length}. \tag{2.2}$$

A changing elevation of the mapped surface influences the required distance between two recorded images, the so called baseline distance, to guarantee a certain image coverage. In other words, two sequential pictures have to overlap to a certain degree for the photogrammetry approach to work and to ensure a sufficient DEM resolution. In the literature typical values of about 70 % for side overlap and a 80 % to 90 % forward overlap can be found (Gindraux et al., 2017; Jouvet et al., 2019; Rossini et al., 2018; Ryan et al., 2015, e.g.). For this thesis a forward overlap of 90 % and a side overlap of 80 % was desired. This leads to a baseline distance of maximum 105 m (80 m for Mavic 2 Enterprise) according to Equation 2.2. If this distance is not surpassed, a sufficient photo coverage is theoretically ensured. However, practically a baseline distance of 70 m was chosen to compensate for noise, unexpected errors and especially decreasing flight height further up the glacier. Given those settings, a sufficient spatial resolution as well as enough coverage could be guaranteed while still regarding the changing elevation of the glacier surface.

Two types of camera orientations can be used to capture aerial images: nadir and oblique. For the nadir photogrammetry the camera is positioned vertically above the surface whereas inclined camera angles are used for the oblique photogrammetry (Federman et al., 2017). Nadir photogrammetry is the more traditional way of image acquisition while recently the oblique photogrammetry is getting increasingly important (Casella and Franzini, 2016). A study of Vacca et al. (2017) stated that the use of oblique UAV flights over buildings is able to increase the model accuracy compared to nadir flights. This shortcoming explains the upcoming interest in oblique imagery. Furthermore, nadir image acquisition produces highly detailed DEMs of the observed objects but struggles to model vertical elements and surfaces (Aicardi et al., 2016). Since this study mapped crevassed glaciers, vertical surfaces are indeed an issue. However, the deep crevasses are positioned close to each other and thus it is difficult to observe the whole vertical surface of a crevasse with only oblique image surveying due to shadow effects of crevasses lying in between.

On a minimal working example (247 images whereof 97 were oblique) of data collected on Heuglinbreen in spring 2019 the effect of the camera orientation was tested. Figure 2.4 illustrates the resulting DEMs of the extract of Heuglinbreen calculated with oblique, nadir and oblique-nadir image input data sets. The oblique-only method achieved to build an accurate surface for the upper part of the objects and the flat surface but failed to give accurate informations about the deeper part of the crevasses. Both the nadir-only and the nadir-oblique combination managed to build good and complete surface data but the latter produced a slightly more accurate model with less noise. Furthermore, James and Robson (2014) found out, that including oblique images to the processing workflow can significantly reduce the systematic error of DEMs. However, for

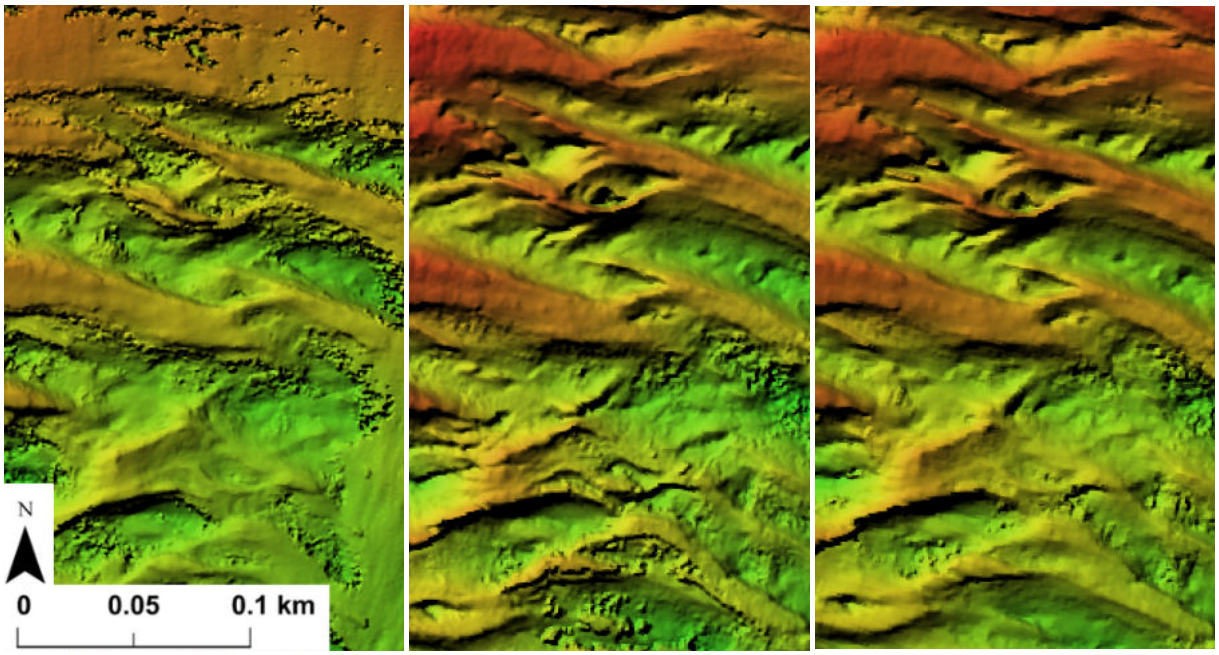

(a) Oblique (b) Nadir (c) Oblique-Nadir

Figure 2.4: Minimum working example on an extract of Heuglinbreen to show the impact of the camera orientation on the resulting DEM built with Agisoft Metashape. The camera orientation oblique (a) alone could not guarantee a good surface model construction. The nadir-only camera orientation (b) already presented good results. The combination of both nadir and oblique camera orientations (c) led to a slightly better model construction and less noise. The colors illustrate the relief elevation of the glacier extract from 75 m a.s.l. (green) to 110 m a.s.l. (red).

the purpose of this study the relative distance between the crevasses is more important than their accurate localisation. Therefore, in this study and to simplify the fieldwork it was decided not to take the extra effort to measure everything in nadir and oblique imagery but rather have a larger area mapped at all. Thus, the images were only captured in nadir mode.

There exist three different ways to collect data with an UAV. These are manual, assisted and autonomous mode which can be chosen for both flying and image acquisition (Nex and Remondino, 2014). The autonomous mode is a convenient way to ensure consistent overlap and prevent holes in the dataset. For the same reason also linear flight patterns can be used. Furthermore, software tools present help with the image acquisition as the flight plan can already be prepared before fieldwork such that the drone automatically follows the path and takes pictures at every waypoint (Uysal et al., 2015). Therefore, in our fieldwork we made use of this technologies and the flights were autonomously conducted with preprogrammed waypoints.

2.3 Building Digital Elevation Models

2.3.1 Structure-from-Motion and Multi-View Stereo

In recent years, structure-from-motion (SfM) together with multi-view stereo (MVS) has demonstrated its large potential to make 3D topographic survey broadly available. It requires minimal expertise and cost while producing rapid 3D point clouds with a comparable data quality to

other existing survey methods (e.g. terrestrial laser scanning). In fact, SfM refers to the first part of the workflow in which it uses bundle adjustment algorithms to rebuild the geometry of the captured surface. In a second stage, the MVS photogrammetry algorithms are used to strongly increase the density of the sparse point cloud (Smith et al., 2016a).

In this thesis the software Agisoft Metashape version 1.6.2 (Agisoft LLC, 2020) was used. It extracts data from the aerial images using a photogrammetry method that then provides surface information about the shape of crevasses like depth, size and distribution. The software runs on a fully automatically workflow and builds 3D models that can be used to construct georeferenced DEMs. Figure 2.7 gives an overview of the used workflow for the DEM generation by Agisoft Metashape. The first stage of the processing workflow was to collect and import pictures and check for sufficient image quality and overlap. To align the photos in a next step, the SfM processing reconstructs the three-dimensional geometry and camera position of a surface from two-dimensional pictures that are taken from multiple viewpoints (Ryan et al., 2015). Therefore, the software automatically detects and matches characteristic features that can be seen on various pictures regardless of the view perspective or lighting conditions (Rossini et al., 2018). Thus, it is important that the position and orientation of the camera at the time of image acquisition is recorded to relate each point to a reference datum and to get 3D coordinates of any visible point that appears in at least two pictures (Irvine-Fynn et al., 2014). As a result, the software builds a sparse point cloud model. In a next stage, a dense point cloud is generated with the Agisoft Metashape MVS approach, which is based on the pictures and their estimated camera position. Dense point clouds have been cleared from noise before proceeding with the generation of a DEM (Agisoft LLC, 2019).

2.3.2 Parameter Settings of Agisoft Metashape

Building DEMs with the software Agisoft Metashape is a straight-forward three-step process starting from image alignment, further to the construction of a dense cloud and finally a DEM (Verhoeven, 2011). The whole processing is automated and only requires little expertise to run the software and build a random, non-specific DEM (James and Robson, 2012). However, it comes along with many parameter settings that can be selected to further improve the DEM quality depending on the input data and the output purpose (see Appendix A for chosen parameter settings of each DEM). To determine an ideal set of parameters for our approach, many different combinations of settings were tested on a minimal working example. The finally used parameters are summarized in the workflow sketch that can be found on Figure 2.7. The stated setting of parameters is found to behave best for the given setup and research purpose of this thesis, but not necessarily for any other investigation.

Before starting the processing, the quality of images should be checked, as vague input photos (e.g. poorly focused) can influence the alignment results badly. Thus, the software provides an image quality check by calculating the sharpness level of the most focused part of a image (Agisoft LLC, 2019). All photos with a quality value of less than 0.5 have been disabled and were excluded from the further processing. In this thesis only a small number of images needed to be disabled which were pictures taken in the spring campaign from non-crevassed areas with snow and little contrast.

The first processing step 'Align Photos' builds a sparse cloud model by finding the camera position and orientation of each picture. The photo alignment procedure can be controlled by several parameter settings. The accuracy of the alignment can either be 'High', 'Medium' or 'Low. The higher the accuracy settings the more accurately estimated is the camera position. A

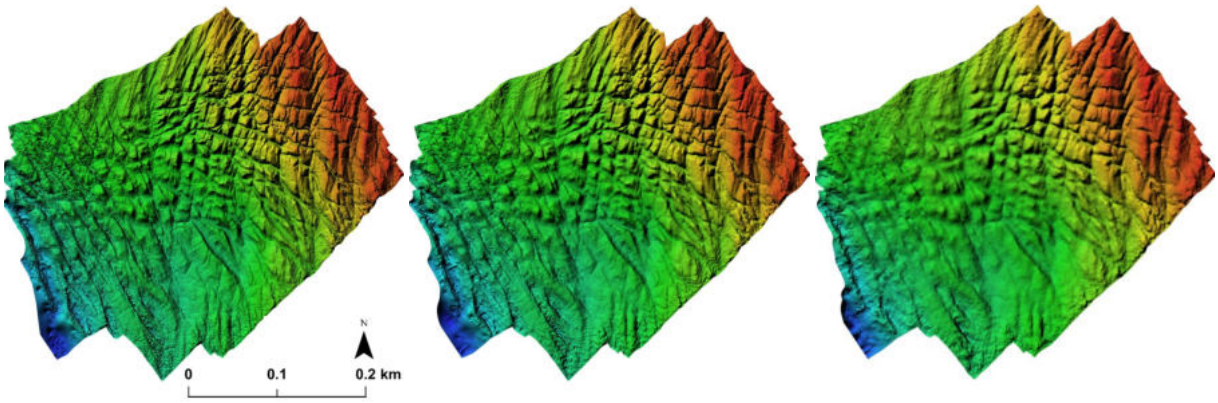

(a) High (b) Medium (c) Low

Figure 2.5: Minimum working example on an extract of Nordenskiöldbreen 2019 illustrating the impact of the parameter 'Quality' for the processing step 'Build Dense Cloud' in Agisoft Metashape. The parameters High (a), Medium (b) and Low (c) can be selected. The chosen parameter has an impact on the output pixel resolution ranging from 0.11 m (High) to 0.23 m (Medium) and 0.45 m (Low). The colors illustrate the relief elevation of the glacier extract from 15 m a.s.l. (blue) to 110 m a.s.l. (red).

minimal working example on an extract of Nordenskiöldbreen 2019 data (21 images) has been performed to test the influence of this specific parameter by setting all the other parameters on default. The results showed only small differences between the final outcome of each alignment accuracy. Furthermore, higher accuracy comes along with longer processing time. Therefore, the accuracy 'Medium' has been chosen as a compromise. The significant stage in the alignment process is the detection of features across different photos. To speed up this time-consuming step different modes of 'image pair selection' can be chosen. The preselection mode 'Generic' uses lower accuracy setting first to select overlapping pairs of photos. The mode 'Reference' on the other hand uses the measured camera location to select the overlapping pairs of photos. For this study both preselection modes were chosen, what is known to speed up the alignment process even more (Agisoft LLC, 2019).

The parameter settings of the second processing step 'Build Dense Cloud' contributed by far the largest impact on the resulting DEM of the whole workflow (see Figure 2.7). In particular, the quality of the dense cloud, which can either be 'High', 'Medium' or 'Low', has a large influence on both processing time and resolution of the DEM. This effect has again been tested on a minimum working example (21 pictures) on an extract of Nordenskiöldbreen measured in 2019. The resulting DEMs are illustrated in Figure 2.5. In this example the resulting output resolution varies from a pixel size of 0.11 m (high) to 0.23 m (medium) and 0.45 m (low). It can be seen that the surface features that were processed with a high quality provide the constructed surface in a higher level of details but also with more noise, in particular deep inside the crevasses. Gindraux et al. (2017) investigated the effect of the quality parameter on processing time and found out that the quality 'Low' is 18 times faster than 'High' and six times faster than 'Medium'. In the end, the parameter 'Medium' was chosen because the level of details is still high enough to fulfill the purpose of this thesis while the processing time is strongly reduced compared to the parameter 'High'. A further parameter that can be set for the construction of the dense cloud is the depth filtering mode which is used when Agisoft Metashape calculates the depth maps for every picture. In the User Manual of Agisoft Metashape (Agisoft LLC, 2019) it is recommended to choose an aggressive depth filtering mode that is often used for aerial data

processing, especially if the reconstructed area is not containing any meaningful small details. Since this mode helps to sort out most of the outliers, for this thesis an aggressive depth filtering mode was applied.

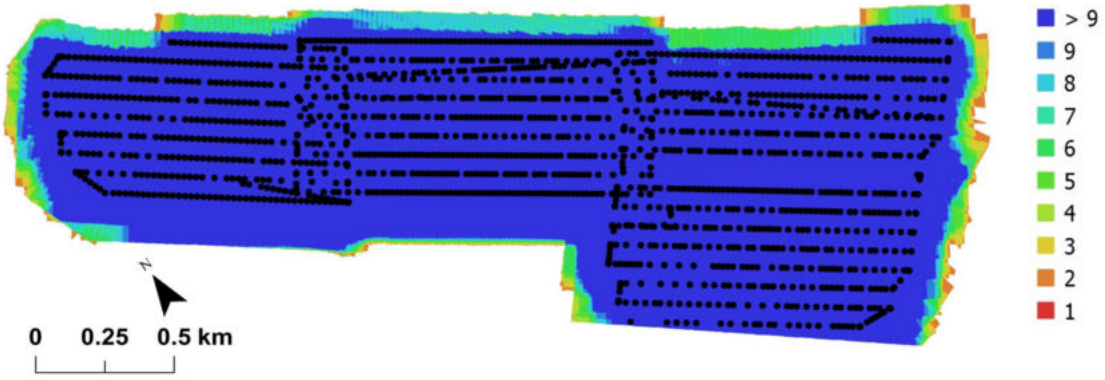

Figure 2.6: Drone flightpath with captured images (black dots) and image overlap (colors) of pictures of Tunabreen taken on three days in summer 2019.

To build the DEM as the third step of the processing, a source data can be selected. Among others this can either be the sparse point cloud or the dense point cloud data. Since the DEM is the main data source of this study the dense point cloud was selected as data source because it provides the best accuracy. As already mentioned before, a certain amount of overlap between two sequent pictures is required to guarantee an uninterrupted DEM at the end. However, in excessive image datasets several pictures are redundant and can be removed in order to save processing time. Figure 2.6 shows the flightpath of the drone that was taking pictures from Tunabreen on three different days in summer 2019. The coloured area shows the overlap which is very high (blue) for most parts with more than 9 overlapping images apart from the regions close to the border. This indicates that there were many redundant pictures which could be disabled for the calculation process. Agisoft Metashape provides a tool called 'Reduce Overlap' that uses a rough mesh built from the sparse point cloud to scan the dataset for redundant images (Agisoft LLC, 2019). The image overlap can again be selected as 'High', 'Medium' or 'Low'. For this thesis 'High' was chosen to prevent quality losses while still strongly reducing the processing time. For all constructed DEMs between 10 % to 50 % of images were disabled and therefore not used for the proceeding calculations.

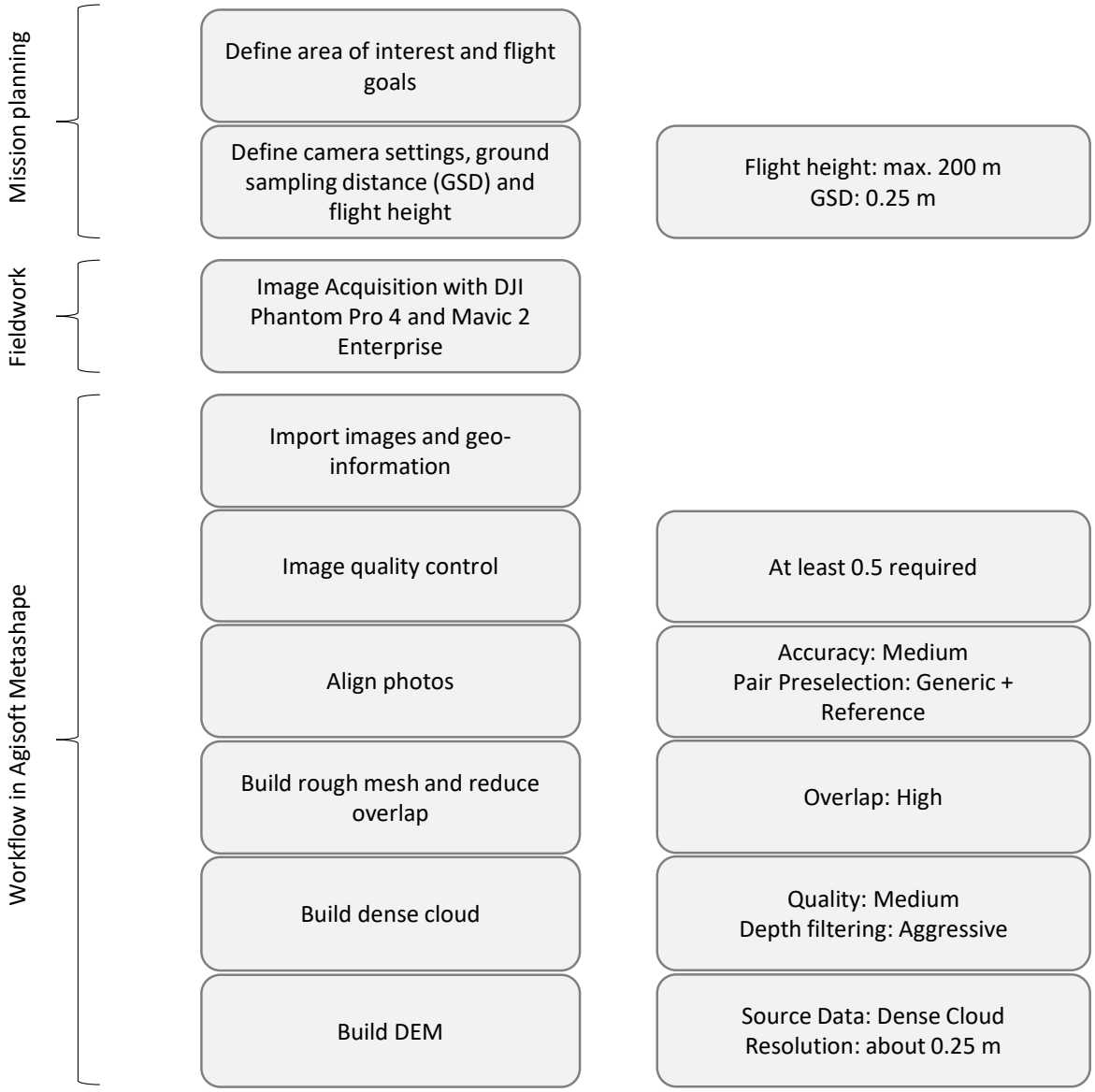

Figure 2.7: Used workflow for the generation of DEMs (left) and the selected parameters (right) with Agisoft Metashape (modified from Gindraux et al. (2017), Rossini et al. (2018) and Federman et al. (2017)).

2.3.3 Georeferencing, Drone Type and Weather

It was impossible to place any ground control points (GCPs) on the glacier surface to georeference the mapped glaciers. The highly crevassed areas were inaccessible in all field campaigns or accessible locations too far away from the mapped area to still be recorded on the pictures. Even the sea ice in front of the glaciers could not have been approached close enough due to safety reasons. However, final product accuracy can be significantly reduced if no network of GCPs can be set up. The practical limitations of providing GCP georeference are one of the most limiting factors of photogrammetry products based on UAVs (Chudley et al., 2019). Especially in glacial environments, these problems are often faced and thus alternative georeferencing methods are applied. Such approaches can be: using tie points to geodetically tie the data together (Kraaijenbrink et al., 2016), placing an external on-board navigation GPS geolocation on the UAV (Ryan et al., 2015) or applying GNSS-supported aerial triangulation that often is combined with real-time kinematic (RTK) or post-processed kinematic (PPK) correction (Chudley et al., 2019; Groos et al., 2019). None of the stated methods could be used in this thesis due to unavailable equipment or missing fixed locations on the moving glacier surface. Accordingly, the georeferencing could only be provided through the camera orientation data of the UAV (James et al., 2017). In other words, the GPS coordinates that are logged for each captured picture by the UAV are used for georeferencing. However, such an approach cannot keep up with methods using GCPs because the internal GPS system of the drone has a relatively low accuracy (Federman et al., 2017).

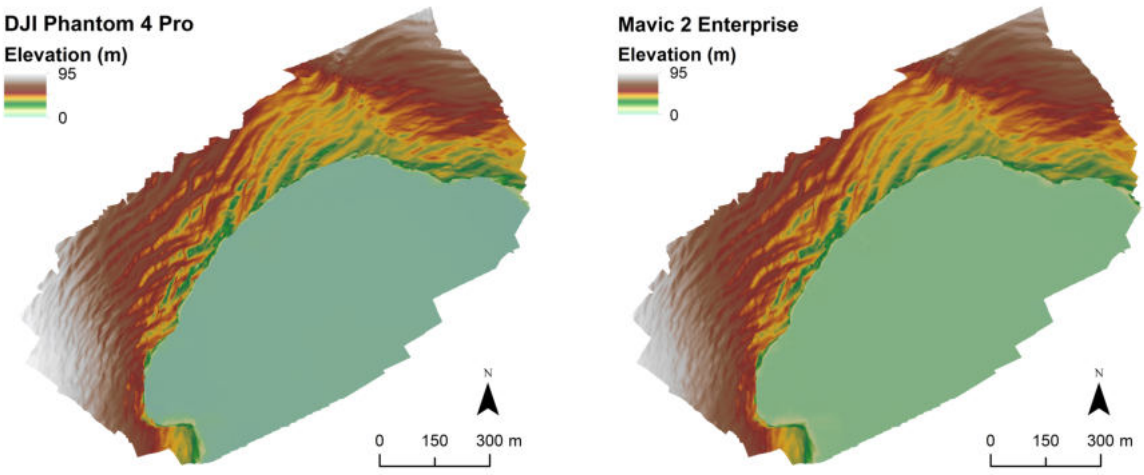

Figure 2.8: Illustration of the impact of chosen drone types for image acquisition. The pictures of the DEM to the left were taken with the Phantom 4 Pro, whereas the images for the other DEM (right) were captured with a Mavic 2 Enterprise. Both data sources managed to build a very similar DEM with only minor differences.

To check the sensitivity of the drone type that captures the images on the resulting DEM, a small area of Fridtjovbreen has been flown twice with two different drones. The drone DJI Phantom 4 Pro and the DJI Mavic 2 Enterprise were both flown at approximately the same altitude of about 200 m a.s.l. varying the most of 20 m vertically. In Figure 2.8 the resulting DEMs were illustrated, whereas their DEM resolution vary slightly with a pixel size of 0.26 m (Phantom 4

Pro) and 0.34 m (Mavic 2 Enterprise). Nevertheless, the two DEMs show that there is only a minor difference between the two input datasets. Both the Phantom 4 Pro (left) and the Mavic 2 Enterprise (right) manage to represent the crevassed glacier area. Only a minor horizontal and vertical deviation can be detected between the two DEMs what can be attributed to the fact that no GCPs were used. However, the relative distances between the two DEMs correspond well.

The days of fieldwork were chosen in a way to avoid sun, wind and precipitation. Wind and precipitation on one side make it difficult or impossible to operate the drone. Sun on the other side leads to shadows effects between two crevasse obstacles. Both fluctuating lighting conditions and shadow during image acquisition can interfere with the keypoint matching stage of the SfM processing (Mallalieu et al., 2017). Accordingly, whenever possible overcast days were chosen which presented ideal diffuse illumination condition (James and Robson, 2012). The real impact of the lighting conditions is difficult to estimate in the field as we only captured pictures once for each glacier and year. However, Agisoft Metashape managed to build reasonable DEMs on days that turned out to be sunny despite an overcast forecast (e.g. Fridtjovbreen). According to Agisoft LLC (2019), changing lighting conditions are in particular important for texture and orthophotos and less for DEMs as used in this thesis.

The surface characteristics of the glacier also has a large influence on the keypoint matching and thus the construction of DEMs. Gindraux et al. (2017) state that for fresh snow too little matching keypoints can be found and therefore image orientation is no longer possible. Yet, already after one day of sunlight the snow cover developed enough contrast for image orientation to work. Since for our field campaigns the snow never has been that fresh and especially since the crevasses provided a lot of contrast themselves, this issue turned out to be negligible.

2.4 Data Preparation for Model Calculation

Before starting the model calculations of the aerodynamic roughness length, the DEMs need to be prepared. Figure 2.9 shows the DEM of Fridtjovbreen how it was originally mapped and constructed (left) and then after the preparation step (right). The DEMs obtained from the SfM processing were rotated in such a way that the main crevasses were aligned crosswise from left to right with the glacier front at the bottom (lower part pf y-axis). Additionally, some DEMs were cropped to remove mapped areas with useless (i.e. no glacier) surface characteristics or to keep the focus on the heavily crevassed areas (i.e. Fridtjovbreen). Moreover, the sea ice/water area was removed as it has no contribution to the turbulent heat exchange of the glacier. In a next stage, the DEM was divided into various new subareas of equal width and length. The size of the subareas was chosen to be 50 m x 50 m, as it is the grid that best represents the average size of a roughness element (for the definition of a roughness element see below). After that, the DEMs were ready for the z_0 calculation. Therefore, every subarea is implemented into one of the five models to calculate z_0 producing one single z_0 value for each subarea and model.

To consider the impact of the wind direction on the resulting z_0 values, each subarea was calculated four times corresponding to the four cardinal wind directions. Since the DEM was rotated, it allows us to calculate z_0 values of the dominant wind directions on glaciers (i.e. common katabatic down-glacier winds (Karner et al., 2013)). In a first step, the elevation data of the subareas was detrended in the models using a 2D-linear detrending method. The appropriate detrending method depends on the scale of the study. According to Chambers et al. (2020), a linear detrending method is fine for smaller plots but not for larger areas. On a first sight a

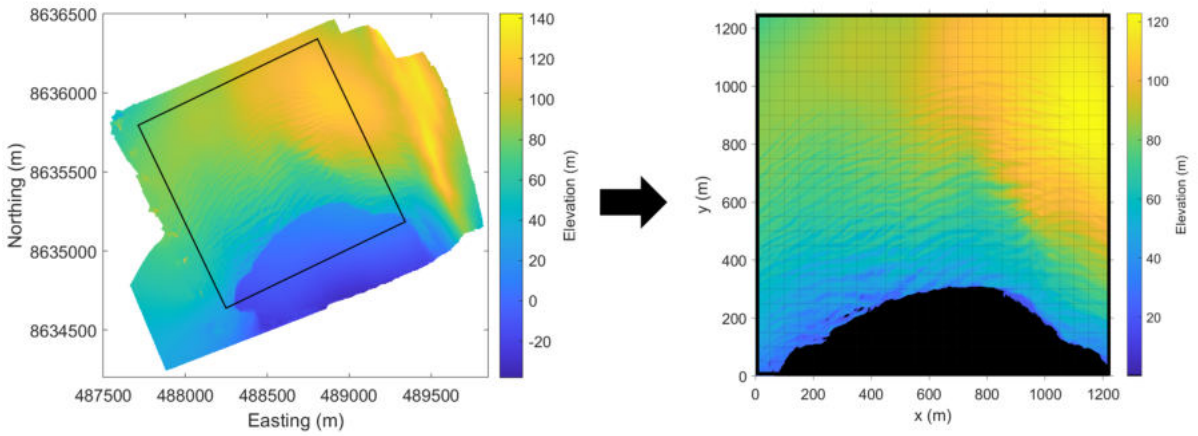

Figure 2.9: The originally mapped DEM (left) of Fridtjovbreen was rotated and cropped (black frame) before using it for the model calculations (right). Additionally, the elevation values of the sea ice area were removed and the whole DEM was divided into subareas of 50 m x 50 m.

grid size of 50 m for the subarea might seems like a large area and thus not ideal for a linear detrending method. However, as our roughness elements (i.e. crevasses) are relatively large, a linear detrending method at this grid size seems appropriate to determine the roughness of the crevassed surface. In contrast, if a too small subarea grid size would be chosen, this could lead into a flattening effect of the actual roughness elements.

This issue is illustrated in Figure 2.10 (left), where the blue line shows a random transect of two roughness elements on Fridtjovbreen each with a length of about 30 m. Two linear detrending methods were applied for this illustration, one for the whole transect (green line) and one for 10 m intervals (red line). If a grid size lower than the obstacle wavelength (e.g. 10 m) is chosen, then the linearly detrended transect is not capturing the whole surface roughness of the crevasse properly (see red line in Figure 2.10, right). In contrast, the linearly detrended transect length of 60 m represents the two roughness elements well (green line, right). Smith (2014) described the same effect mentioning that removing any trend from data affects the representation of small-scale roughness elements because they are not representing the true topographic expression. Furthermore, a main assumption of the approach followed in this thesis is that the wind is blowing parallel to the large-scale glacier surface. Therefore, it is important to also consider the large-scale roughness elements which are more important for this thesis than the small-scale roughness on the crevasse obstacle themselves. In other words, a subarea grid size of at least the length of an average obstacle wavelength should be chosen to account for the large-scale surface roughness of the crevassed glaciers.

This leads to the definition of an average obstacle length. The range of roughness element sizes on the investigated tidewater glaciers is large. Distances from one crevasse to the other reach from somewhat around 10m up to 60m and locally even more (see Chapter 3.1). A small investigation revealed that roughness obstacles of the mapped tidewater glaciers have an average wavelength between 30 m and 50 m depending on the wind direction and glacier (see Table 3.2). Furthermore, since a grid size larger than one roughness element still takes into account the issue stated above, there is no clear upper boundary. Therefore, we were confronted with the question which subarea grid size might be the most appropriate. One main goal of this thesis is to provide various z_0 values across the glacier. Thus, we are in general interested in keeping the grid size as small as possible to provide a large spatial resolution. As a compromise, a subarea grid size

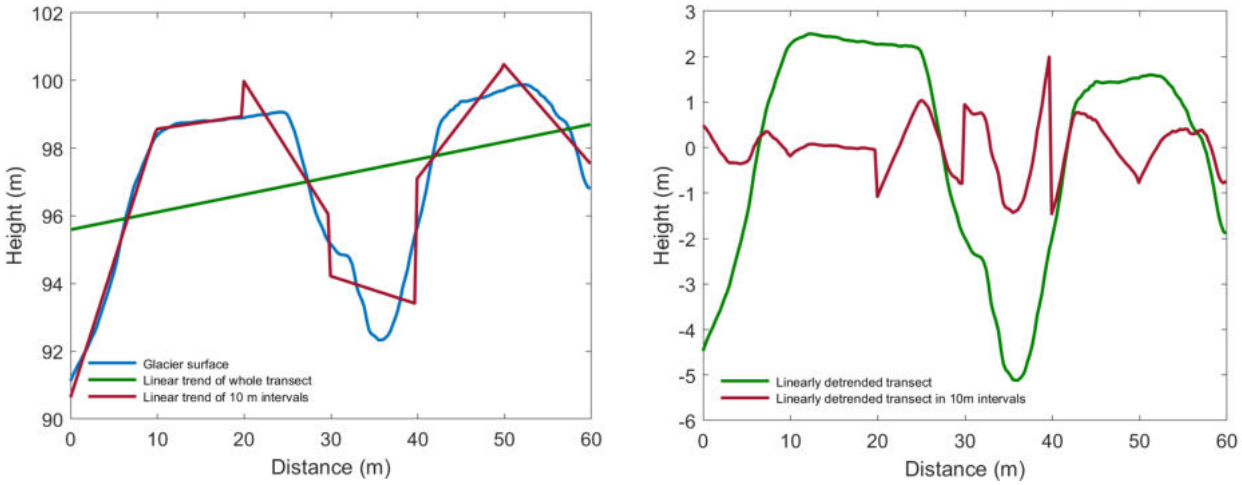

Figure 2.10: The left graph shows a random transect of two roughness elements on Fridtjovbreen (blue line). The transect is linearly detrended, once over the whole profile (green) and another time in 10 m intervals (red). The right graphs illustrates the according linearly detrended transect. While the approach of linearly detrending the whole transect (green line on right graph) is able to detect the two roughness elements, the 10 m intervals led to randomly detrended elevation values (red). To prevent that, a subarea grid size should not be smaller than the actual wavelength of one roughness elements.

of 50 m x 50 m was chosen for the main calculation. This grid size corresponds to the upper range of an estimated average roughness element. Thus, it could be guaranteed that most of the roughness elements have a length scale lying within the scale of the subarea grid size while still keeping the grid size as low as possible. However, to investigate the impact of this decision and therefore the dependency of z_0 values on increasing subarea grid size, several grid sizes between 5 m and 150 m were tested in a small case study on Fridtjovbreen.

Figure 2.10 further stimulates the discussion about the definition of a roughness element, whereof two can be found on the given transect. From a glaciological perspective, the crevasses protruding downwards from the glacier surface and their effect on turbulent fluxes are the main objective. From an aerodynamic point of view however, it makes more sense to divide the surface into various obstacles protruding upwards. Thus, an obstacle is defined as the part of the glacier located between two crevasses - called roughness element. This goes back to the experiment of Lettau (1969) using bushel baskets (all of equal size and placed in a systematic pattern) as obstacles on a flat plane. Accordingly, the roughness elements in this thesis spanning from one crevasse to the next are assumed to have the same effect as the baskets in the original experiment.

2.5 Model Calculation of Aerodynamic Roughness Length

Once the elevation data is detrended, it can be used to calculate the aerodynamic surface roughness length. The most widely used methods in glaciology to calculate z_0 values with the bulk method are all based on the study of Lettau (1969). The author developed the following equation for the bulk aerodynamic roughness length:

$$z_0 = c_d h^* s/S, \tag{2.3}$$

where h^* is the effective obstacle height (m), s is the silhouette or frontal area of the obstacle (m^2) and S the according horizontal ground area (m^2). The value $c_d = 0.5$, first proposed by Lettau (1969), corresponds to the average drag coefficient of a characteristic roughness element. It is defined as the ratio of wind kinetic energy to surface stress. Accordingly, the drag coefficient accounts for the change in effective drag by individual roughness elements with increased relative sheltering and can be used for moderately inhomogeneous surfaces (Wiernga, 1993). The value of 0.5 has has been widely adopted in the field of glaciology for various types of roughness elements (e.g. Brock et al., 2006; Munro, 1989; Nicholson et al., 2016).

Equation 2.3 is also based on the bushel baskets experiment of Lettau (1969). Under these laboratory conditions, the parameters of Equation 2.3 can be obtained fairly easily. However, this turns out to be more difficult in glacial environment where the individual roughness elements vary a lot in height, size and density (Chambers et al., 2020). Therefore, the original equation has been adjusted and further developed in several studies leading to different methods to estimate z_0 values. In this thesis five different approaches (hereafter called models) were used to estimate z_0 values, all of which have already been applied in similar studies before (for overview of the five models see Table 2.3). This procedure allows us to determine the strengths and weaknesses of each model and to find a range of meaningful aerodynamic roughness length values independent of the used model. The five models can further be subdivided into two groups that are based on different assumptions and simplifications. They mainly differ in terms of determining and measuring the roughness elements. One group is counting the number of roughness elements in a transect (hereafter called transect method) while the other group is based on a raster approach (hereafter called raster method) using every DEM cell value for the calculation of z_0.

2.5.1 Transect Method

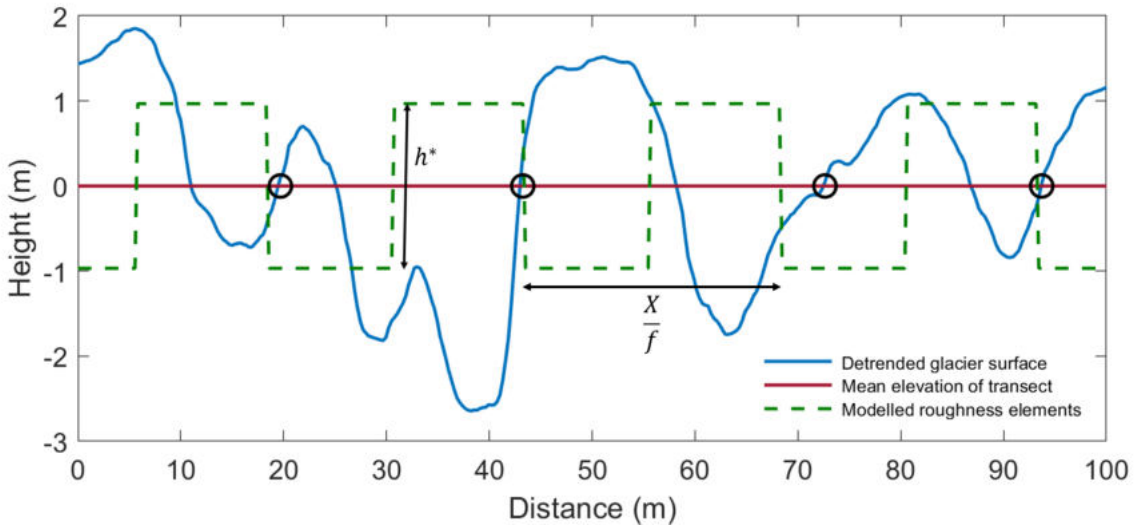

Figure 2.11: Schematic illustration of the transect method modelling the roughness elements (green) of the detrended glacier surface (blue) within one transect (X). The black circles mark the zero-up-crossings (f) from below to above the mean elevation of the transect (modified from Smith et al. (2016b)).

For the transect method the roughness elements are modelled by looking at only one profile of length X (m) at the time. Each row of the subarea is treated as a separate transect. Then, the number of roughness elements in each transect is counted and used for the calculation as illustrated in Figure 2.11. More precisely, it is counted how many times in each transect the detrended profile crosses the mean transect elevation from values below to values above the mean elevation, the so called zero-up-crossing frequency (f). As Munro (1989) showed in his study, the frontal silhouette area s and the ground area S of Equation 2.3 can then be calculated with f and X only.

The transect method presents a simple approximation of the roughness elements across a profile and is based on the following assumptions (Smith et al., 2016b):

1. All roughness elements are of equal height.
2. All roughness elements are uniformly distributed.
3. Roughness elements do not shelter each other.
4. All roughness elements are isotropic (i.e. same frontal area for each wind direction).

As illustrated in Figure 2.11 these assumptions can not completely be fulfilled on heavily crevassed glacier areas. However, Munro (1989) states that the method still provides a good approximation as the results only differ about 12 % from reference z_0 values. Furthermore, the method has the advantage of being computational simple.

An important rule stated in the method of Munro (1989) is that the silhouette area s is calculated in a vertical plane perpendicular to the wind direction. However, Smith et al. (2016b) figured out that this approach is not able to detect a crevasse that is aligned exactly perpendicular to the prevailing wind direction. Figure 2.12 illustrates this wind direction issue. In such a case, the given results would differ significantly from the z_0 values calculated with the raster method. If the roughness elements would fulfill all the stated assumptions above, no such difference could be detected and z_0 values would be the same for profiles taken perpendicular and parallel. Further, Smith et al. (2016b) state that this issue is only important for studies that focus on natural streamlined surfaces. However, since heterogeneous and perpendicularly aligned crevasses are the main focus of this thesis it would make no sense to choose a transect aligned perpendicular to the wind direction. This is because only a transect aligned parallel to the prevailing wind direction is able to account for the topographic variability and surface roughness for this specific wind direction (see Figure 2.12). In addition, wind systems are influenced by the large-scale catchment topography such that winds often flow up or down the glacier (Quincey et al., 2017), leading to exactly such a setup as described above. To account for these issues, in this thesis the profiles were always chosen parallel to the prevailing wind direction and then calculated for all cardinal wind directions individually.

Munro

The approach of Munro (1989), hereafter called Munro, has been widely used in glaciological studies (e.g. Brock et al., 2006; Irvine-Fynn et al., 2014; Quincey et al., 2017). The author simplified and adapted Equation 2.3 of Lettau (1969) and thus adopted it into the field of glaciology. In his method the height of roughness element h^* (m) was calculated by taking twice the standard deviation of elevations of the detrended transect. To do so, the mean elevation was

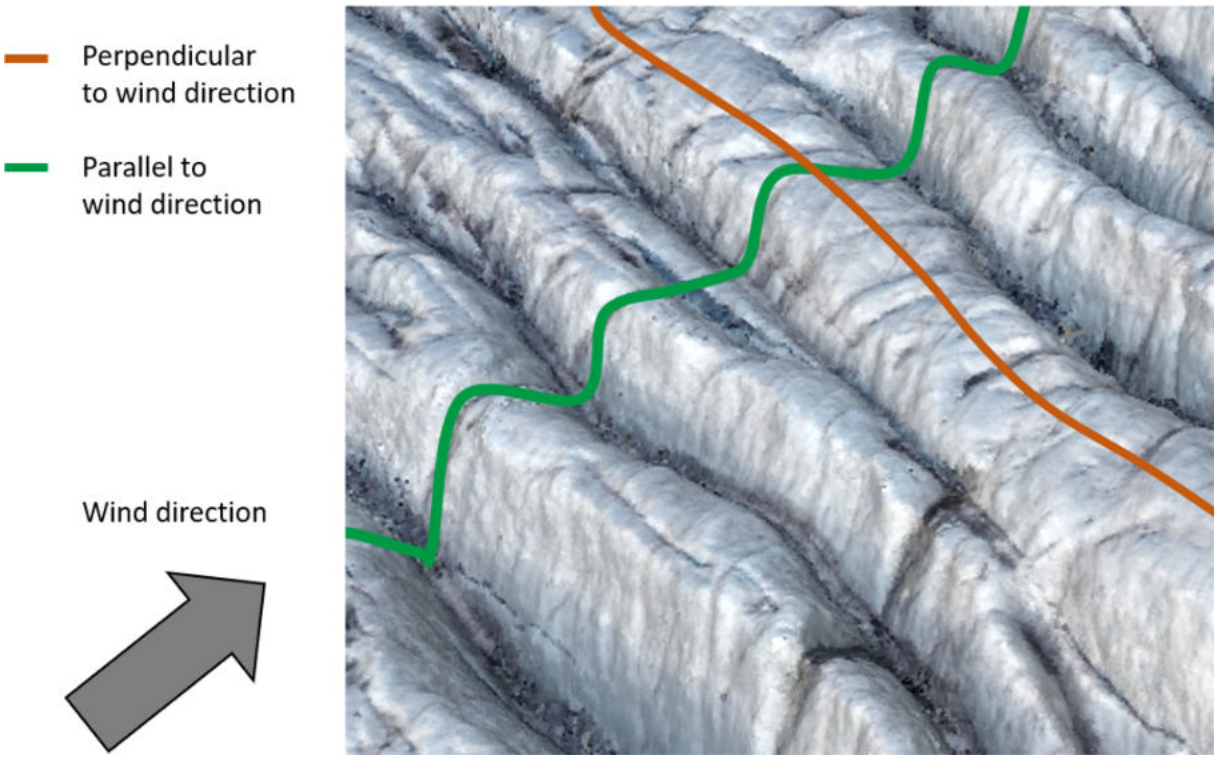

Figure 2.12: Demonstration of different profile elevation values between transects aligned perpendicular (orange) or parallel (green) to the prevailing wind direction (grey arrow) for the setup of perpendicularly aligned crevasses. Only a transect aligned parallel to the wind direction can account for the topographic variability and thus the surface roughness of the glacier area for this specific wind direction.

set to zero. This leads to the following equations for the frontal silhouette area s (m^2) and the ground area S (m^2):

$$s = \frac{\sigma X}{f}, \tag{2.4}$$

$$S = \left(\frac{X}{f}\right)^2. \tag{2.5}$$

For any given transect, the aerodynamic roughness length was then calculated to be:

$$z_0 = \frac{f\sigma^2}{X}. \tag{2.6}$$

Every row of the subarea was regarded as a transect leading to as many z_0 values as there are rows in each subarea. The final z_0 value for each subarea was then calculated as the mean of the individual row z_0 values.

Table 2.3: Overview of parameters from the Lettau (1969) Equation 2.3 used for the z_0 calculation in each model.

Parameter	Smith	Chambers	Fitzpatrick	Munro	Lettau
Effective obstacle height h^* (m)	Mean height above the detrended plane	2 x standard deviation of z above detrended plane	Mean height above the detrended plane	2 x standard deviation of detrended profile	Mean obstacle height
Silhouette area s (m^2)	Frontal area above detrended plane across whole subarea calculated for each cardinal wind direction		Frontal area across subgrid above the height of the first row cells calculated for each cardinal wind direction	Frontal area of a modelled roughness element: $h^*X/2f$. With X = transect length, f = up-crossing frequency	
Ground area S (m^2)	Full area of DEM subarea		Area of subgrid	Ground area of a modelled roughness element: $(X/f)^2$	
Drag coefficient c_d	0.5				
Roughness length z_0 (m)	$z_0 = c_d h^* s/S$				

Lettau

In the next model, hereafter called Lettau, we again followed the transect method by counting the zero-up-crossings as stated by Munro (1989). However, for this method h^* was not represented by twice the standard deviation of elevations of the detrended transect (as in the Munro model). Instead, it was defined as the average vertical extent of the roughness elements, as originally proposed by Lettau (1969). Therefore, Equation 2.4 has been slightly adjusted to:

$$s = \frac{h^* X}{2f}, \tag{2.7}$$

leading to the following equation for the aerodynamic roughness length:

$$z_0 = \frac{f(h^*)^2}{4X}. \tag{2.8}$$

Again, the final z_0 value of each subarea corresponds to the mean of its row z_0 values. However, the definition of h^*, as the mean of all normalized and detrended cell elevation values across each transect, was discussed controversially among different glaciological studies. Several authors (e.g. Chambers et al., 2020; Irvine-Fynn et al., 2014) still stick to the definition $h^* = 2\sigma$ initiated by Munro (1989). Unlike them, Smith et al. (2016b) used a h^* that is calculated as the mean height of all points above the detrended plane. This definition was later adopted by several studies (e.g. Nicholson et al., 2016; Quincey et al., 2017).

2.5.2 Raster Method

The transect method is a computationally efficient simplification of the real surface roughness. However, as only the number of zero-up-crossings is effectively needed for the calculation, large volumes of the input topographic data remain unused. Such an approach is therefore most appropriate for situations with limited data availability or calculation capacity (Smith et al.,

2016b). The application of drone surveying combined with SfM processing is definitely not accounted to these situations. Additionally, the Lettau model only holds at low densities of roughness elements because otherwise the roughness elements begin to aerodynamically interfere with each other (Rounce et al., 2015). This has an impact on the resulting z_0 values and therefore needs to be considered in the model calculations. Due to all these reasons a new method that compensates for the mentioned shortcomings has been applied (see Figure 2.3 for overview).

The raster method is directly based on the Lettau (1969) Equation 2.3 and determines the roughness elements by looking at cell elevation values of a DEM raster. Therefore, every cell value of the row is considered for the calculation and the elevation differences between two adjacent cells define the surface roughness at the end. A main advantage of the raster method is that assumptions 1.-4. from Subsection 2.5.1 can be nullified. Figure 2.13a illustrates how the frontal area s is calculated directly from the cell's elevation values and for each cardinal wind direction. Accordingly, assumptions 1., 2. and 4 can be repealed. To consider the sheltering effect between close roughness elements only frontal areas above the detrended zero plane are included in the calculation (Smith et al., 2016b). Thus, also assumption 3. from subsection 2.5.1 can be neglected.

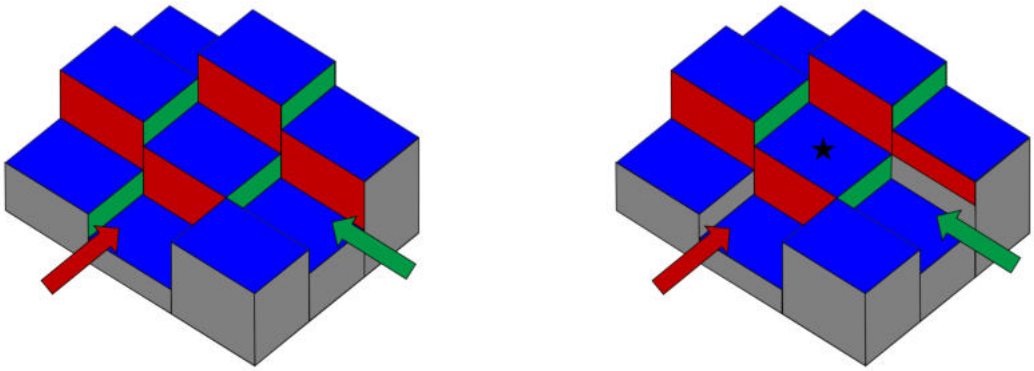

(a) Smith and Chambers model

(b) Fitzpatrick model

Figure 2.13: Schematic illustration of raster method highlighting the exposed frontal area s for two different wind directions with colors (red and green). Figure (a) shows the approach for the Smith and the Chambers model whereas Figure (b) illustrates the Fitzpatrick model (modified from Smith et al. (2016b) and Fitzpatrick et al. (2019)).

Smith

The following model, hereafter called Smith model, is based on the 'DEM-based' approach described by Smith et al. (2016b) in their study about z_0 values of glacial surfaces with data obtained from terrestrial laser scanning. The parameters s and h^* from Equation 2.3 were calculated individually for each row of the subarea. The frontal area s is the sum of the frontal areas of each cell that can be seen if the previous cell in the same row has a lower elevation value (see Figure 2.13a). However, to compensate for the sheltering effect mentioned before only frontal areas lying above the detrended zero plane were used for calculation. In other words, elevation values below the trend line (i.e. negative values after detrending) are assumed to have no effect on the surface roughness due to sheltering of the obstacle in front. The same is valid for the effective obstacle height h^* that was calculated as the mean elevation of all the cells of each row

above the zero plane. The resulting row s values were then summed up, while the mean of the row h^* values was calculated to bring it down to one single value for each subarea according to Equation 2.3. Lettau (1969) specified the ground area S to contain not only the ground area of the roughness element itself but also the surrounding plot area (i.e. area below the zero plane). Thus, the value S corresponds to the area of the DEM subarea. At the end, one z_0 value for each subarea and each cardinal wind direction was calculated with the Smith model.

Chambers

This model (hereafter called Chambers model) is very similar to the Smith model only differing in the definition of the effective obstacle height h^*. The model is based on the 'DEM method' described in the study of Chambers et al. (2020) presenting a quantitative evaluation of glacial z_0 values using data from two glaciers in Arctic Sweden. Unlike Smith et al. (2016b), the authors of this study calculated h^* by taking twice the standard deviation of elevations above the detrended plane. Therefore, the model calculates h^* for every row and then again takes the mean of the row values to generate one h^* value for each subarea and cardinal wind direction. All the further parameters (i.e. s, S and z_0) were calculated in the same way as in the Smith model.

Fitzpatrick

The fifth model (hereafter called Fitzpatrick model) applied in this thesis is based on the 'Block estimation' described in the study of Fitzpatrick et al. (2019). The authors are utilising LiDAR input data to determine the aerodynamic roughness length of two glaciers in Canada. While the two previous raster methods calculated some of the parameters row-wise, this method followed a moving-window approach. In other words, for each cell in the subarea a border of several cells in each direction was selected leading to a grid of cells (hereafter called subgrid) used to determine the z_0 value of the centre cell. Thus, the surrounding area of the cell is influencing the cell's aerodynamic roughness length value. Once the z_0 value of a centre cell is calculated the grid-window moves one cell further and continues with the same process.

The sheltering issue has been taken into account by only considering the part of the frontal area that is taller than the very first cell in each subgrid row, as illustrated in Figure 2.13b. The exact equation for the calculation of s looks as follows:

$$s = (\sum_{i=1}^{n} max(z_{ij}) - z_{i1}) * cellwidth, \tag{2.9}$$

where i is the column, j the row and n the total number of rows of the subgrid. In words, the height of the first line of cells in the subgrid sets the base level and the cell with the maximal height z in the same row sets the upper level. The difference between upper and lower level was then used to calculate s. The sum of each row's s values determined the s value for the centre cell which was calculated for each wind direction individually.

The obstacle height h^* corresponds to the mean of all the detrended elevation values above the zero plane within the subgrid. The ground area S is assigned to the area of the subgrid. Accordingly, for every cell a z_0 value was calculated. The final z_0 value of the subarea corresponds to the mean of the z_0 values of all its cells. This model is computationally more demanding than the other models but is considering the adjacent cells from all wind directions for the calculation.

The subgrid size (i.e. the block of adjacent cells) is defined by Fitzpatrick et al. (2019) as an average roughness element and its surrounding influence area. However, the DEM resolution in their study is about 4 times coarser than the one in this thesis. In addition, their investigated roughness elements are about one order of magnitude smaller. The authors found out that an increasing border thickness comes along with an increase in corresponding z_0 values. Therefore, the question appeared what a reasonable subgrid size for this model would be, given the input DEMs of this thesis. As already discussed with Figure 2.10 in Section 2.4, the roughness elements can only be properly represented if the subgrid size has at least the length of an average roughness element. Furthermore, roughness obstacles of the mapped tidewater glaciers have an average wavelength between 30 m and 50 m depending on the wind direction and glacier (see Table 3.2). However, a too large subgrid size (i.e. longer than the size of one roughness element) would not properly represent the surface roughness. This is because s is only calculated by subtracting the maximum value in each row from its front row value, as stated above. Given the heterogeneous roughness elements of the mapped tidewater glaciers this represents a challenge. As a compromise, it was decided to take a subgrid size of 30 m (i.e. 15 m border thickness to each side), which corresponds to the lower estimation of an average roughness element. Although it means that the moving window almost reaches the size of the subarea itself (i.e. over 100 pixels), this is assumed to be the best approximation according to the theory of Fitzpatrick et al. (2019).

2.6 Surface Energy Balance Model

A point surface energy balance model for glaciers was applied to visualize the impact of the obtained z_0 estimations on the surface ice melt rates. The model is described properly in the technical communication of Brock and Arnold (2000). Apart from z_0 values, the simple energy balance model only needs basic meteorological input data (Chambers et al., 2020), such as air temperature (°C), air vapour pressure (Pa), wind speed (m/s) and incoming shortwave radiation (W/m^2). The model is based on the aerodynamic bulk method, which is often used in glaciological studies (e.g. Arnold et al., 2006; Fitzpatrick et al., 2019; Radic et al., 2017). Thus, the resulting surface melt rate (MLT) can be obtained with the following surface energy balance equation (Brock and Arnold, 2000):

$$MLT = SWR + LWR + SHF + LHF, \tag{2.10}$$

where SWR and LWR are the net shortwave and longwave radiation fluxes, respectively. Further, the sensible and latent heat fluxes are expressed as SHF and LHF. For the calculation of the sensible and latent heat flux the obtained z_0 values are needed, based on the following evaluation of Munro (1989):

$$SHF = \frac{\rho c_p k^2 u_z T_z}{[ln(z/z_0) + \alpha_M z/\wedge][ln(z/z_t) + \alpha_H z/\wedge]}, \tag{2.11}$$

$$LHF = \frac{\rho \omega \lambda k^2 u_z (e_z - e_s)/P}{[ln(z/z_0) + \alpha_M z/L][ln(z/z_e) + \alpha_E z/L]}, \tag{2.12}$$

where ρ is the air density, c_p the specific heat capacity of air and k is the von Kármán constant. T_z, u_z and e_z correspond to the mentioned input data of temperature, wind speed and vapour pressure. z_t and z_e are scaling lengths for the aerodynamic temperature and humidity same as z_0 is the scaling length for aerodynamic roughness. Furthermore, e_s is the vapour pressure at

the glacier surface, ω is the molecular weight of water vapour to air and λ the latent heat of vaporization. The stability correction constants for momentum, heat and humidity are expressed with the parameters α_M, α_H and α_E, respectively (Brock and Arnold, 2000). Additionally, P is atmospheric pressure and $\wedge$ and L are the Monin-Obukhov length scales for SHF and LHF, accordingly (Obukhov, 1971). The expression z/L corresponds to the stability parameter that is defined as the height shear stress balancing buoyancy given that the boundary layer is stable (Hock, 2005; Obukhov, 1971). The two equations 2.11 and 2.12 highlight the importance of the aerodynamic roughness length to determine the heat exchange and surface ice melt on a glacier.

Model input data of temperature, air vapour pressure and wind speed were taken from the meteorological station (MET Norway, 2020) in the settlement Pyramiden, which is located close to Nordenskiöldbreen. This station is assumed to find similar weather conditions and thus input data as an according instrument in front of or even on the glacier. However, the mentioned meteorological station does not measure the incoming shortwave radiation. Therefore, this input dataset was taken from a similar station in Adventdalen (Janssonhaugen Vest), which is located a bit further south (MET Norway, 2020). The model was fed with input data from the first three days of July 2020. With this time frame it could be ensured, that air temperatures were positive. This is crucial for a meaningful exploration of the impact of surface roughness on turbulent heat transfer. Furthermore, the ice is assumed to be at the melting point. In the model all parameters apart from the z_0 values were hold constant to best highlight the impact of the surface roughness on the melt rates of a glacier.

Chapter 3

Results

3.1 Digital Elevation Models

Table 3.1: Attributes of the constructed DEMs for each glacier. The number of images belongs to the mapped area of the glacier, whereas the coverage area refers to the extract that effectively has been used for the surface roughness calculation (in particular important for Fridtjovbreen and Nordenskiöldbreen 2020).

Glacier	Date	No. of Images	Coverage Area (km^2)	Resolution (m/px)
Nordenskiöldbreen 2019	19.-22.08.2019	4024	2.6	0.17
Tunabreen	28.04.2020	2552	2.4	0.19
Heuglinbreen	04.05.2020	621	1.1	0.21
Fridtjovbreen	07.05.2020	1198	1.0	0.28
Nordenskiöldbreen 2020	21.07.2020	2028	0.9	0.22

The main results of the first step of this thesis are the constructed DEMs for each glacier and fieldwork date, which are shown in Figure 3.1 and Figure B.1 in Appendix B. The required ground sampling distance of 0.1 m/px for the captured images could be fulfilled on all glaciers with GSDs varying from 0.04 m/px to 0.07 m/px. As anticipated, this image resolution was necessary to achieve a certain DEM resolution. Table 3.1 summarizes, that apart from Fridtjovbreen with a pixel size of 0.28 m/px, all DEMs managed to adhere the desired resolution of 0.25 m/px. Thus, with the given pixel size it is easily possible to visualize the surface characteristics (i.e. crevasses) of the mapped glacier areas, as can be seen on Figure 3.1. Additionally, the size of area effectively used for the aerodynamic roughness length calculation varies for each glacier. The reasons can be found in the amount of mapping days (3 days on Nordenskiöldbreen 2019 and 1 day on all the other glaciers), battery capacity and GPS issues (on Heuglinbreen). Furthermore DEMs were cropped afterwards to focus on the most interesting areas (Fridtjovbreen and Nordenskiöldbreen 2020). In the end, the chosen DEM area has a significant impact on the resulting mean z_0 value of a glacier. Smooth glacier ice (e.g. at the upper part of Fridtjovbreen) decreases the overall z_0 average value of the glacier. This needs to be taken into account especially when comparing averaged roughness values between the glaciers.

Furthermore, the constructed DEMs illustrate that for all mapped glaciers the majority of the crevasses are aligned mostly perpendicular to the flow direction. In general, the crevasses closer to the front seem deeper and larger in terms of spacing (width of crevasse opening) compared

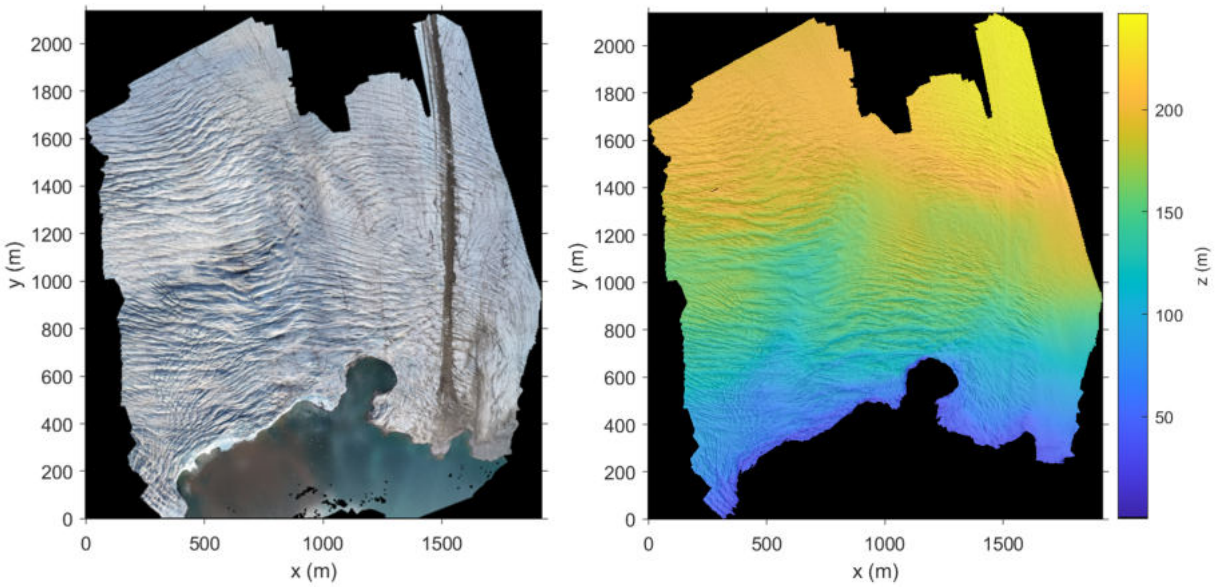

Figure 3.1: Orthomosaic (left) and DEM (right) of the crevassed glacier front area of Nordenskiöldbreen captured in summer 2019. The DEM was built with a SfM approach using high-resolution drone images. A hillshade layer was laid under the DEM for a better visualization of the crevasses. DEMs of Tunabreen, Heuglinbreen, Fridtjovbreen and Nordenskiöldbreen 2020 can be found in Appendix B.

to crevasses located further up the glacier (see Figure 3.1). However, there are some differences among the glaciers regarding the shape of the roughness elements and number of crevasses. Fridtjovbreen and Heuglinbreen are only heavily crevassed at the very lowest part of the glacier (i.e. the mapped area) whereas Tunabreen and Nordenskiöldbreen have many large crevasses a long way up the glacier and far beyond the area actually mapped with the drone. Furthermore, the crevasses on Tunabreen and Nordenskiöldbreen are deep (can be at least 30 m) and steep, whereas the crevasses on Fridtjovbreen and Heuglinbreen are less steep and can have a depth of at least 20 m. Therefore, the crevasse spacing is in general larger on the latter two glaciers compared to Tunabreen and Nordenskiöldbreen. However, the variability of crevasse spacing and shape across one glacier is large. Locally, the spacing can vary from some meters up to 70 m or more.

Table 3.2 shows average obstacle lengths and heights for each glacier calculated according to the zero-up-crossing transect method of Munro (1989). For wind directions up and down the glacier the roughness elements are a bit smaller with a length of about 30 m. For cross-glacier wind directions the average obstacles have length values of slightly more than 40 m. The heights of the roughness elements are larger in up- or down-glacier wind direction than for winds blowing across the glacier. In average, Tunabreen and Nordenskiöldbreen again show higher values than Fridtjovbreen. Heuglinbreen also has high average crevasse depth values with 14 m in up- and down-glacier wind direction. Nordenskiöldbreen has smaller mean roughness element in 2019 than in the following year, where a smaller and more heavily crevassed area was mapped (see Table 3.1). However, it needs to be considered that this is a rough and simple estimation of an average value for both height and length of roughness elements. On a local scale, the obstacle size can exceed the given values by far.

Table 3.2: Attributes of mean length and height values of roughness elements on each mapped extract of the glaciers. All values are shown in the unit meters.

Glacier	Height cross	Height up/down	Length cross	Length up/down
Nordenskiöldbreen 2019	7	10	41	29
Tunabreen	11	14	43	37
Heuglinbreen	9	14	35	31
Fridtjovbreen	6	8	46	29
Nordenskiöldbreen 2020	9	16	49	35

3.1.1 Validation of Digital Elevation Model Accuracy

For this thesis no georeferencing with GCPs was used to build the DEMs. So, the on-board GPS and the measurements of camera orientation were solely responsible for the georeferencing. The positional accuracy of the DEM is limited by the on-board GPS with a hover accuracy of ± 1.5 m horizontally and ± 0.5 m vertically for both drones (DJI, 2017, 2019). Under these conditions, the software manages to build the DEMs in the correct shape. However, scale, translation and rotation are arbitrary with respect to a geographic coordinate system (James et al., 2017). Since the DEM is rotated and clipped before the z_0 model implementation, translation and rotation are not impacting the results. Therefore, only the uncertainty of the scale (i.e. distortion) is of importance for the results of this thesis.

Horizontal Accuracy

Since no GCPs or other reference control points were used it was not possible to run an appropriate DEM accuracy check. However, to still assess the extend of the possible scale deviation a visual approach was applied. Figure 3.2 illustrates the horizontal positional DEM accuracy on Tunabreen, which has a large horizontal extend of more than 3.5 km. Therefore, the obtained DEM was laid over a Sentinel-2 satellite image (ESA, 2020), which has a resolution of 10 m. The blue line represents the glacier front line of the Sentinel-2 satellite image (captured on April 24, 2020) and the red line refers to the front line of the DEM (April 28, 2020). The satellite images might also have some accuracy uncertainties, but these are generally very low. Therefore, this issue was not pursued deeper in the thesis and the satellite image assumed to be free of distortion. While as a rough estimate, the DEM is matching the satellite image, a closer comparison between the two layers provides some horizontal deviations. To a large part the observed error seems systematically, as the blue line is constantly about 30 m in front (further in southwestern direction) of the red line. However, on both edges of the mapped area the red line is located further outside, indicating a relative distortion with respect to the satellite image.

This phenomenon must occur mostly close to the border of the glacier because Figure 3.2 shows that in the middle part the two lines correspond better to each other (e.g. the small bay to the left of the centre). However, a distortion of about 60 m across a horizontal distance of 3500 m corresponds to a relative length change of 1.7 %. This raises the question of the impact of such a distortion on the resulting z_0 estimations. To investigate this effect a small test study on a minimum working example on Tunabreen (2000 px x 2000 px) for the Smith and Munro model and averaged wind directions has been conducted and the results are summarized in Table 3.3. To do so, the original DEM was manually distorted in both horizontal and vertical direction by ±1 %, ±5 % and ±10 %, respectively. The vertical distortion leads to a systematic deviation in

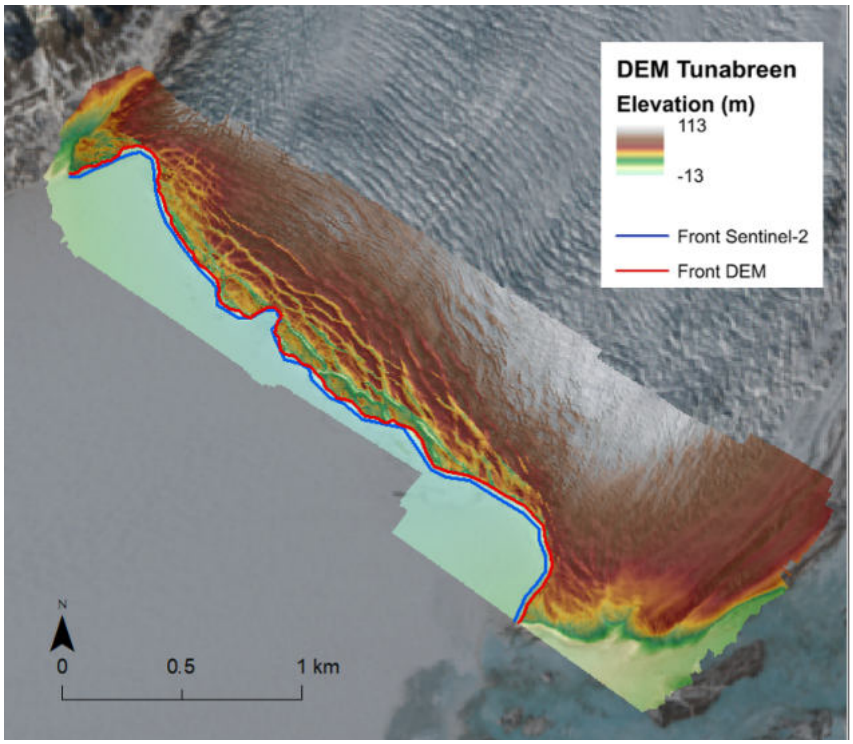

Figure 3.2: Illustration of the horizontal positional deviation between the constructed DEM and the underlaid Sentinel-2 satellite image (ESA, 2020). The glacier front line of the DEM (red) and the satellite image (blue) are highlighted.

z_0 values which is approximately twice as large as the DEM distortion (in percent). In other words, a distortion of 2 % leads to a deviation of z_0 values of 4 %. The test study results of the horizontal distortion revealed more random z_0 values. However, they still fit in the same range as the vertical deviations. In summary, the experiment shows that the influence of a small distortion of a few percent on the resulting z_0 values is relatively minor.

Vertical Accuracy

The vertical DEM accuracy is hard to determine because neither the glacier surface nor the water surface (tide) are on a constant elevation in time. Therefore, no stable reference point is available. To visualize these shortcomings, a small investigation on the DEM of Fridtjovbreen was conducted. Figure 3.3a illustrates that the DEM construction of Fridtjovbreen that just used the internal GPS system of the drone (i.e. no GCPs and no further adaptations) leads to a z-axis that is substantially shifted. This can be seen on the legend showing that the sea ice is located at a height of roughly 95 m instead of slightly above zero.

In a second approach which is illustrated on Figure 3.3b, control points were artificially added in front of the glacier. Therefore, the sea level in summer was assumed to be at 0 m a.s.l while the sea ice in spring was assumed to be one meter thick, whereas x- and y-coordinates were still provided by the internal GPS system. This assumption comes along with a specific uncertainty in the order of magnitudes of meters. According to Agisoft Metashape, the resulting model accuracy of the artificial control points set on the sea level have an additional vertical error of up to one meter (assuming the artificial control points are correctly referenced). However, using this

Table 3.3: Sensibility of DEM distortion on z_0 estimation. The test study was determined on a minimum working example (2000px x 2000px) on Tunabreen. The original DEM was horizontally and vertically distorted by ±1 %, ±5 % and ±10 % and the corresponding DEMs were run with the Smith and Munro model. The z_0 values reported in this table were averaged in all wind directions.

Distortion	Smith vertical (m)	Munro vertical (m)	Smith horiz. (m)	Munro horiz. (m)
z_0: original	0.233 (0.0 %)	0.766 (0.0 %)	0.233 (0.0 %)	0.766 (0.0 %)
z_0: +1%	0.237 (+2.0 %)	0.782 (+2.0 %)	0.232 (-0.4 %)	0.764 (-0.3 %)
z_0: -1%	0.228 (-2.0 %)	0.751 (-2.0 %)	0.232 (-0.1 %)	0.759 (-0.9 %)
z_0: +5%	0.256 (+10.2 %)	0.845 (+10.3 %)	0.208 (-10.6 %)	0.697 (-9.1 %)
z_0: -5%	0.210 (-9.8 %)	0.691 (-9.7 %)	0.243 (+4.3 %)	0.791 (+3.3 %)
z_0: +10%	0.281 (+21.0 %)	0.927 (+21.0 %)	0.195 (-16.0 %)	0.662 (-13.6 %)
z_0: -10%	0.188 (-19.0 %)	0.621 (-19.0 %)	0.254 (+9.3 %)	0.825 (+7.7 %)

approach, the resulting DEM is finally located in a reasonable vertical range from slightly below zero up to 100 m. More importantly, it can be seen that the elevation ranges (i.e. maximum-minimum) of both DEMs correspond well. This deviation indicates a systematic offset rather than random distortion. In other words, both figures show an elevation range of roughly 105 m.

Furthermore, in Figure 3.3c the two DEMs were subtracted from each other with the mean value set to zero. There it is visible, that the systematic error compensates for the largest part of the deviation in z-axis. The remaining difference is not exceeding the uncertainty of some meters (here four meters). A systematic error is of no matter for the approach used in this thesis as only the relative distances in between the roughness elements are used for further calculations. In any case, the approach conducted in Figure 3.3b only helped to reduce the vertical systematic offset of the DEM. However, since the accurate height of glacier front is not known due to lack of reference points, there could still be a vertical distortion that was not possible to determine.

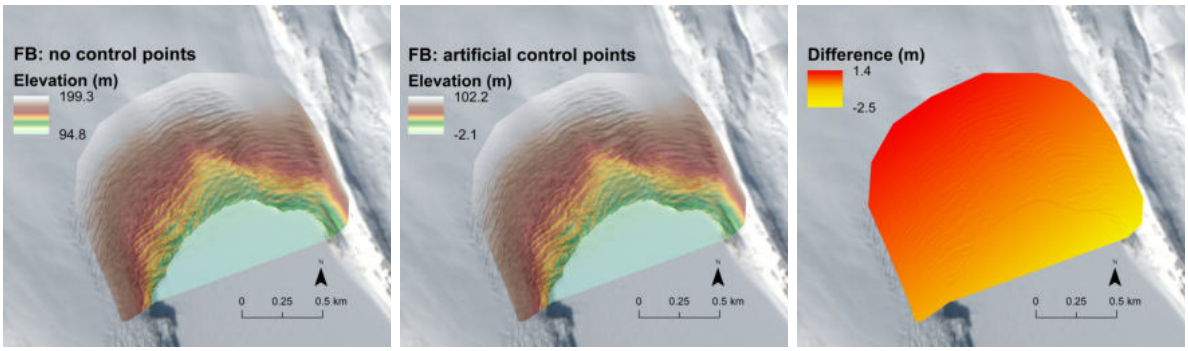

(a) (b) (c)

Figure 3.3: Visualization of the impact on the z-axis of artificially added control points (b) used for the calculation of the DEM. The legends of Figure (a), which has no control points added and (b) show the different range of elevation values. However, the relative elevation range (maximum-minimum) is similar and differences in the maps are hard to find, what indicates a systematic offset error. The third figure (c) shows the difference between the two DEMs with its mean value set to zero. All three figures have the Sentinel-2 satellite image (ESA, 2020) as reference base layer.

3.2 Aerodynamic Roughness Length

The aerodynamic roughness length was calculated for four tidewater glaciers by five models and for the four cardinal wind directions. Table 3.4 provides an overview of the estimated mean z_0 values for each model and glacier averaged in all wind directions. First of all, it can be seen that the resulting mean z_0 values vary up to one order of magnitude between different glaciers and calculation models. Furthermore, the estimated z_0 estimations can be distributed into two groups. The results from the Munro and Lettau model, both belonging to the transect method, are higher than those of the Smith, Chambers and Fitzpatrick models generated with the raster method. In more detail, Table 3.4 shows that the transect method leads to mean z_0 values from 0.17 m to 0.63 m. The estimated average z_0 values for the raster method range between 0.05 m and 0.19 m averaged in all wind directions. The same trend can be observed if only one specific wind direction is observed (see Figure C.13 in Appendix C). Figure 3.4 illustrates the down-glacier mean z_0 values for all glaciers and models. Thus, it can be seen that mean z_0 values vary between 0.08 m and 0.28 m for the raster method and 0.25 m to 0.88 m for the transect method (see also Table C.1 in Appendix C).

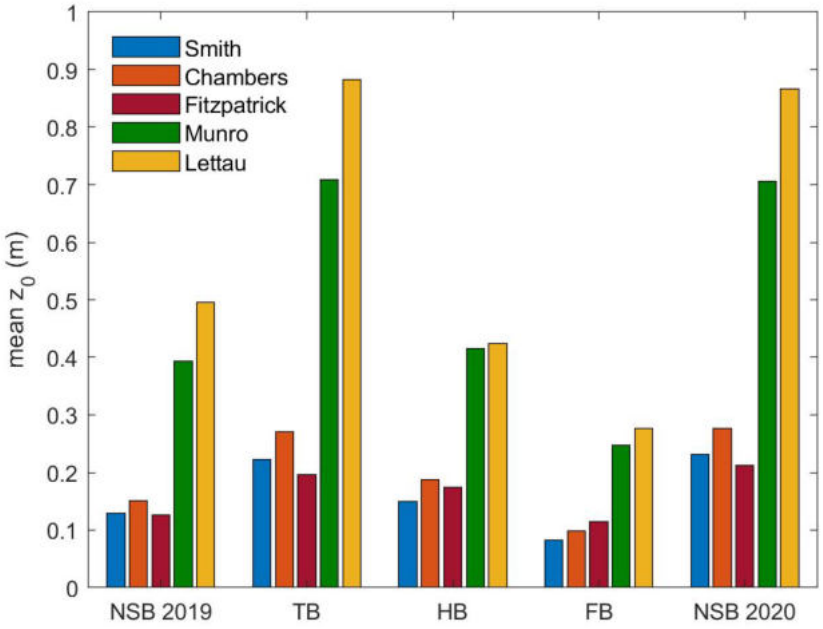

Figure 3.4: Mean z_0 values for the down-glacier wind direction applied for each model on Fridtjovbreen (FB), Heuglinbreen (HB), Tunabreen (TB) and Nordenskiöldbreen (NSB) in 2019 and 2020, respectively.

So far, only averaged z_0 estimations across one glacier were addressed. However, Table 3.4 further illustrates the spread of obtained subarea z_0 values across one glacier and model. Often, the standard deviation (Std) as well as the interquartile range (IQR) reach about the size of the mean value itself or even slightly exceed it. Figure C.5 in Appendix C illustrates this by plotting mean against Std z_0 values for all glaciers and models in the down-glacier wind direction. Thus, it can be seen that all data values are located around the 1:1 line. This indicates that the variability of the subarea z_0 values across each glacier is substantial. However, parameters like wind direction, subarea grid size and the location within the glacier also have a large impact on the obtained z_0 values and thus were further investigated below.

Table 3.4: Summary of z_0 values for each glacier and model averaged in all wind directions. The standard deviation (Std) and the interquantile-range (IQR) are two parameters to estimate the spread of the z_0 values across the mapped area.

Glacier	Parameter	Smith	Chambers	Fitzpatrick	Munro	Lettau
Nordenskiöldbreen 2019	Mean (m)	0.083	0.099	0.081	0.259	0.326
	Std (m)	0.140	0.161	0.174	0.423	0.639
	IQR (m)	0.084	0.102	0.072	0.274	0.315
Tunabreen	Mean (m)	0.154	0.187	0.143	0.508	0.625
	Std (m)	0.207	0.250	0.215	0.699	0.955
	IQR (m)	0.176	0.211	0.151	0.573	0.680
Heuglinbreen	Mean (m)	0.097	0.120	0.111	0.280	0.295
	Std (m)	0.111	0.137	0.154	0.308	0.454
	IQR (m)	0.119	0.147	0.125	0.327	0.306
Fridtjovbreen	Mean (m)	0.054	0.065	0.076	0.168	0.183
	Std (m)	0.075	0.091	0.177	0.223	0.379
	IQR (m)	0.076	0.088	0.078	0.241	0.230
Nordenskiöldbreen 2020	Mean (m)	0.140	0.168	0.131	0.441	0.542
	Std (m)	0.180	0.216	0.216	0.544	0.729
	IQR (m)	0.148	0.178	0.130	0.490	0.594

3.2.1 Model Variability

Five different models were used to calculate the aerodynamic roughness length. Thus, the impact of different calculation approaches on the results could be investigated. Figure 3.5 shows a map of the subarea z_0 values for each model of a down-glacier wind direction on Nordenskiöldbreen 2019 (for other glaciers see Figures C.4, C.7, C.9 and C.10 in Appendix C). Thus, every subarea of the map got colourized according to its z_0 value from red (low) to yellow (high) values. The results reveal that all models agree on the spatial z_0 patterns across a glacier. Accordingly, for the flatter and less crevassed part (e.g. to the right of the mapped area on Nordenskiöldbreen) all models show lower z_0 values (red) compared to the heavily crevassed part close to the glacier front (yellow). To further investigate the relative agreement between the models a statistical correlation test on the z_0 data of Nordenskiöldbreen (averaged in all wind directions) was conducted. The results are listed on Table 3.5 and confirm the statement of relative agreement between the models. The table shows the correlation R^2 of the subarea z_0 values between each pair of models. All models are strongly correlated to each other leading to R^2 values of 0.877 (between Chambers and Lettau) and higher. The high correlation could also be detected between the raster and transect method, especially for the Munro model. This means that throughout all the models, high and low relative z_0 values are found on the same subareas across the glacier. A similar correlation has also been observed on the other glaciers.

Despite the large relative agreement on z_0 values, the absolute values differ substantially. This can again be seen on the map of Nordenskiöldbreen for a down-glacier wind direction illustrated on Figure 3.5. The absolute values of the models Munro and Lettau show higher roughness values on a same subarea than the other three models. The difference can locally be up to one order of magnitude. The three models of the raster method provide subarea z_0 values of about 1 mm for slightly crevassed areas and 1 m for really heavily crevassed areas. The same spots calculated with the two transect methods produced z_0 values from 10 mm (slightly crevassed) up to 10 m (heavily crevassed). The same effect can be found when looking at the mean z_0 values averaged

Table 3.5: Correlation R^2 between calculation models of subarea z_0 values averaged in all four cardinal wind directions on Nordenskiöldbreen. The Munro and Lettau model belong to the transect method, while the other models are based on the raster method.

Model	Smith	Chambers	Fitzpatrick	Munro	Lettau
Smith	1	0.998	0.996	0.999	0.899
Chambers	0.998	1	0.996	0.998	0.877
Fitzpatrick	0.996	0.996	1	0.996	0.996
Munro	0.999	0.998	0.996	1	0.887
Lettau	0.899	0.877	0.996	0.887	1

across the glacier. Figure 3.4 illustrates the down-glacier mean z_0 values for all glaciers and models. The figure shows that mean z_0 values vary about half an order of magnitude between the models. In general, the Smith model provides the lowest z_0 values followed by the Chambers model. The Fitzpatrick model is often close to the two other models of the raster method. Unlike them, the Fitzpatrick model cannot be put in a fixed order. In other words, the z_0 values of the Fitzpatrick model can either be lower or higher compared to the Smith and Chambers model depending on the glacier and wind direction. Furthermore, the Lettau model generally produces higher z_0 estimations than the Munro model. In summary, despite the clear relative agreement between the models, the estimated magnitude of the z_0 values varies substantially between the models.

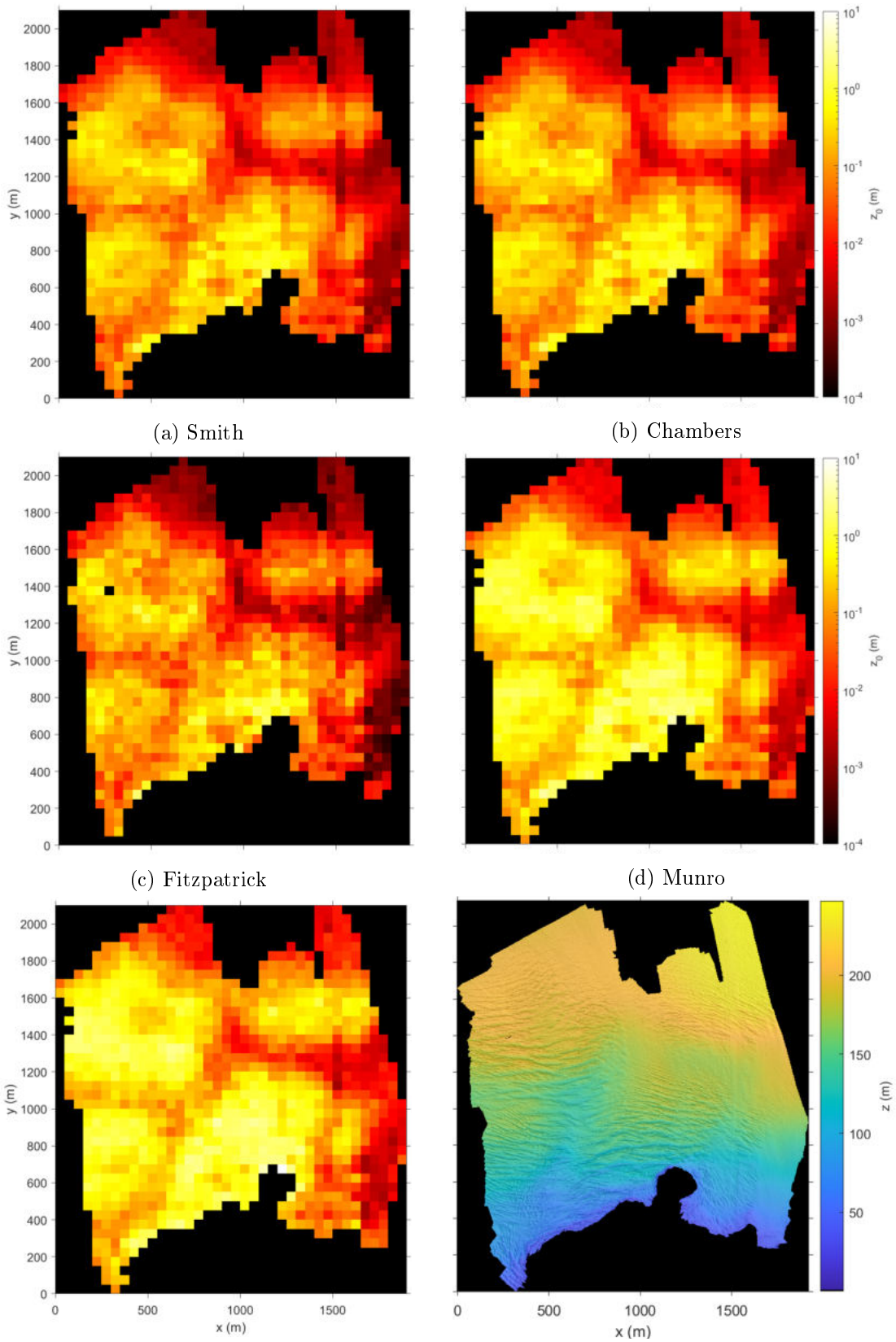

(a) Smith (b) Chambers

(c) Fitzpatrick (d) Munro

(e) Lettau (f) DEM

Figure 3.5: Variability of z_0 values for Nordenskiöldbreen (2019) depending on the calculation models Smith (a), Chambers (b), Fitzpatrick (c), Munro (d) and Lettau (e) for a subarea grid size of 50 m x 50 m and a down-glacier wind direction. Graph (f) shows the according DEM with the underlaid hillshade layer.

3.2.2 Glacier Variability

In this thesis z_0 values of four different glaciers have been estimated. Figure 3.4 not only provides insights about the model variability of z_0 values but also indicates that there is some variability among the mapped glaciers (see also Table C.1). The results show that the mean z_0 values for the Smith model and down-glacier wind direction are somewhat larger on Tunabreen (22.3 cm) and the extract of Nordenskiöldbreen mapped in 2020 (23.1 cm) compared to the other glaciers. The same mean z_0 values on Nordenskiöldbreen measured in 2019 are lower with only 12.9 cm. Heuglinbreen (15.0 cm) and especially Fridtjovbreen (8.2 cm) show lower mean z_0 values than the glaciers mentioned above.

The mapped glaciers all vary in size of area, mostly due to mapping time (see Table 3.1). These areas were cropped to an extent where they to a large part are heavily crevassed (i.e. only little non-crevassed areas), because that corresponds to the main focus of this study. However, there are still parts of the glacier that are less heavily crevassed (e.g. upper part of Fridtjovbreen or right part of Tunabreen) influencing the estimation of an average z_0 value of the mapped glacier. Therefore, it is helpful to also have a look at the local subarea z_0 values on each glacier in order to determine the aerodynamic roughness length differences among the glaciers. Figure 3.6 shows the map of subarea z_0 values for a down-glacier wind direction calculated with the Smith model. There it can be seen that all glaciers show a similar range of z_0 values with decimeter to meter scale for heavily crevassed subareas and milimeter to centimeter scale for less crevassed subareas. In general, all the observed patterns recognized in further investigations below (e.g. impact of wind direction or subarea grid size on z_0 values) are independent of the chosen glacier and vary (if even) only in magnitude rather than relative patterns in between the glaciers.

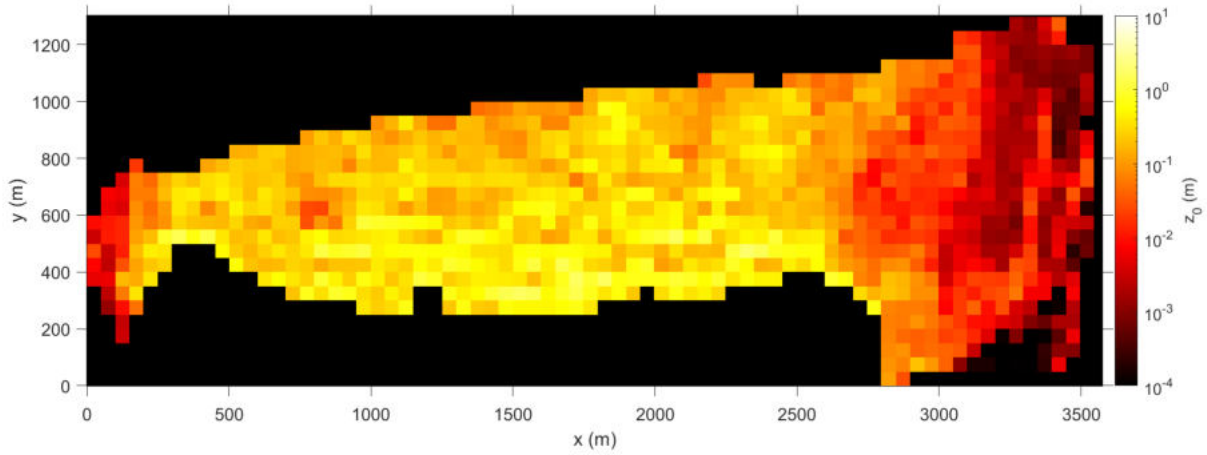

(a) Tunabreen

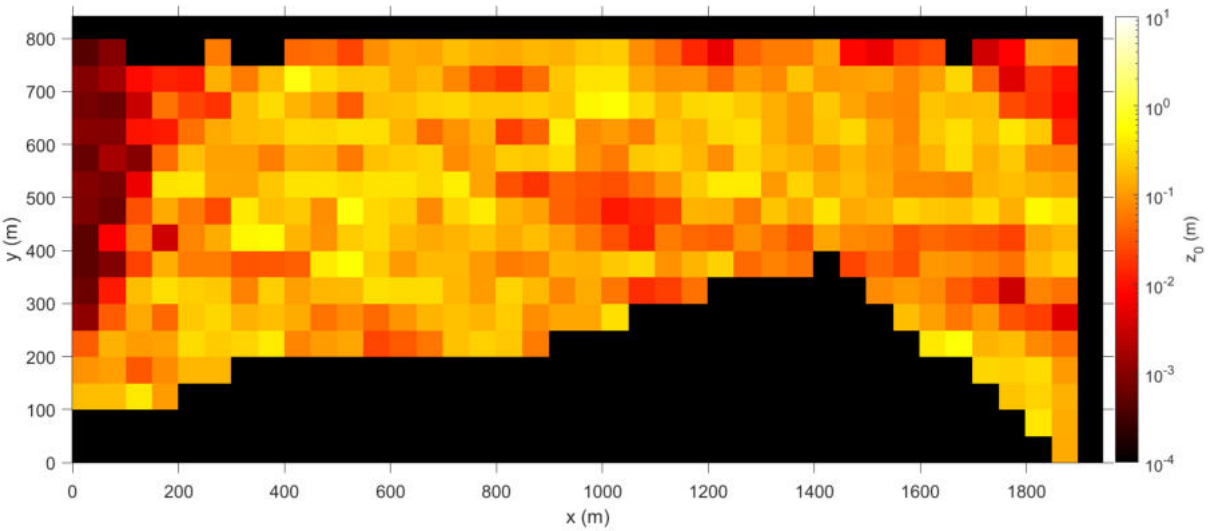

(b) Heuglinbreen

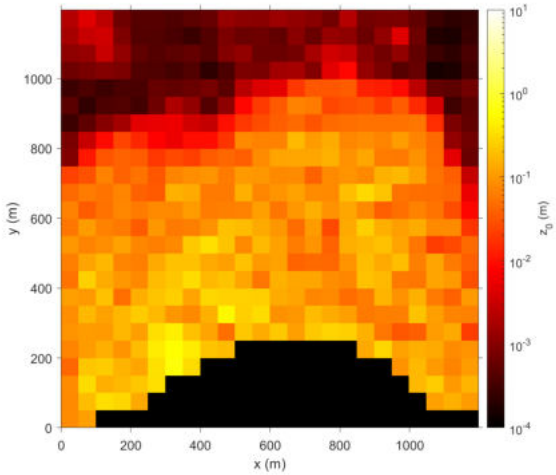

(c) Fridtjovbreen

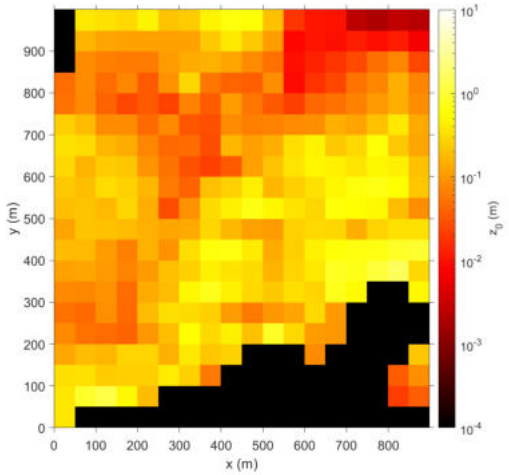

(d) Nordenskiöldbreen 2020

Figure 3.6: Variability of z_0 values for the glaciers Tunabreen (a), Heuglinbreen (b) Fridtjovbreen (c) and Nordenskiöldbreen 2020 (d) calculated with the Smith model for a down-glacier wind direction and a subarea grid length of 50 m.

3.2.3 Wind Direction Dependency

Since the roughness elements on the tidewater glaciers investigated in this thesis are very heterogeneous (see Table 3.2), each model calculated the subarea z_0 values for all four cardinal wind directions. Figure 3.8 shows the map of Fridtjovbreen with calculated subarea z_0 values of the Smith method for four cardinal wind directions. Thus, it is visible that z_0 values are higher for wind directions that face the crevasses perpendicularly (i.e. up- and down-glacier). Since crevasses are mainly oriented perpendicular to the flow direction, the mapped areas show a strongly anisotropic pattern of the glacier surface. This wind dependency effect is visible on all five applied models (see Figure C.2 in Appendix C for the Munro model). The measured four cardinal wind directions can be subdivided into two groups of similar z_0 values. Up- and down-glacier winds lead to higher z_0 values than wind directions crossing the glacier from the side. This pattern can be observed independent of the roughness element size and applied model. However, Figure 3.8 illustrates that larger roughness elements (i.e. area close to the glacier front and crevassed area in the centre of Fridtjovbreen) present a stronger wind dependency since they vary stronger with turning wind directions compared to areas that are less crevassed (i.e. upper part of Fridtjovbreen). In summary, the direction from which the wind is blowing has a large impact on the resulting aerodynamic roughness length values.

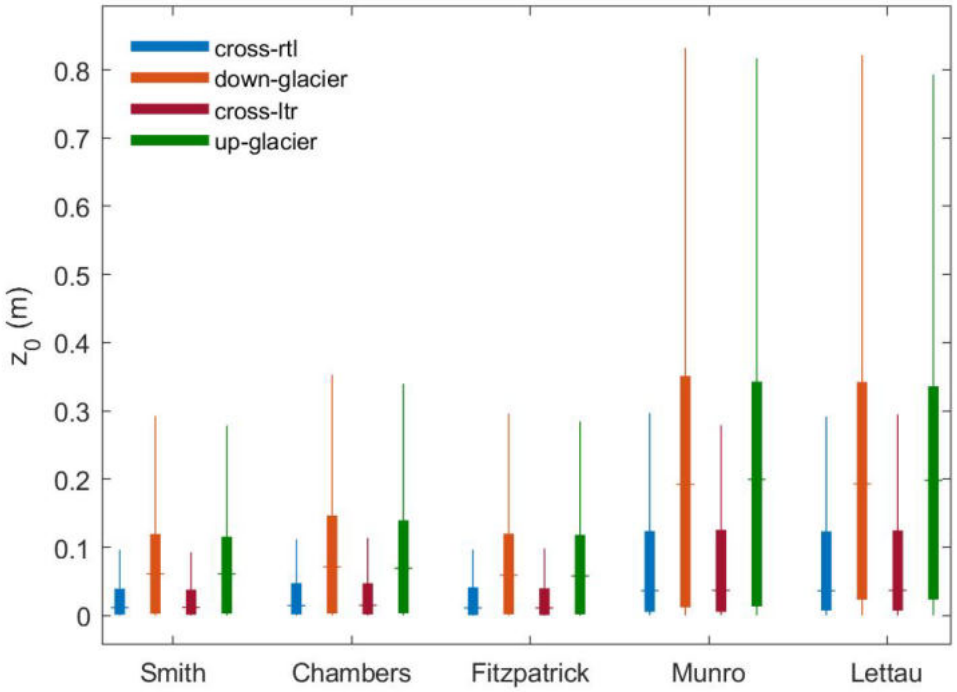

Figure 3.7: Boxplot visualization of subarea z_0 values for all four wind directions and each applied model determined on Fridtjovbreen. The wind direction is either down- (orange) and up-glacier (green) or cross the glacier from right-to-left (blue) and left-to-right (red).

Additionally, Figure 3.7 shows the boxplot graph of z_0 estimations illustrating the wind direction dependency of z_0 values on Fridtjovbreen (for other glaciers see Figure C.1). The boxplot z_0 medians of all models vary in a range of 1.2 cm to 3.7 cm for crosswind directions and 5.8 cm to 20 cm for up- and down-glacier wind systems. Therefore, aerodynamic roughness length values show a range of up to one order of magnitude for changing wind directions. The large dependency of estimated z_0 values on the chosen wind direction is observed throughout all models. In contrast

to the large differences between two perpendicular wind directions, Figure 3.7 shows that up- and down-glacier wind systems (left-to-right and right-to-left crosswinds, respectively) present z_0 values that are in very close agreement in between each other. Their mean and median values never differ more than 10 % and only rarely more than 5 % independent of the chosen model or glacier. In summary, it can be stated that the impact of wind direction on average or median z_0 values slightly exceeds the model variability. Locally however, both parameters can vary about one order of magnitude.

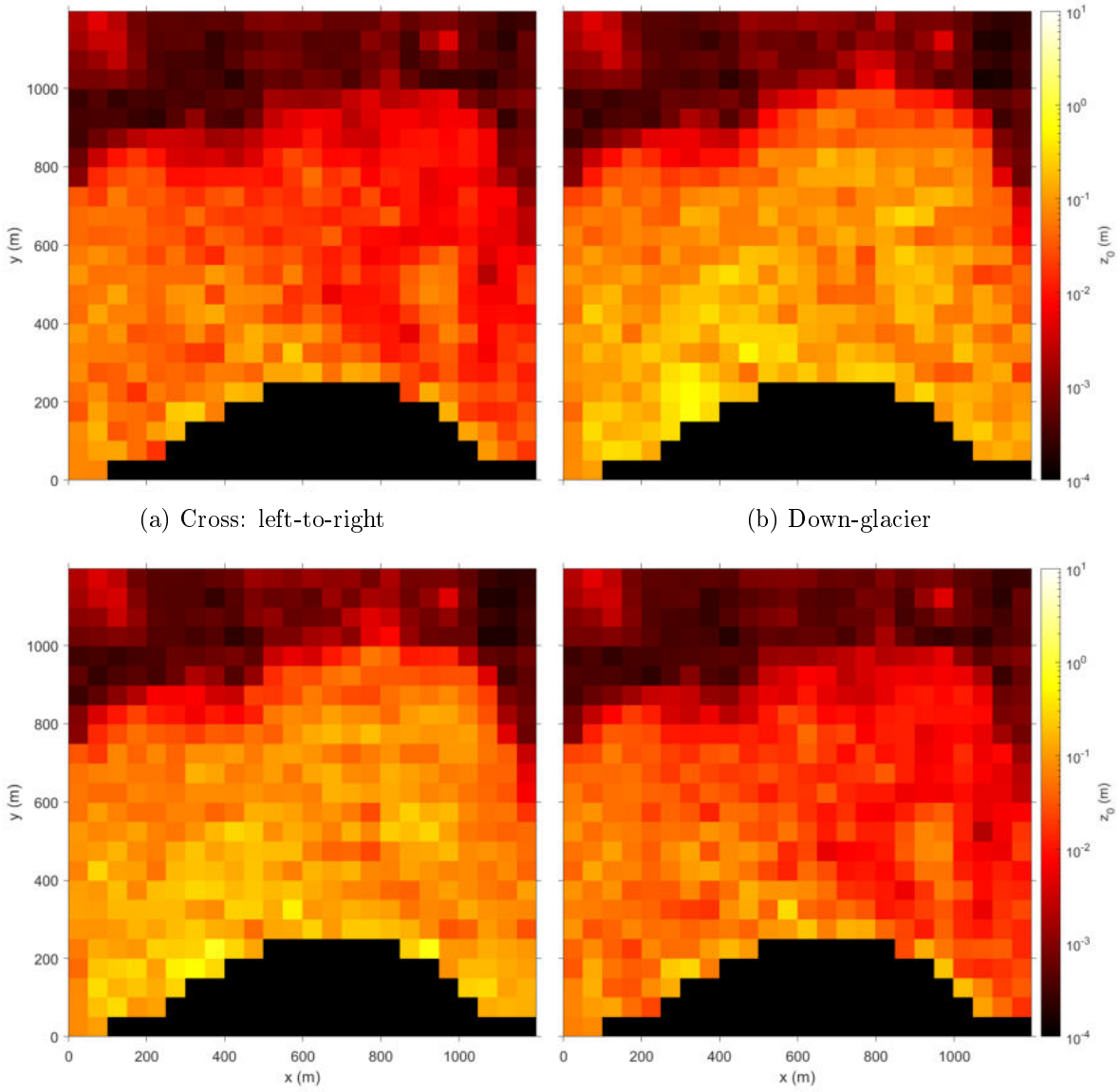

(a) Cross: left-to-right

(b) Down-glacier

(c) Up-glacier

(d) Cross: right-to-left

Figure 3.8: Variability of z_0 values for Fridtjovbreen depending on the wind direction for a subarea grid size of 50 m calculated with the Smith model. Winds blowing across the glacier either from the left to right (a) or right to left (d) produce smaller z_0 values than down- (b) or up-glacier (c) wind systems.

The following anisotropy ratio Ω was used to additionally investigate the trend in wind direction dependency for local subarea z_0 values (Smith et al., 2006):

$$\Omega = \frac{z_{01} - z_{02}}{z_{01} + z_{02}}. \tag{3.1}$$

The ratio compares aerodynamic roughness length of the mean parallel (z_{01}) and mean perpendicular (z_{02}) wind directions for every subarea. A ratio value of 0 means that the surface roughness is isotropic. A positive ratio towards 1 means the parallel winds (up- and down-glacier) are dominant and a negative ratio towards -1 means that perpendicular winds (cross-glacier) dominate. Figure 3.9 illustrates a histogram of the subarea Ω values on the example of Fridtjovbreen and for the Smith and Munro model. The results show, that the subarea z_0 values are strongly anisotropic all across the glacier whereas wind directions parallel to the flow direction are dominant. Almost all estimated subareas have larger values in parallel wind direction than in perpendicular (i.e. are positive). Both the raster (here Smith model) and the transect method (Munro) show a similar pattern with the highest frequency at the range of 0.4 to 0.7 (Smith) and 0.4 to 0.8 (Munro). Although Tunabreen has still mostly positive ratio values it is the glacier with the least anisotropic behaviour of all the glaciers.

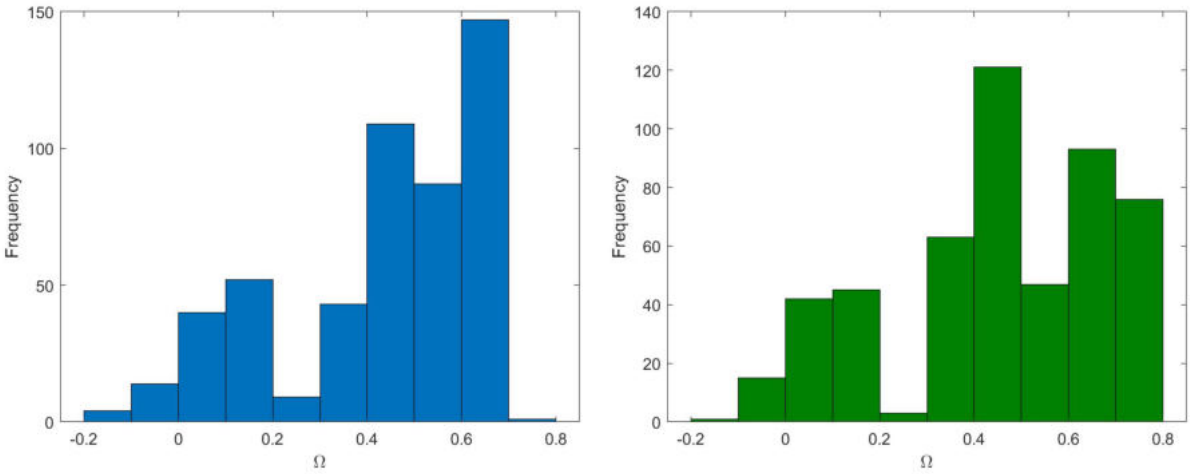

(a) Smith

(b) Munro

Figure 3.9: Anisotropy ratio values for the two models Smith (a) and Munro (b) calculated for subarea z_0 values on Fridtjovbreen. The further away the Ω values are from zero, the larger the anisotropy. A positive ratio towards 1 means that parallel winds (up- and down-glacier) are dominant over perpendicular winds (cross-glacier).

3.2.4 Grid Size Dependency of Subarea

The mapped glacier areas were divided into subareas with a grid size of 50 m x 50 m to account for the spatial variability of z_0 on the glacier. However, to investigate the grid size dependency of the subareas on z_0 values, a small case study on the glacier Fridtjovbreen was conducted. Therefore, z_0 values for varying grid sizes between 5 m and 150 m were calculated. Thus, Figure 3.11 illustrates the scale dependency of z_0 on the example of the Smith model for down-glacier wind directions on a map of Fridtjovbreen. To guarantee a better orientation a hillshade layer of the DEM has been underlaid. The resulting z_0 values show a strong dependency on the chosen grid size independent of the model, glacier and wind direction. The larger the chosen grid size

of the subarea, the larger the resulting z_0 values. Nevertheless, relative spatial patterns across the glaciers remain similar regardless of the chosen grid size. In more detail, a grid size of 5 m to 10 m mostly produces z_0 values in a scale of centimeters (apart from locally high values on the front or exceptionally steep crevasses). For larger grid sizes like 50 m or more, the estimated z_0 values tend towards a scale of decimeters. Thus, for a small grid size like 5 m, the relatively large z_0 values correspond well - as it is supposed to - with the steep fronts of the crevasses seen on the hillshade. This is especially distinct on the upper part of Fridtjovbreen where the ice surface is generally flat but interrupted by clearly shaped crevasses. In any case, for such a small grid size, z_0 values are representing microtopography on top of the roughness elements rather than the large-scale surface roughness of the objects themselves. However, the main focus of the thesis is on the large-scale roughness as already discussed with Figure 2.10.

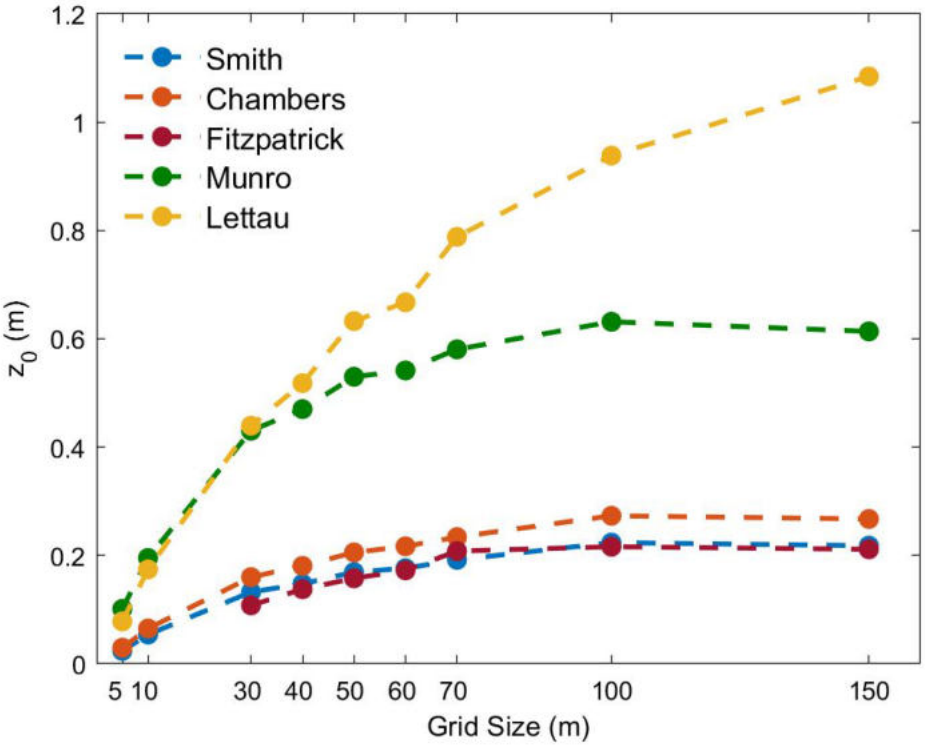

Figure 3.10: Scale dependency of mean z_0 values for the five applied models and a down-glacier wind direction on Fridtjovbreen with chosen subarea grid sizes from 5 m to 150 m. The z_0 values are increasing with larger grid size independent of the chosen model.

Figure 3.10 summarizes the mean z_0 results of the case study for the down-glacier wind direction. For all the models, the mean z_0 values increase by at least half an order of magnitude between a subarea grid size of 5 m and 150 m. All models show a similar pattern with strongly increasing z_0 values for small grid sizes (5 m to 30 m) and only slightly increasing estimates afterwards. In absolute terms, the two models from the transect method show a larger variability of z_0 with increasing grid size. Relatively seen however, the scale dependency variations between the models are not that pronounced. While the 5 m z_0 value of the Lettau model is only 7 % of the according 150 m value, the Smith model is with 11 % only slightly more robust. The Munro model shows the smallest relative change by increasing grid size as its 5 m z_0 value is 16 % of the value of a 150 m grid size. In summary, for grid sizes of about 70 m or more the z_0 values are loosing their strong scale dependency effect leading to stable z_0 estimations. The same effect is visible on Figure 3.11, where the chosen grid size of 50 m represents similar z_0 values (colors) as the higher

grid sizes for the same location while still providing a considerable grid resolution. Furthermore, on Figure C.11 the results of the grid size case study for a cross-glacier wind direction (left-to-right) are presented. This wind direction shows the same behaviour as the down-glacier wind direction, but the effect is less pronounced.

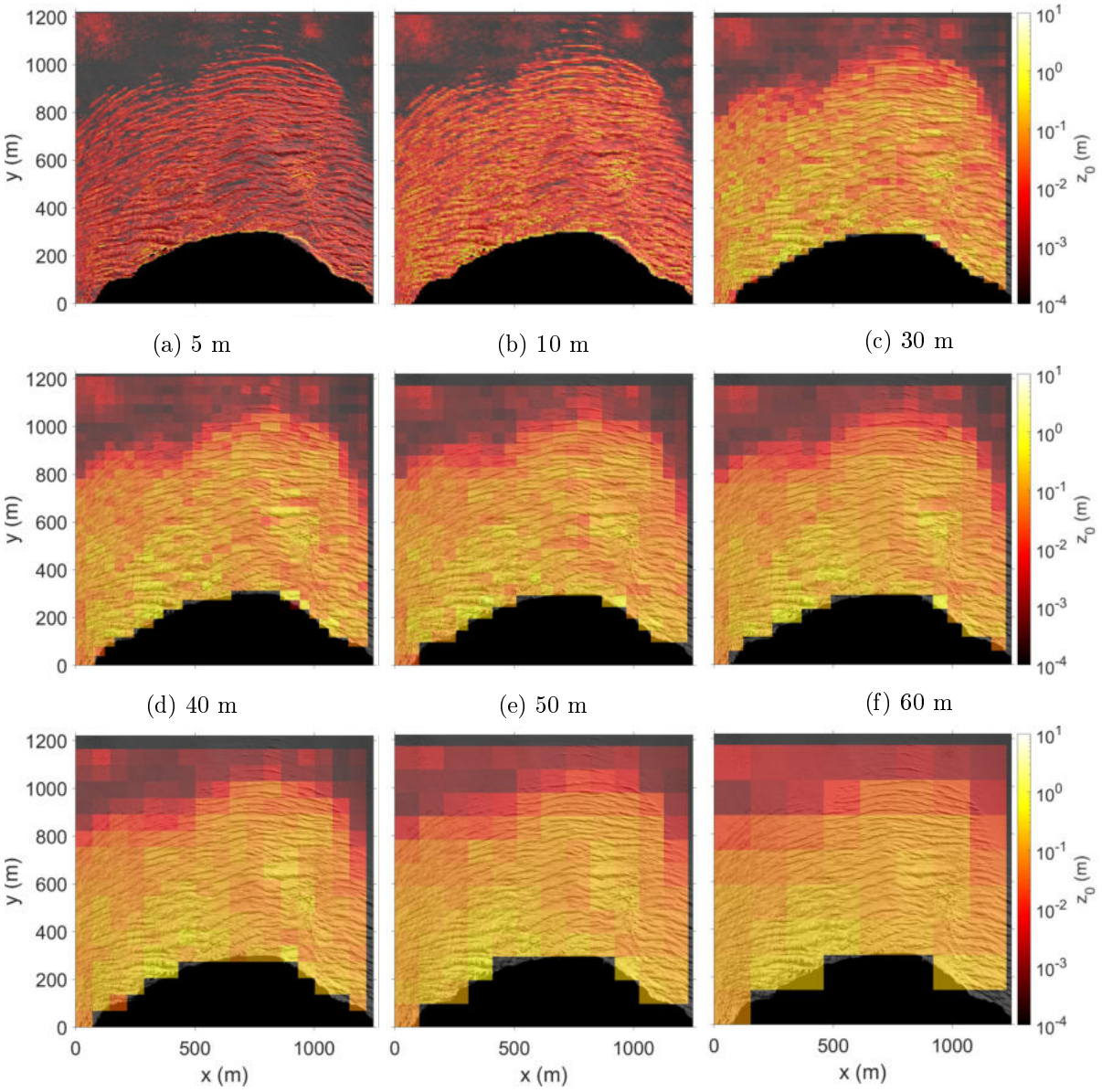

(a) 5 m (b) 10 m (c) 30 m

(d) 40 m (e) 50 m (f) 60 m

(g) 70 m (h) 100 m (i) 150 m

Figure 3.11: Scale dependent z_0 values for the Smith model and down-glacier wind direction applied on Fridtjovbreen for subarea grid size resolutions of 5 m (a), 10 m (b), 30 m (c), 40 m (d), 50 m (e), 60 m (f), 70 m (g), 100 m (h) and 150 m (i) with underlaid hillshade layer for orientation.

3.2.5 Temporal Variability on Nordenskiöldbreen between 2019 and 2020

Nordenskiöldbreen is the only glacier that has been visited twice during the three field campaigns. Thus, it provides insights on the temporal variability of z_0 values for two consecutive years. However, the investigations in this thesis focus on the yearly change of z_0 variability rather than the intra-annual deviation. Figure 3.12 shows the two DEMs of Nordenskiöldbreen in 2019 and 2020, respectively. The mapped area in summer 2020 (one day of fieldwork) was smaller compared to the field campaign approximately one year earlier in 2019 (three days of fieldwork). Therefore, only the overlapping area has been used for the temporal variability investigation. As a consequence, the resulting mean z_0 values of the clipped Nordenskiöldbreen 2019 DEM were higher compared to the mean z_0 values of the whole area. Additionally, to prevent any impact of different DEM resolutions, the DEM extract of Nordenskiöldbreen 2019 (0.17 m/px) was resampled to the resolution of the Nordenskiöldbreen 2020 DEM (0.22 m/px). The two DEMs in Figure 3.12 show that the roughness elements slightly changed shape and location during this year. However, after all the two DEMs look very similar.

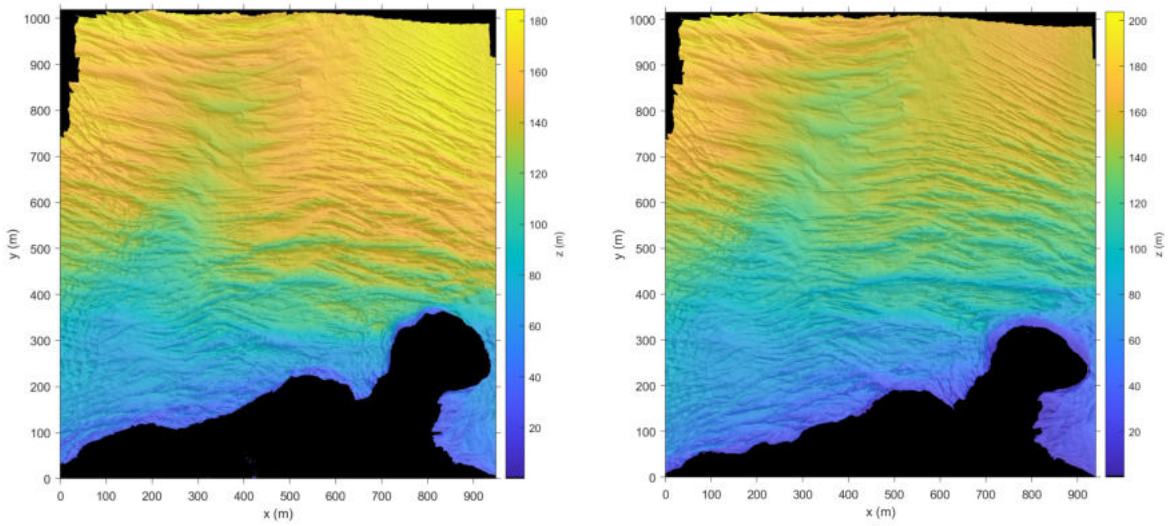

(a) Nordenskiöldbreen 2019

(b) Nordenskiöldbreen 2020

Figure 3.12: DEMs of the tidewater glacier Nordenskiöldbreen in 2019 (a) and 2020 (b) used for the calculation of the temporal z_0 variability. For a more accurate investigation, the DEM of Nordenskiöldbreen 2019 is clipped to the extend of the DEM of Nordenskiöldbreen in 2020. Again, a hillshade layer was laid under the DEMs for a better visualization of the roughness elements.

Figure 3.13 compares the mean and median z_0 values for a down-glacier wind direction and each model for the two years of data on Nordenskiöldbreen. First of all, the figure shows that the z_0 values on Nordenskiöldbreen are very similar for the two consecutive years. A closer look on the graph illustrates that both the mean and median z_0 values of all models on Nordenskiöldbreen were slightly higher in 2019 than in 2020. In contrast, only the median z_0 values of the Munro and Lettau model were somewhat higher in 2020. The same is valid for the up-glacier wind direction, whereas for the cross-glacier wind direction all mean and median z_0 values were higher in 2019. In more detail, the mean z_0 value for the Smith model and down-glacier wind direction in 2019 is with 0.25 m higher than the according value on the same area but one year later

(0.23 m). Relatively, the mean z_0 values never deviated more than 20 % and mostly even less than 10 % between the two years. In summary, the differences in produced z_0 estimations across the used models exceed the temporal z_0 variability by far, independent of the model calculation.

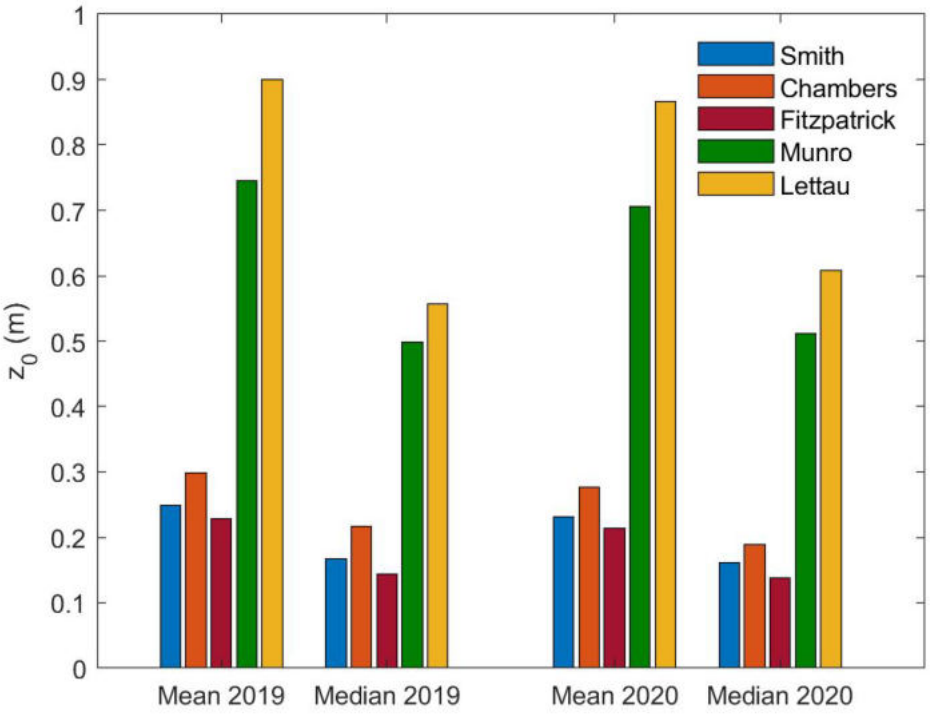

Figure 3.13: Temporal variability on Nordenskiöldbreen with data gathered in summer 2019 and 2020. The plotted data show the mean and median z_0 values for the down-glacier wind direction and each model. Please note that for meaningful comparison the data of Nordenskiöldbreen 2019 was clipped to the extent of the area mapped in 2020.

Figure 3.14 compares the two corresponding maps of the Smith model for a down-glacier wind direction, which show really similar z_0 subarea values. The relative high and low z_0 values can be found in the same subareas (from top right corner towards left bottom corner). Furthermore, Figure 3.13 shows that the median z_0 value is always lower than the corresponding mean value for each glacier, model and wind direction. The mean is an average measure that is prone to outliers. However, for the approach followed in this thesis high outlier z_0 values (i.e. from the glacier front or large crevasses) are of particular interest and have an important contribution to the actual melt rate of the glacier and therefore should not be excluded.

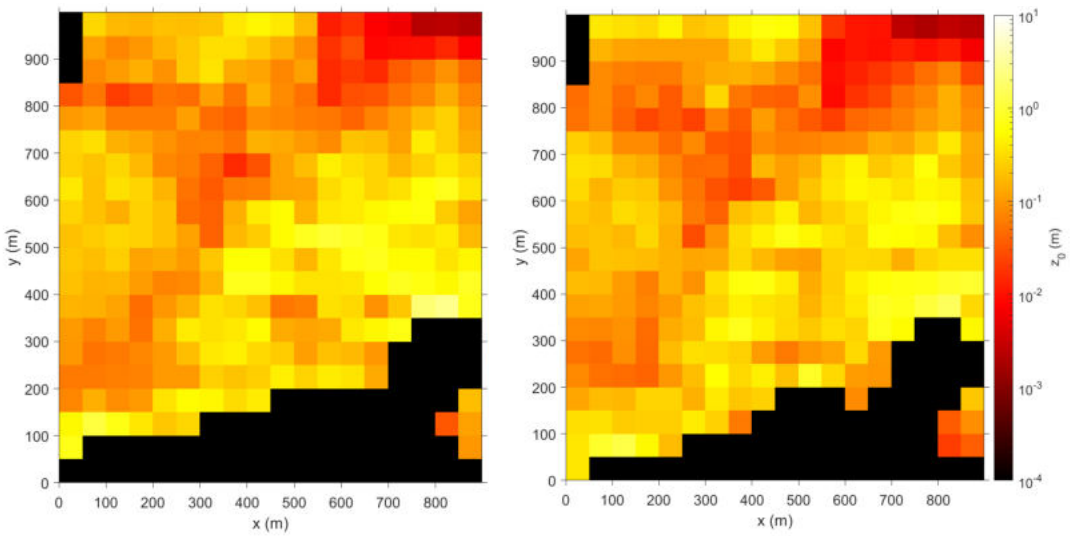

(a) Nordenskiöldbreen 2019

(b) Nordenskiöldbreen 2020

Figure 3.14: Temporal variability on Nordenskiöldbreen with data gathered in summer 2019 and 2020. The plotted data show z_0 values for the down-glacier wind direction calculated with the Smith model. To compare the results, the mapped area from 2019 (a) was clipped to the extent of the mapped area of 2020 (b) before running the calculation.

3.2.6 Characteristic Surface Features

One main advantage of the surface roughness approach followed in this thesis is to present spatial variability of z_0 values across the glacier rather than just one single value for the whole mapped glacier area. Several figures (e.g. Figure 3.6 and 3.7) show that the spatial variability of z_0 values across the mapped area is huge, with a range of up to three (locally even four) orders of magnitude. Figure C.8 further illustrates this variability by presenting a histogram overview of subarea z_0 values on Nordenskiöldbreen (2020) for each cardinal wind direction calculated with the Smith model. Thus, it can be seen that low z_0 values are very frequent, but locally they reach values of up to 0.8 m. In general, the larger a roughness element the larger its aerodynamic roughness length. The highest values were calculated with the transect methods and for winds blowing parallel to the flow direction of the glacier. Thus, locally where roughness elements are large the estimated z_0 values reach a length of one meter and more. Such values can be found close to the glacier front where crevasses are big and steep. The lowest values are estimated with the raster methods for smooth, crevasse-free ice often on the edges or upper parts of the mapped areas.

Several locations (plots of 50 m x 50 m) on Nordenskiöldbreen (2019) were selected in order to determine z_0 values of certain surface features and to highlight the spatial variability across the glacier. The according DEM extracts of five different surface characteristics can be found on Figure 3.16. The sites were selected in a way to predominantly find the according surface feature. The resulting z_0 estimations calculated for all models can be found in Figure 3.15. Thus, the models of the raster method estimated z_0 values in a milimeter scale for debris-covered ice (DCI) on a medium moraine. Small roughness elements like melt water channels (MWC) or small crevasses (SC) can usually be found in flatter parts of the tidewater glacier or further away from the glacier front. They have an estimated aerodynamic roughness length of up to one centimeter. Further, heavily crevassed (HC) plots, that can usually be found close to the

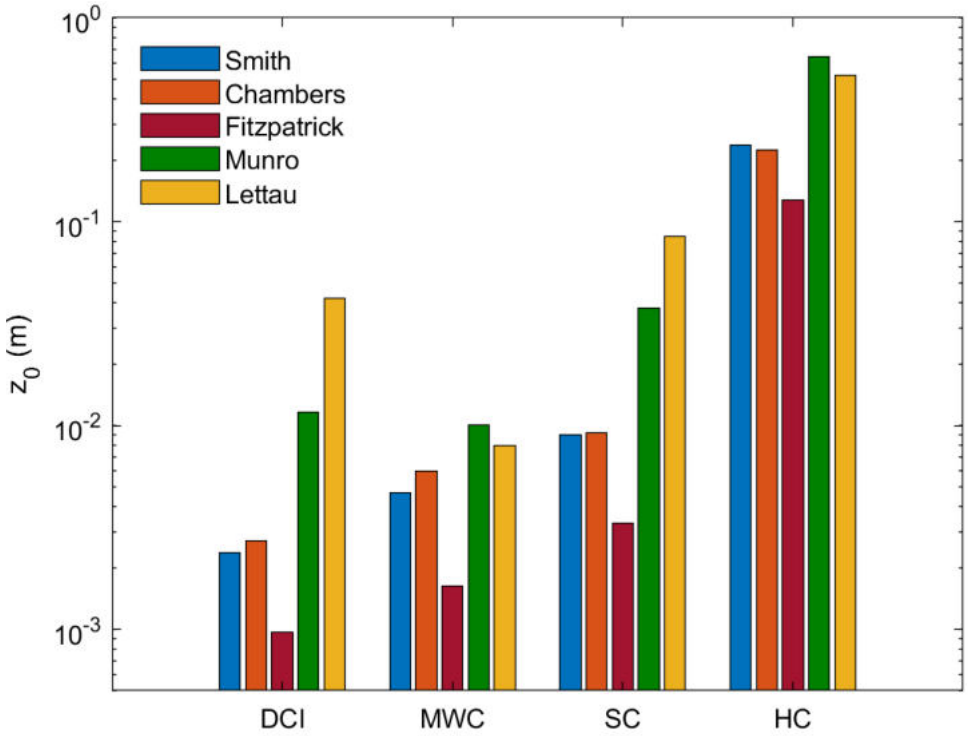

Figure 3.15: Spatial variability of z_0 values for different surface features (plots of 50 m x 50 m) on Nordenskiöldbreen. For each model and for a down-glacier wind direction the following surface characteristics were measured: debris-covered ice (DCI), melt water channel (MWC), slightly crevassed (SC) and heavily crevassed (HC) areas. Note the logarithmic scale on the y-axis.

glacier front, produced z_0 values in the scale of several decimeters. For non-crevassed areas with a rather smooth ice surface (i.e. snow covered and flat), which for instance can be found on the upper part of Fridtjovbreen, z_0 values drop even further than those for debris-covered ice ($<$ 0.5 mm). While the transect methods estimated z_0 values that are larger for debris-covered ice than for melt water channels it is reverse for the raster methods. The stated values are valid for a down-glacier wind direction. For perpendicular wind directions, the differences in aerodynamic roughness length values are still visible in the same order, but are lower in absolute values compared to the down-glacier wind direction (see Figure C.12 in Appendix C). In particular, z_0 values of the crevasses (for both slightly and heavily crevassed) decrease a lot if the wind blows crosswise over the glacier.

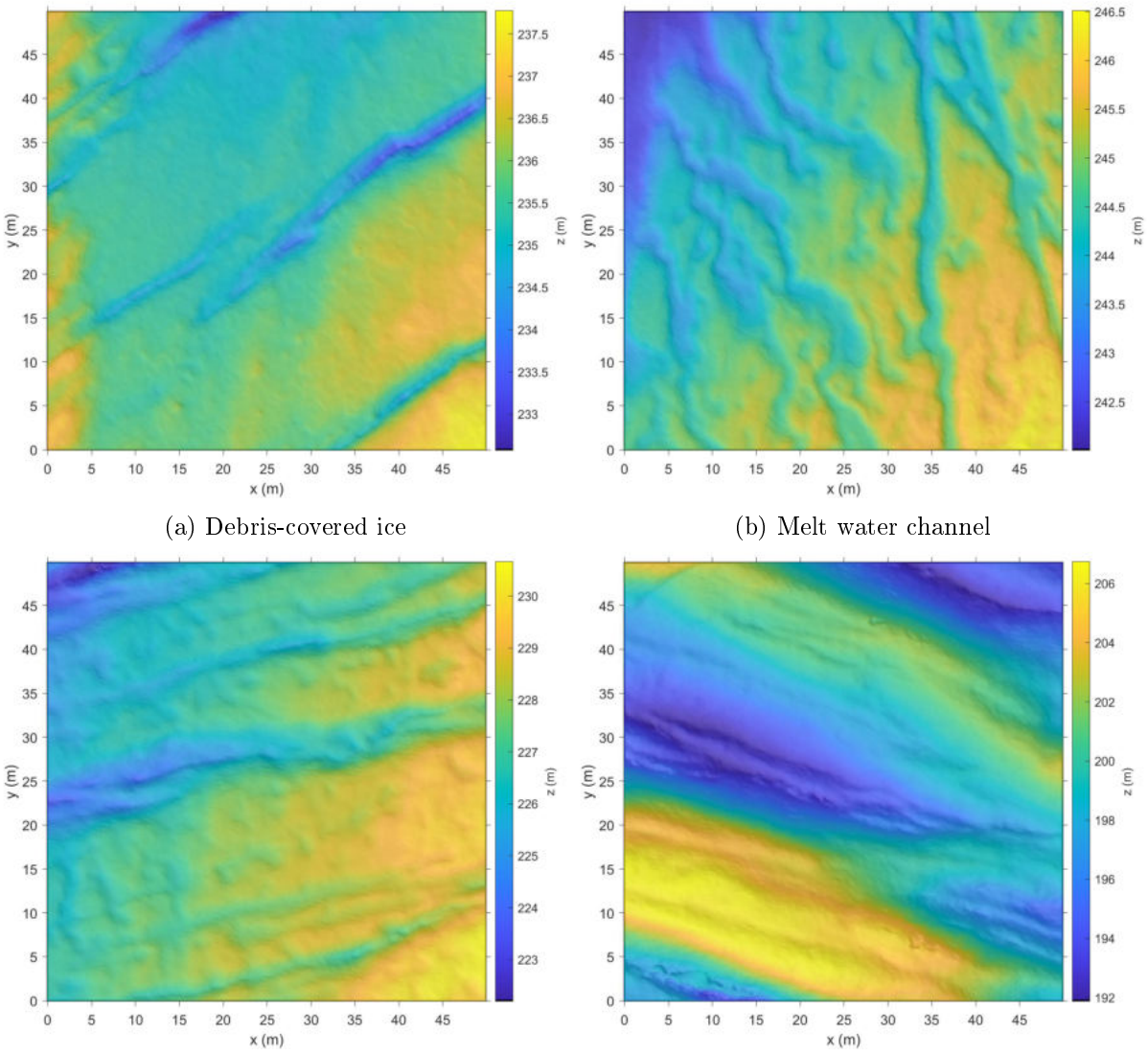

(a) Debris-covered ice

(b) Melt water channel

(c) Slightly crevassed

(d) Heavily crevassed

Figure 3.16: DEM extracts of Nordenskiöldbreen 2019 (50 m x 50 m) to investigate the aerodynamic roughness length of specific surface features. This features are debris-covered ice (a), melt water channels (b), slightly crevassed (c) and heavily crevassed (d) areas. A hillshade layer was laid under the DEMs for a better visualization of the surface features.

3.3 Surface Energy Balance Model

In order to visualize the impact of a varying aerodynamic roughness length on surface ice melt the z_0 values were implemented into the surface energy balance model of Brock and Arnold (2000). Figure 3.17 shows the resulting daily surface ice melt (blue dots) under weather conditions that can be found on an average July day on Nordenskiöldbreen for several input aerodynamic roughness lengths. Increasing z_0 values lead to a larger melt of the glacier ice varying in this example from 24.2 mm w.e. per day for a z_0 = 0.1 mm up to 43.2 mm per day (z_0 = 1 m). For comparison, a typical literature aerodynamic roughness length z_0 = 0.8 mm was also implemented into the model. The value was estimated by Smith et al. (2016b) in their study for a rather smooth glacier and reveals a daily ice melt of 25.4 mm. However, the mean z_0 value for a common down-glacier wind direction estimated for Nordenskiöldbreen in 2019 estimated with the Smith model (z_0 = 0.13 m) leads to a melt of 29.7 mm. This is an increase in daily ice melt of 17 % only due to larger surface roughness.

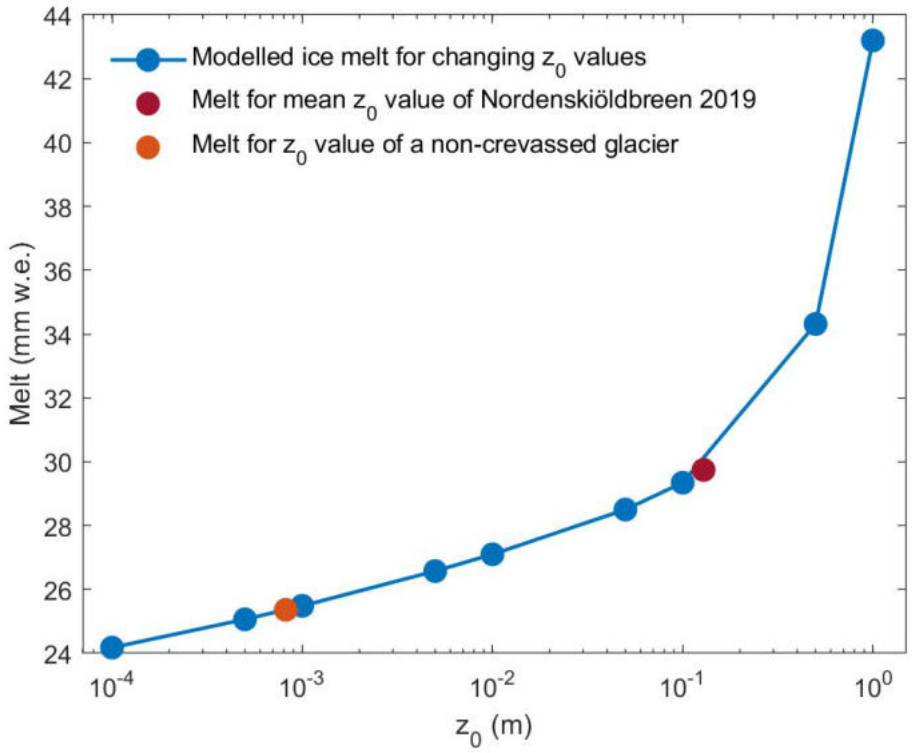

Figure 3.17: Daily surface ice melt (blue) according to different input z_0 values modelled with a simple surface energy balance model (Brock and Arnold, 2000) for weather conditions which can be found in July at Nordenskiöldbreen. Additionally, the model was fed with the mean z_0 value of Nordenskiöldbreen 2019 (red) and a literature z_0 value of a glacier with a non-crevassed (orange) surface roughness (Smith et al., 2016b) leading to the corresponding daily ice melt.

Locally, where the z_0 values exceed the length of 0.5 m, their impact on the ice melt starts to increase substantially. Accordingly, a very rough glacier with an aerodynamic roughness length of 1 m would have an ice melt that is almost twice as large as the melt on a smooth glacier with z_0 = 0.1 mm. In other words, especially the larger roughness elements (i.e. heavily crevassed areas) have the potential to substantially increase the surface ice melt indicating the importance of considering their surface roughness when estimating the ice melt of a glacier.

Chapter 4

Discussion

The results obtained in this study are in line with the aims of the thesis stated in Chapter 1. First of all, the applied approach showed that it is possible to use UAVs to build DEMs of the tidewater glacier's terminus areas. This DEM information was then used by five different models (split in transect and raster method) to estimate the aerodynamic roughness length of the mapped area. Further, the estimated z_0 values can be used to better represent the heat exchange rates and with it the actual ice melt rate of glaciers calculated in surface energy balance models. Accordingly, the results are able to answer the three stated research questions. However, before concluding with bare numbers, the data deserves a more detailed discussion.

4.1 Digital Elevation Models

The input data to build the DEMs in this thesis were aerial pictures captured with drones rather than airborne/terrestrial LiDAR approaches (e.g. Nicholson et al., 2016) or ground-based pictures (e.g. Miles et al., 2017). The received DEM resolution from our approach (about 0.25 m) was accurate enough to visualize the large crevasse obstacles. Given the advantages of a drone compared to other devices (e.g. cheap price, applicable in inaccessible areas), this thesis proofs that drones provide a reliable and effective way of data gathering used for aerodynamic roughness length estimation on heavily crevassed tidewater glaciers.

Although the SfM-MVS approach managed to build trustworthy DEM results, the obtained depth of the crevasses must be seen as a minimum depth. In other words, the crevasses might advance further down into the glacier than actually measured. This can have several reasons. The surface that was mapped during the spring field campaign could still have had some snow-bridges in the crevasses preventing the camera to capture the whole crevasse depth. Moreover, Agisoft Metashape might not be able to construct the whole crevasse depth due to the lack of reflected light from the deep crevasses. Thus, the narrowest part of the crevasse is most likely not constructed by the software. Additionally, at a depth where the crevasses get narrow down to a width of some decimeters the obtained resolution of the DEM is too coarse to map the crevasse even though it probably is continuing vertically for some meters (Ryan et al., 2015). However, in an aerodynamic context those narrow crevasses might not have a large influence.

The main shortcoming of the DEM construction is that no GCP points could be used for georeferencing. In general, properly georeferenced UAV point cloud models manage to keep up with the accuracy of laser scanning photogrammetry (Federman et al., 2017). However, for this thesis the

usage of GCPs was practically not feasible. This led to a small deformation of the DEMs what can influence the z_0 estimations. On the one hand, the observed deviation can be explained to some part by a systematic offset. According to James and Robson (2014), systematic errors are a result of self-calibration that often occurs when only using nadir image datasets. The authors further state that systematic errors could have been significantly reduced by capturing oblique images. Since for this thesis only pictures in nadir mode were collected (to save battery and capture a larger area), for further research a combination of nadir and oblique images should be considered to improve the DEM accuracy. On the other hand, the deformation of the DEM can also to some extend be explained by distortion. As seen in Figure 3.2 the deviation between the satellite image and the drone-based DEM can in particular be detected towards the sides of the glacier. This is a typical feature appearing with only nadir viewing directions used, because the reconstruction software is not able to derive the accurate radial lens distortion. Thus, it leads to a systematic 'doming' DEM deformation (James and Robson, 2014). The same effect already got detected in the precision maps of the study of James et al. (2017) on an example of weak georeferencing.

One apparent issue of building DEMs without using GCPs or other georeferencing tools (i.e. GNSS-supported aerial triangulation) is that in particular the z-axis was often substantially shifted. Again, the offset is to a large part only systematic (see Figure 3.3). This may be explained by the drone that assumes to take off at sea level height (what was not the case for Fridtjovbreen with the largest vertical offset) and calculates the altitude from that reference point. The use of artificial control points, which were set on the sea ice or water level, mostly removed that problem (see Figure 3.3 and also Ryan et al. (2015)). However, the stated investigation is no proof that there is no distortion when not using artificial control points or especially GCPs. It only indicates that systematic errors compensate for large parts of unreasonable locating.

As stated above, it needs to be pointed out that the DEMs come along with a specific uncertainty. Additionally, it is hard to even express the extent of uncertainty (i.e. the distortion) in numbers without any reference points available. While for the horizontal accuracy assessment the DEMs were compared with satellite images, a similar approach was not possible for assessing the vertical accuracy. The main challenge there is that no fix reference point could be found. For further research it might be a possibility to additionally use terrestrial laser scanning to determine the height of glacier front, which can be used to determine the vertical distortion. Alternatively, a drone equipped with RTK technology could also largely decrease the stated uncertainty.

In any case, since we are most of all interested in the relative object distances (i.e. size and spacing of roughness elements) rather than their accurate localization, the present approach is sufficient for the objectives of this thesis. Moreover, as the DEMs were detrended before implementing the z_0 model calculations (Smith et al., 2016b), all systematic offsets were negligible. Furthermore, the resulting z_0 values are not that sensible to small distortions (see Table 3.3). A distortion of for instance 5 % leads to a change in z_0 of 10 %. This means that even a distortion of several meters over the mapped area would still stay within a trustful range of z_0 estimations. Due to all those reasons, the z_0 variability resulting from the distortion uncertainty of the DEMs is minor compared to other parameters influencing the z_0 estimations such as wind direction, model calculation or scale dependency. In other words, despite the mentioned shortcomings, the DEMs are still a reliable data source to estimate the aerodynamic roughness length.

4.2 Aerodynamic Roughness Length

The z_0 estimations on crevassed terminus areas of tidewater glaciers differ depending on wind direction, model calculation and subarea grid size as well as roughness element size and mapping time. However, it is hard to determine which parameter has the largest impact on the $z - 0$ estimations. Especially the range of z_0 values by varying wind direction, grid scale and model calculation is about one order of magnitude for each parameter. Since variability due to subarea grid size and model calculation refer to method and model uncertainties they should be further narrowed down in future investigations. However, the spatial and temporal variability and the dependence on wind direction present a real range of z_0 values actually found across a tidewater glacier. Therefore, this variability should be included into surface energy balance models as accurate as possible. For a final conclusion about the relative impact of each discussed parameter, a comparison with meteorological data (e.g. anemometer) is inevitable.

4.2.1 Variability of Aerodynamic Roughness Length across the Glacier

Literature values of z_0 for such heavily crevassed glacier areas as investigated in this thesis have not been estimated before what makes it difficult to compare the results. Table 1.1 gives an overview of studies that investigated z_0 values of large crevasses. Despite the large spread of z_0 values across the models, the mean results from Table 3.4 which are averaged in all wind directions roughly agree with z_0 values found in the literature. Especially, the values from the raster method fall mostly within the same order of magnitude as proposed for instance by Smeets et al. (1999). However, the estimated z_0 values of this thesis are in general higher or at the upper limit of the listed literature values in Table 3.4. Only the range given by Fitzpatrick et al. (2019) fits for most of the models and glaciers. While comparing the z_0 estimates with literature values the size of the effectively measured roughness elements must be taken into account. Thus, obstacles declared as 'deep' or 'large' crevasses still can present a huge range of obstacle shapes and sizes. None of the stated studies in Table 1.1 investigated a crevassed area with such large roughness elements as done in this study. Therefore, somewhat higher z_0 estimations must be expected in this thesis.

Wind Direction Dependency

The wind direction has a large impact on the magnitude of the z_0 values on crevassed glaciers due to the mostly orderly arrangement of the roughness elements. Smith et al. (2016b) state, that in particular crevasses are prone to anisotropy. Our results confirmed this statements since the larger roughness elements present a stronger wind dependency. The importance of wind direction can be observed in many studies (e.g. Fitzpatrick et al., 2019; Munro, 1989; Smith et al., 2016b) and is found to be the strongest on ablation zones where elongated features like meltwater channels and crevasses are frequent. Thus, wind directions that face these features perpendicularly lead to higher z_0 values due to an increased form drag (Fitzpatrick et al., 2019).

The broad-scale topography (i.e. glacier shape and surrounding landscape) has an important impact on the aerodynamic roughness length (Quincey et al., 2017). According to the study of Fitzpatrick et al. (2019) winds are very likely (93 % of the time) to blow in direction of the mean slope angle (within 45°). Also Karner et al. (2013) observed mainly down-slope wind direction in their study on Kongsvegen glacier in northwest Spitzbergen. The reason is a topographically influenced synoptic wind system and katabatically forced down-slope winds. These can often

be observed in glacial boundary layers and are in particular common over the glacier terminus (Munro, 1989). In other words, winds on tidewater glaciers are often blowing down the glacier what makes this wind direction more interesting than the others (especially compared to cross-glacier wind systems). Therefore, the effect of roughness anisotropy on the variation of z_0 values and hence on turbulent heat exchange might be overestimated because not all four wind directions have the same likelihood to occur (Fitzpatrick et al., 2019).

Temporal Variability on Nordenskiöldbreen

The aerodynamic roughness length is not constant in time as several studies already investigated (e.g. Fitzpatrick et al., 2019; Smeets et al., 1999). The temporal study conducted on Nordenskiöldbreen presented a small difference in obtained z_0 values, whereas the mean z_0 value decreased with time. The observations are in line with other studies (i.e. Fitzpatrick et al., 2019), which also did not observe a large difference in z_0 estimates for the same location measured in two consecutive years. The area and resolution of Nordenskiöldbreen investigated in this case study are the same since the larger area of the Nordenskiöldbreen 2019 DEM was clipped and resampled to the extent and resolution of the Nordenskiöldbreen 2020 DEM. Small changes in the input area due to a changing glacier front line are expected to have a minor impact on the results, because the roughness elements on the two DEMs are very similar. Therefore, a slightly larger input area is not affecting an average z_0 value.

It is hard to find the real reason for the decrease in z_0 estimation, especially since the deviations in z_0 values are small (mostly below 10 %). Nevertheless, the differences might be explained due to a lower glacier front height (see Figure 3.12). The ice thickness at the glacier front of Nordenskiöldbreen is about 5 m to 30 m lower in 2020 compared to one year earlier, if no vertical referencing errors of the DEMs are assumed. Nordenskiöldbreen is a tidewater glacier that is about to loose its contact to the sea water and thus the surface ice melt is an increasingly important contributor to ice loss (Błaszczyk et al., 2009). This melt could have led to a change of the roughness element height what then impacts the aerodynamic roughness length. However, an investigation of average roughness element sizes produced exactly the same mean height values (16 m for up- and down-glacier and 9 m for cross-glacier wind directions) for the clipped area of Nordenskiöldbreen 2019 as for the same area one year later (see Table 3.2). Thus, despite the large ice melt, the roughness elements managed to roughly keep the same size and therefore are not having a strong impact on the resulting z_0 values.

A further reason to explain the temporal variability in z_0 values could be that the data for the DEM 2020 was collected one month earlier. Thus, there might still were some snow bridges remaining in the crevasses what lowered the resulting aerodynamic roughness length. The two stated reasons are most likely able to explain the differences in mean z_0 values since the decrease in z_0 is small. In any case, only the temporal variability in z_0 from one year to the next was investigated in this thesis. Alternatively, the intra-annual variability could be of interest and most likely leads to larger deviations, especially when considering snow cover. Quincey et al. (2017) found out that the impact of a snow event could reduce the aerodynamic roughness length by about 75 %. However, the impact might decrease with increasing roughness elements. Thus, such an approach should be investigated in future research.

Figure 4.1: Drone picture of Tunabreen (left) and Fridtjovbreen (right) taken during fieldwork. The crevasses on Tunabreen are chaotically aligned and steep whereas on Fridtjovbreen they are aligned more regularly and less steep. Photos taken by Richard Hann.

Glacier Variability

In general, Tunabreen and Nordenskiöldbreen (especially the part mapped in 2020) show higher z_0 values than Fridtjovbreen and Heuglinbreen. This is in good agreement with the average length and height of roughness elements estimated for each glacier in Table 3.2. The crevasses on Tunabreen and Nordenskiöldbreen are generally deeper and steeper than the crevasses on the other two glaciers (see DEMs in Appendix B). This might be explained by different dynamical behaviour, leading to higher z_0 values. Crevasses and ice flow velocity are closely linked. In general, it is assumed that the faster a glaciers flows, the more crevasses are observed in the terminus area of the glacier and the larger the area of crevassing (Błaszczyk et al., 2009). Out of all the visited glaciers, Tunabreen is the most dynamically active. Tunabreen and Nordenskiöldbreen both have flow velocities of about 0.3 m/day (averaged over the year 2019) in the upper parts of the glacier (Luckman, 2020). Additionally, Tunabreen was surging in the years 2003 to 2005 and had another advance of the glacier front about ten years later (Ericson et al., 2019). According to Mansell et al. (2012), such surging events usually lead to very chaotically aligned crevasses.

Figure 4.1 confirms the same effect comparing drone pictures from Fridtjovbreen (right) and Tunabreen (left) taken during fieldwork. Corresponding pictures of Heuglinbreen and Nordenskiöldbreen can be found on Figure C.14 in Appendix C. The front area of Tunabreen is chaotically crevassed and covered with many steep roughness elements. Crevasses on Fridtjovbreen are more regularly aligned and less steep leading to triangular-shaped roughness elements. The pictures support the observation that the anisotropy ratio value Ω is lowest on Tunabreen, as perfectly aligned roughness elements increase the anisotropy effect. Further, it is in line with the fact that the aerodynamic roughness length on Tunabreen is higher than on Fridtjovbreen. However, comparing average z_0 values among different glaciers is challenging because the mean z_0 values depend a lot on the mapped input area and therefore the size of included roughness elements. This also explains the following occurrence: The mean z_0 values of Nordenskiöldbreen 2020 are larger than those of Nordenskiöldbreen 2019 (see Figure 3.4). However, as soon as the Nordenskiöldbreen 2019 data is clipped to the same extend as in 2020 its z_0 values are very similar and in this case even slightly larger than those in 2020 (see Figure 3.13). This is because many subareas with small roughness elements in 2019 were excluded in the clipped version used

for the investigation of the temporal z_0 variability. Therefore, the differences in z_0 between the glaciers, as for instance shown in Figure 3.4, should not be over interpreted since z_0 estimation are more similar in between the glacier if the same roughness elements sizes are compared (see subarea values on Figure 3.6).

The occurrence of heavily crevassed areas on a glacier can have a large influence on its mean z_0 value. If we consider tidewater glaciers like Fridtjovbreen or Heuglinbreen, which are only heavily crevassed on their terminus area (see Figure 2.1), this small area is still substantially impacting the resulting mean z_0 values. To make an example, a fictitious glacier has a heavily crevassed area of about 10 % of its complete surface with a z_0 value of 0.2 m. The other 90 % are mostly smooth with a z_0 value of 0.001 m. Thus, the mean z_0 value of the glacier is still about 0.02 m. In summary, even small areas on a glacier which are heavily crevassed can have a large influence on the total surface ice melt and surface energy balance of this given glacier. However, this influence is larger for glaciers like Nordenskiöldbreen or Tunabreen which are heavily crevassed on most parts of the glacier area and in particular for surging glaciers which are often chaotically crevassed.

4.2.2 Evaluation of Model Calculations

The obtained z_0 estimations manage to point out the two used calculation approaches, as models of the raster method have similar values which are in general (locally up to one order of magnitude) lower than those calculated with the transect method. The correlation values of Table 3.5 indicate how similar the estimated z_0 values are in a relative perspective among the different models. However, it does not give any conclusion about the quality of the individual models. To find out which model performs the best and for a better evaluation of the estimated z_0 values, a comparison with alternative measurement methods (e.g. wind profiles) would be necessary. These need to be measured at the same time and location as the DEM input data surveying, as done in several studies (Fitzpatrick et al., 2019; Quincey et al., 2017; Smeets et al., 1999). For this thesis however, the area of interest was inaccessible for such measurements what means that this validation option was impossible to achieve.

Assessment of Model Results

There are several studies investigating the aerodynamic roughness length with both a transect and a raster method (Chambers et al., 2020; Quincey et al., 2017; Smith et al., 2016b, 2020). However, no other study calculated z_0 with the same approach on such heavily crevassed glaciers. This makes it challenging to evaluate the model estimates and therefore a proper assessment of the results is hard to achieve. Further, the model results in this thesis could not have been verified with the data and method of the study on which our models are originally based on (e.g. Smith model with study of Smith et al. (2016b)), since neither codes nor DEM input data of these studies were available. This could have improved the confidence in the obtained model results and could be interesting for future investigations. Nevertheless, the study results can still be compared relatively. In the study of Smith et al. (2016b), the differences between the algorithms were in general small, since the results from the raster method were about 20 % lower compared to the transect method. However, this study was only looking at smaller plots (2 m x 2 m). Additionally, as soon as the authors were looking at deep crevasses, the transect method could lead to z_0 values twice as large as those calculated with the raster method. A similar relationship between the two methods has been determined in the study of Chambers et al. (2020) and on

some spots in the study of Quincey et al. (2017). The authors of the last-mentioned study found only small z_0 differences among the two methods for small plot sizes, but more random results for larger plots (e.g. 15 m x 15 m). On locations with crevassed glacier ice, Smith et al. (2020) received z_0 values which were about 35% smaller calculated with the raster method compared to the transect method, whereas the difference increased for increasing roughness elements. In summary, the results found in other studies show similar characteristics as those investigated in this thesis.

The spatial variability of aerodynamic roughness length values on glaciers can be large as various studies already investigated (e.g. Smith et al., 2016b). The obtained results on all mapped tidewater glaciers confirmed this statement. In general, the size of subarea z_0 variability parameters (i.e. Std or IQR) across a glacier is about the same size as the mean z_0 value itself (see Figure 3.4). This again indicates a large topographic variability on a glacier surface. Moreover, it reveals an important sampling issue (Smith et al., 2016b) as in general the standard deviation and IQR increase with increasing mean z_0 values. However, the basic approach followed in this thesis allows accounting for local variabilities instead of just using one single value per glacier. All models manage to produce high relative z_0 values in areas of large crevasses and low relative z_0 values for non-crevassed areas. Therefore, and same as Miles et al. (2017) concluded in their study, each model manages to provide an approximation of roughness in relative scales. Nevertheless, the range of model results also indicates some uncertainties about the magnitude of the aerodynamic roughness length.

Since little reference values for z_0 on heavily crevassed roughness elements can be found in the literature, the models were run over specific surface features on Nordenskiöldbreen for comparison (see Figure 3.15). The resulting z_0 values correspond well with the existing values from other studies. Debris-covered ice from a medium moraine with a estimated aerodynamic roughness length of several milimeters (calculated with the raster method) is a bit lower than those found by Quincey et al. (2017) of 5 mm to 25 mm or by Brock et al. (2010) with 16 mm. Only the transect methods estimated z_0 values within a similar range. However, small crevasses estimated with the raster method, reach the same magnitude as z_0 values (9 mm to 18 mm) measured by Smith et al. (2016b). For clean ice, z_0 values below 0.5 mm were estimated in this thesis. A literature study by Brock et al. (2006) shows that z_0 values for glacier ice often are between 0.1 mm and 2 mm. Therefore, the estimated values are within the (lower) range of z_0 values found in the literature. Further, Smith et al. (2016b) found z_0 values of 2 mm to 4 mm for supraglacial channels what corresponds well with our estimated values for the meltwater channels (2 mm to 8 mm for the raster method). In summary, the estimated z_0 values for small scale surface features correspond with existing literature values indicating that the used model approach is applicable for heavily crevassed tidewater glaciers. In general, the z_0 values of the surface features show that the raster method performed slightly better than the transect method as its results were closer to literature values.

Sheltering Effect of Roughness Elements

The transect method on the one hand does not account for sheltering of an obstacle (Smith et al., 2016b), what is a main shortcoming of this approach. The raster method on the other hand neglects the frontal areas below the detrended plane assuming that it would be effectively sheltered. According to Nicholson et al. (2016), z_0 values are expected to be lower if the sheltering effect is considered. The model results in this thesis confirm this statement as the transect methods consistently produced higher z_0 values than the raster method. To consider the sheltering effect,

the so called displacement height z_d is often applied. A large density of roughness elements leads to an upwards displacement of the zero wind velocity level. The length of this vertical displacement is called z_d (Nicholson et al., 2016). It is a corrective height displacement (Lettau, 1969) occurring over taller roughness elements where the level of momentum transfer between obstacles and airflow is displaced vertically (Nicholson et al., 2016). As a general approximation, z_d is often defined as 0.7 h^* (Grimmond and Oke, 1999). For the raster method, the displacement height z_d corresponds to the detrended plane level that was introduced earlier. Therefore, the effective roughness only depends on the roughness elements above this displacement height which indicates how far the effective turbulent mixing advances into the crevasses (Nicholson et al., 2016). Again, the transect method is not considering any displacement height.

Furthermore, the sheltering issue can be discussed from another perspective. If the roughness elements on a plot are too densely packed, then the objects begin to interfere aerodynamically with each other (Rounce et al., 2015). They form a plateau-like new surface at their tops (Lettau, 1969) leading to a skimming flow. If this roughness density (frontal area divided by ground area) increases as far that skimming flow is happening then the z_0 values are decreasing again (Grimmond and Oke, 1999). Accordingly, the results from the transect methods which are not considering any sheltering effects are likely to overestimate the roughness, especially for densely packed obstacles (Nicholson et al., 2016). Several studies (e.g. Nicholson et al., 2016; Rounce et al., 2015; Smith et al., 2016b) used a roughness density threshold of 20 % to 30 % (as stated by Macdonald et al. (1998)) for Equation 2.8 of Lettau (1969) to still be valid. In our thesis, all glaciers were tested with the Smith method for their roughness density. Some glaciers (e.g. Fridtjovbreen) are completely within the range for which Equation 2.8 holds. Other glaciers (e.g. Tunabreen) present some subareas with a higher roughness density (locally up to 0.5) which indicates some skimming flow over the obstacles. Among all glaciers, the subareas with a roughness density above the threshold of 30 % can be found predominantly in areas close to the glacier front, which are heavily crevassed. Similar observations were already investigated by Smith et al. (2016b). However, the large majority of the subareas are below the threshold and only some exceed it. This is represented by the mean roughness density values of the glaciers, which are between 0.1 and 0.16 for each glacier (e.g. 0.15 for Tunabreen). Therefore, this thesis shows that the Lettau (1969) Equation 2.8 can be assumed to hold also on heavily crevassed tidewater glaciers.

Definition of Obstacle Height

Another important difference between the model methods is the definition of the obstacle height h^*. Rounce et al. (2015) state that the lack of a clear obstacle definition presents the main problem of the bulk method approach introduced by Lettau (1969). Especially in crevassed glacier areas, where an apparent base level is missing, it is hard to define individual roughness elements and their according height (Nicholson et al., 2016; Smith et al., 2016b). Moreover, Nield et al. (2013b) state that the obstacle height is the most important control parameter over the output of z_0 what means that an appropriate definition of h^* is crucial. In this thesis, the Smith and Chambers models, as well as Munro and Lettau models, only differ in the definition of h^*. While the parametrization of h^* with twice the standard deviation produced higher z_0 values in the raster method (Chambers), the results of this approach are lower in the transect method (Munro).

Again, it is hard to tell which model and which definition of h^* might performs better as there is no reference data to compare it with. Both definitions have their merits and weaknesses. Smith

et al. (2016b) on the one hand question the rationale behind the standard deviation approach. The authors state that any chosen obstacle height will be somewhat arbitrary. Moreover, they suggest that their obstacle height (i.e. mean height above detrended plane) could be most meaningful on ice surfaces that are mainly irregular. Chambers et al. (2020) on the other hand chose the standard deviation definition to preserve the influence of the larger roughness elements. However, it clearly can be seen that the definition of h^* has a lower impact on the results than the basic approach (i.e. raster/transect) itself. This is because the differences in z_0 results between the two methods are far larger than the according differences between the same method but varying definition of h^*.

In summary, the transect method is assuming isotropy, equal size and distribution of roughness elements and not considering sheltering. None of those assumptions is effectively valid on heavily crevassed tidewater glaciers. Additionally, the transect method assumes tower-like roughness elements whereas in reality crevasses are getting more narrow with depth. The raster method is not making any of those assumptions and is even considering the displacement height z_d. Furthermore, the raster method is making the best use out of the available dataset as every pixel value is considered for calculation (Smith et al., 2020). Despite the lack of any appropriate reference measurements (e.g. anemometer) what aggravates a clear conclusion on best model performance, it can be stated that raster methods should - at least theoretically - be more accurate.

4.2.3 Scale Dependency of Aerodynamic Roughness Length

The grid size study made on the DEM of Fridtjovbreen with different subarea sizes showed clearly that there is a scale dependency issue for the calculation of the aerodynamic roughness length. This issue appears independent of the chosen glacier, model or wind direction. In theory, the estimated z_0 values should be independent of the input grid size as long as homogeneous object spacing and shape can be assumed (Lettau, 1969). However, many studies investigated and encountered the dependency of z_0 estimations on the size of the subarea or the transect length (e.g. Fitzpatrick et al., 2019; Miles et al., 2017; Rees and Arnold, 2006). They all agree on the relationship: larger subareas or longer transects cause z_0 values to increase (Chambers et al., 2020). Also the grid size study conducted on Fridtjovbreen revealed that the z_0 values increase with increasing grid size. This can be explained with the fact that glaciers (especially crevassed terminus areas as mapped in this thesis) often have heterogeneous roughness elements (Quincey et al., 2017). In general, it needs to be considered that the selection of an appropriate grid size comes along with a large uncertainty. Thus, the question appeared which grid size would produce the most meaningful results.

Chambers et al. (2020) state that the comparison with independent methods like aerodynamic wind profiles is the best way to answer this question. Quincey et al. (2017) did exactly that and concluded that small patch sizes usually underestimated the z_0 values while large patch sizes in general overestimated them. As they were focusing on debris-covered glacier roughness they chose patch sizes of 5 m up to 15 m. Thus, their patch sizes were larger than their mean roughness element. In any case, the option to use meteorological data (e.g. met mast) was not possible in this thesis. Therefore, the decision needed to be made otherwise. The grid size in our models is directly (Smith and Chambers model) or indirectly (Munro, Lettau and Fitzpatrick model) correlated to the ground area S. According to Lettau (1969), S is defined as the total area of a site divided by the number of obstacles. Thus, the stated relation can be fulfilled if the grid size is chosen in a way that it represents the size of one individual roughness element. Therefore, in

this thesis the grid size was defined such that it is large enough to include an average obstacle size and small enough to provide a considerable spatial resolution of z_0 values across the glacier. As far as the results could be evaluated, the selected grid size of 50 m x 50 m led to meaningful z_0 estimations.

The validity of the chosen grid size can further be evaluated theoretically. According to the theory of Smith (2014), the definition of 'roughness' is related to the grid scale that separates roughness from topography. In other words, the author distinguishes between the grain roughness that represents the texture of a roughness element and the form roughness which corresponds to the form drag of the roughness element itself. The grid size, at which the transition from roughness to topography (grain to form roughness, respectively) occurs, provides a useful reference point (Smith, 2014). This transition between different scales of roughness can be found on a kink in the trend line of a figure plotting z_0 values against increasing grid sizes (Shepard et al., 2001; Smith, 2014). Figure 4.2 illustrates this breakpoint on the example of the Smith and Munro model for the down-glacier wind direction on Fridtjovbreen. The breakpoint is located somewhere between a subarea grid size of 30 m and 50 m.

To make sure not having a too small grid size, a grid size of 50 m was chosen. If the grid size would be smaller than 50 m, then it only would consider the microtopography of a roughness element itself rather than the effect of the large-scale surface features. Thus, the small grids might not include an obstacle population that is large enough to represent the glacier surface (Miles et al., 2017). This effect has already been discussed in Section 2.4 for detrending grid sizes. Furthermore, Smith (2014) state in his theory, that the scale of specific features that are already distinguished, determines an appropriate grid scale. In our case, this corresponds to the mean roughness elements described in Table 3.2, which again have the size of about 30 m to 50 m. Due to all those reasons, a grid size of 50 m seems to be the most appropriate one for the tidewater glaciers investigated in this thesis, despite the lack of a clear reference measurements to properly assess the results.

4.3 Surface Energy Balance Model

Karner et al. (2013) found out that the sensible heat flux was the most important energy source at the surface of Kongsvegen, a glacier with similar size and topographic conditions as those investigated in this study. Another important energy source was the latent heat flux. Both heat fluxes were almost entirely contributed to ice melt rather than heating of the ice. Another study of Fausto et al. (2016) states that on average the non-radiative energy fluxes on their study site in Greenland contributed up to 76 % of the daily ice melt energy. Both studies show that turbulent fluxes are an important contributor to the ice melt and therefore essential to include into surface energy balance models (Steiner et al., 2018). To do so, the terms for the turbulent fluxes (sensible and latent heat flux) must be derived. This is commonly achieved by the aerodynamic bulk method using the aerodynamic roughness length to calculate these turbulent fluxes, whereof z_0 is the most important input parameter (Chambers et al., 2020).

Various studies (e.g. Fausto et al., 2016) investigated the large influence of increased z_0 values on surface ice melt. Brock et al. (2000) found out that an increase of z_0 by one order of magnitude will more than double the value of turbulent fluxes. The same effect was investigated in this thesis with a simple energy balance model to calculate surface ice melt. Although the effect was not that large as in the study of Brock et al. (2000), the impact of an increasing z_0 value is substantial. The larger the z_0 values, the larger the calculated surface ice melt. The results

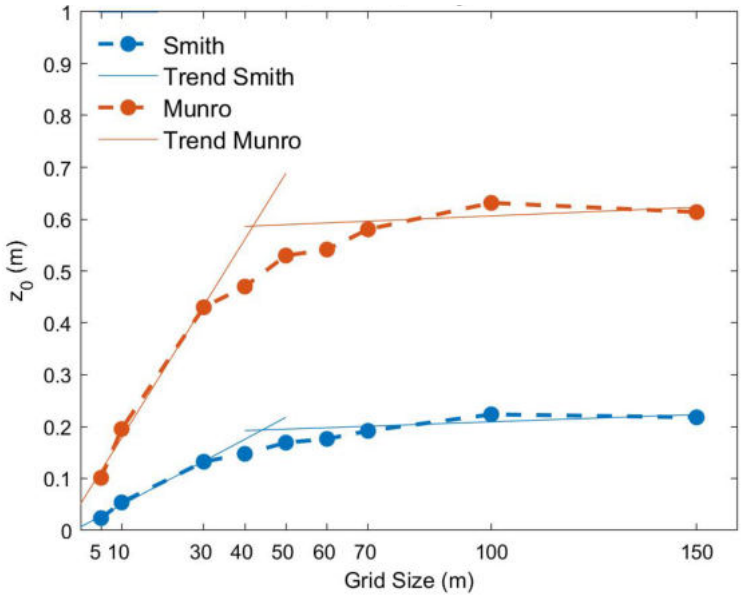

Figure 4.2: Scale dependency of mean z_0 values of the Smith and Munro model for the down-glacier wind direction on Fridtjovbreen with chosen subarea grid sizes from 5 m to 150 m. The solid line marks the trend line of the lower and upper three data points, respectively. The grid size at the intersection of the two trend lines marks the breakpoint indicating a meaningful subarea grid size.

showed, that the surface ice melt for a glacier with a roughness like Nordenskiöldbreen is almost 20 % larger compared to the roughness of a smooth glacier. Locally, where the z_0 values are above average, the surface ice melt can increase substantially. However, it needs to be considered that the reference z_0 value of the smooth glacier is averaged over the whole glacier, whereas our z_0 values only refer to the mapped extract of each glacier. This is especially important for the tidewater glaciers Fridtjovbreen and Heuglinbreen where only the area close to the glacier front is crevassed. Furthermore, the surface energy balance model used in this thesis is very basic and based on the bulk method. The two Equations 2.11 and 2.12 are used for the calculation of the turbulent heat fluxes, which of course are model approximation and therefore come along with some uncertainties.

A major advantage of the method used in this thesis is that not only one z_0 value but various across the mapped glacier area were determined. Thus, they all could be implemented into the surface energy balance model leading to a more accurate representation of the surface ice melt. This is especially crucial for surfaces with heterogeneous roughness elements like heavily crevassed glacier surfaces where a single z_0 value for the whole glacier is a poor representation of the actual processes (Miles et al., 2017). Given that the climate gets wetter, warmer and windier under climate change, turbulent fluxes have an increasing contribution to surface energy balance models (Smith et al., 2020). Furthermore, heat flux variations can be large, already within a small spatial scale due to topographic effects (Sauter and Galos, 2016). Accordingly, an appropriate estimation of spatial variations in z_0 values is important to decrease model errors for the calculation of surface ice melt (Miles et al., 2017).

Chapter 5

Conclusion and Outlook

5.1 Conclusion

The heavily crevassed terminus areas of the tidewater glaciers Fridtjovbreen, Heuglinbreen, Nordenskiöldbreen and Tunabreen were mapped with drones to build DEMs using a SfM-MVS photogrammetry approach with Agisoft Metashape. UAVs for data surveying proved to be a successful and cheap tool to map inaccessible and heavily crevassed glacier areas while still providing a DEM resolution good enough to reveal crevasse shape informations like spacing width and depth. To take into account the spatial variability across the glacier, the DEM was divided into subareas of 50 m x 50 m. Five different models were successfully applied to each DEM subarea to calculate the aerodynamic roughness length and therefore achieved the aim of the first research question. The five models can be divided into two groups: the transect method and the raster method. While the transect method is simply counting the number of roughness elements for each transect, the raster method is using each DEM cell's elevation value to calculate the aerodynamic roughness length. The z_0 estimations from the transect method are in general higher (up to one order of magnitude) than the raster method estimations. It is hard to evaluate which model performs the best, since reference data (e.g. wind profiles) is not available. However, in contrast to the transect method, the raster method accounts for some sheltering effects and does not assume homogeneity among the roughness elements. This makes the raster method theoretically more trustful than the transect method.

Wind direction and grid size of the subarea have a large impact on the z_0 estimations, again producing a range of up to one order of magnitude for each parameter. The roughness elements investigated in this thesis are strongly anisotropic. For winds blowing parallel to the ice flow direction the z_0 values are larger than for winds crossing the glacier perpendicularly. The chosen grid size of the subareas, each producing one z_0 value and thus influencing the spatial resolution of the investigated area, presents a large uncertainty in aerodynamic roughness length estimation. The resulting z_0 values are strongly scale dependent, whereas a larger grid size leads to higher z_0 values. A conducted grid sizes case study led to the selected subarea grid size of 50 m x 50 m, which was assumed to be large enough to include an average roughness element while still being small enough to account for the roughness variability across the glacier. If all parameters are included, the range of the resulting z_0 estimations is large, with locally up to three (in extreme cases even four) orders of magnitudes. Nevertheless, the model estimates of z_0 strongly correlate to each other. In other words, all models managed to detect the same relative spatial variability across the glacier. In absolute values and to come back to the second research question, the

estimated z_0 values range from below one milimeter (snow-covered, smooth glacier surface) up to several decimeters (heavily crevassed ice) or locally even more. Averaged z_0 values for down-glacier wind directions vary from 0.08 m up to 0.88 m depending on glacier and model.

The chosen approach allows providing several instead of just one average z_0 value for each mapped glacier area. This is crucial especially for such heavily crevassed glaciers as investigated in this thesis, where one value would be a poor representation of the real roughness on such a complex topography. The z_0 values of the investigated tidewater glacier are substantially larger than average values of smooth glaciers often found in literature and used for surface energy balance models. Therefore, such models can now incorporate these distributed z_0 estimations leading to a better representation of turbulent heat fluxes and prediction of surface ice melt rates. In this thesis, a simple energy balance model was used to answer the third research question, by showing that larger z_0 values found on heavily crevassed tidewater glaciers significantly increased the surface ice melt of a glaciers. The calculated melt is almost 20 % larger for an average z_0 value found on crevassed tidewater glaciers compared to the z_0 value of a smooth glacier. This effect increases substantially where local z_0 estimations exceed a value of 0.5 m. In other words, heavily crevassed glacier areas have the potential to significantly increase the surface ice melt indicating the importance of considering their surface roughness when estimating the ice melt of a glacier. To conclude, despite the challenges and uncertainties of the approach used for this thesis the obtained results are promising. They show that drone-based DEMs represent a valuable and operating tool to investigate the spatial variability of the aerodynamic roughness length and its influence on turbulent fluxes and surface ice melt, especially on crevassed and inaccessible glaciers.

5.2 Outlook

As stated above, the range of estimated z_0 values is large. While one part of it can be attributed to real variability (e.g. wind direction and general spatial variability), another part is related to calculation uncertainty and simple method assumptions. The latter part provides potential to further be minimized in future work. Some degree of uncertainty in z_0 estimation comes along with the unsatisfactory georeferencing of the DEM. Inaccessible topography made it impossible to place any GCPs in the field. Thus, the most obvious georeferencing method could not be applied during fieldwork on heavily crevassed glaciers. However, other georeferencing tools like GNSS-supported aerial triangulation (Chudley et al., 2019), RTK equipped drones or the additional application of oblique imagery (Vacca et al., 2017) might improve the accuracy of the DEM and with it the resulting z_0 estimation and therefore should be considered for further investigations.

Furthermore, the scale dependency of the models is responsible for a large part of the total model uncertainty. Ideally, for future work a scale independent calculation method for z_0 could be found. Otherwise it is crucial to determine which input grid size of subarea produces the most trustful z_0 values. To do so and to additionally evaluate model performance or simply narrow down the large range of meaningful z_0 values, a comparison with meteorological measurements (e.g. wind profiles) is highly recommended for future work. Whenever possible, this needs to be measured at the same time and location as the field work is conducted. In inaccessible areas these measurement stations might have to be placed on the glacier by helicopter or the drones could be used themselves to measure such parameters. Alternatively, the models might be evaluated on a test area where reference meteorological data is available. Another possibility to assess the results is the comparison with wind tunnel models or computational fluid mechanics simulations.

Several studies investigated the impact of the DEM input resolution (e.g. Chambers et al., 2020; Miles et al., 2017) and the chosen detrending method (e.g. Chambers et al., 2020; Smith, 2014) on the resulting z_0 values. Both parameters are able to strongly influence the z_0 estimations. For further research and to best estimate the aerodynamic roughness length out of drone-based data, the impact of input resolution and detrending method should be investigated. Additionally, the widely adopted drag coefficient of Lettau (1969) corresponds to an average form drag effect on roughness elements, what not necessarily holds for heterogeneous locations (Quincey et al., 2017). Therefore, for further research it might be helpful to investigate how appropriate one single drag coefficient value is, given the large range of roughness element sizes.

UAVs provide a good opportunity to investigate inaccessible and crevassed tidewater glaciers. However, a major shortcoming is that the size of the mapped research area is limited due to signal distance and battery capacity. Drones are an appropriate tool to investigate the surface energy balance of a single glacier or at least parts of it. However, for large glaciated areas (i.e. ice sheets) this approach might not be suitable. Since these areas often are of particular interest for surface energy and mass balance models, especially regarding climate change scenarios, it could be meaningful to combine the approach with satellite data in future research. If a correlation between local, drone-based roughness estimations and global satellite data can be made, an extrapolation to large-scale estimations of spatially and temporally distributed z_0 values might be possible.

Acknowledgements

The completion of such a thesis would not be possible without the knowledge and support of various and wonderful people around me. First and foremost, I would like to thank my supervisor Dr. Richard Hann who has guided and supported me through my thesis since the very first moment. He always found time and good advice and his uncomplicated, efficient and clear supervision was much appreciated. Additionally, he was carrying out all the fieldwork with me where his large knowledge about drones in the Arctic was very valuable.

Furthermore, I want to express my thanks to the other two supervisors of this thesis, Prof. Dr. Andy Hodson from University Centre in Svalbard and Dr. Andreas Bauder from ETH Zürich. The realization of a thesis as a guest student always comes along with additional challenges and would not be possible without supervisors from both universities that believe in you and your project - especially during times of global COVID-19 pandemic. Therefore, I would like to thank Prof. Dr. Andrew Hodson for offering me this thesis at the very first place and for his large expertise about glaciology in Svalbard in general. Dr. Andreas Bauder had the thankless task to supervise a thesis that was not even initiated by himself. However, his uncomplicated and open manner and in particular the confidence he had in me made this international project possible without any problems and therefore he deserves many thanks.

I also would like to thank Dr. Evan Stewart Miles for sharing his knowledge and codes of a similar study he conducted on the Lirung Glacier in Nepal. Further, Prof. Adrian Luckman was kind enough to provide me with flow velocity data of the tidewater glaciers I investigated in this thesis which could be used for the discussion of my results.

My next acknowledgement goes out to my friend and project colleague Arthur Garreau. We not only shared the same fieldwork and project topic what led to many inspiring discussions about glacier-atmosphere interaction, but also the admiration for Svalbard and the urge to go out and explore this unique landscape in our free time. Regarding fieldwork I would like to further thank Christina Hess for her support in drone spotting, picture taking and cake baking. In addition, many thanks go out to Florina Roana Schalamon for reading through my thesis and providing valuable feedback. I also would like to mention here my friends in Svalbard as well as in Switzerland for their motivation, inspiring conversations and all the amazing moments we shared and in particular my family for all their loving support throughout my studies.

Last but by far not least I would like to express my gratitude to the financial support of the Arctic Field Grant provided by the Svalbard Science Forum (SSF) which is coordinated by the Research Council of Norway (RCN). The Arctic Field Grant funded the whole project and without it the fieldwork and large parts of the thesis could not have been conducted.

References

Agisoft LLC, 2019: Agisoft Metashape User Manual - Professional Edition, Version 1.5. Tech. rep., 145 pp.

Agisoft LLC, 2020: Agisoft Metashape. Accessed on: 2020-05-01, URL https://www.agisoft.com/.

Aicardi, I., F. Chiabrando, N. Grasso, A. M. Lingua, F. Noardo, and A. Spanò, 2016: UAV photogrammetry with oblique images: first analysis on data acquisition and processing. *ISPRS - International Archives of the Photogrammetry, Remote Sensing and Spatial Information Sciences*, Prague, Czech Republic, Vol. XLI-B1, 835–842, doi:10.5194/isprsarchives-XLI-B1-835-2016.

Arnold, N. S., and W. G. Rees, 2003: Self-similarity in glacier surface characteristics. *Journal of Glaciology*, **49 (167)**, 547–554, doi:10.3189/172756503781830368.

Arnold, N. S., W. G. Rees, A. J. Hodson, and J. Kohler, 2006: Topographic controls on the surface energy balance of a high Arctic valley glacier. *Journal of Geophysical Research*, **111 (F02011)**, 1–15, doi:10.1029/2005JF000426.

Baltsavias, E. P., E. Favey, A. Bauder, H. Bosch, and M. Pateraki, 2001: Digital surface modelling by airborne laser scanning and digital photogrammetry for glacier monitoring. *Photogrammetric Record*, **17 (98)**, 243–273, doi:10.1111/0031-868X.00182.

Bauder, A., M. Funk, and M. Huss, 2007: Ice-volume changes of selected glaciers in the Swiss Alps since the end of the 19th century. *Annals of Glaciology*, **46**, 145–149, doi:10.3189/172756407782871701.

Bhardwaj, A., L. Sam, Akanksha, F. J. Martín-Torres, and R. Kumar, 2016: UAVs as remote sensing platform in glaciology: Present applications and future prospects. *Remote Sensing of Environment*, **175**, 196–204, doi:10.1016/j.rse.2015.12.029.

Błaszczyk, M., J. A. Jania, and J. O. Hagen, 2009: Tidewater glaciers of Svalbard: Recent changes and estimates of calving fluxes. *Polish Polar Research*, **30 (2)**, 85–142.

Braithwaite, R. J., and O. B. Olesen, 1990: Response of the energy balance on the margin of the Greenland ice sheet to temperature changes. *Journal of Glaciology*, **36 (123)**, 217–221, doi:10.1017/S0022143000009461.

Brock, B. W., and N. S. Arnold, 2000: A spreadsheet-based (microsoft excel) point surface energy balance model for glacier and snow melt studies. *Earth Surface Processes and Landforms*, **25 (6)**, 649–658, doi:10.1002/1096-9837(200006)25:6<649::AID-ESP97>3.0.CO;2-U.

Brock, B. W., C. Mihalcea, M. P. Kirkbride, G. Diolaiuti, M. E. J. Cutler, and C. Smiraglia, 2010: Meteorology and surface energy fluxes in the 2005–2007 ablation seasons at the Miage debris-covered glacier, Mont Blanc Massif, Italian Alps. *Journal of Geophysical Research*, **115 (D09106)**, 1–16, doi:10.1029/2009JD013224.

Brock, B. W., I. C. Willis, and M. J. Sharp, 2006: Measurement and parameterization of aerodynamic roughness length variations at Haut Glacier d'Arolla, Switzerland. *Journal of Glaciology*, **52 (177)**, 281–297, doi:10.3189/172756506781828746.

Brock, B. W., I. C. Willis, M. J. Sharp, and N. S. Arnold, 2000: Modelling seasonal and spatial variations in the surface energy balance of Haut Glacier d'Arolla, Switzerland. *Annals of Glaciology*, **31**, 53–62, doi:10.3189/172756400781820183.

Casella, V., and M. Franzini, 2016: Modelling steep surfaces by various configurations of nadir and oblique photogrammetry. *ISPRS Annals of Photogrammetry, Remote Sensing and Spatial Information Sciences*, Prague, Czech Republic, Vol. III-1, 175–182, doi:10.5194/isprsannals-iii-1-175-2016.

Chambers, J. R., M. W. Smith, D. J. Quincey, J. L. Carrivick, A. N. Ross, and M. R. James, 2020: Glacial Aerodynamic Roughness Estimates: Uncertainty, Sensitivity, and Precision in Field Measurements. *Journal of Geophysical Research: Earth Surface*, **125 (2)**, 1–19, doi:10.1029/2019JF005167.

Chappell, A., and G. L. Heritage, 2007: Using illumination and shadow to model aerodynamic resistance and flow separation: An isotropic study. *Atmospheric Environment*, **41 (28)**, 5817–5830, doi:10.1016/j.atmosenv.2007.03.037.

Chudley, T. R., P. Christoffersen, S. H. Doyle, A. Abellan, and N. Snooke, 2019: High-accuracy UAV photogrammetry of ice sheet dynamics with no ground control. *Cryosphere*, **13 (3)**, 955–968, doi:10.5194/tc-13-955-2019.

Colgan, W., H. Rajaram, W. Abdalati, C. McCutchan, R. Mottram, M. S. Moussavi, and S. Grigsby, 2016: Glacier crevasses: Observations, models, and mass balance implications. *Reviews of Geophysics*, **54 (1)**, 119–161, doi:10.1002/2015RG000504.

Cuffey, K., and W. S. B. Paterson, 2010: *The Physics of Glaciers*. 4th ed., Academic Press, 704 pp.

DJI, 2017: Phantom 4 Pro/Pro+, User Manual v1.4. Tech. rep., 68 pp.

DJI, 2019: Mavic 2 Enterprise Series, User Manual v1.8. Tech. rep., 69 pp.

Ericson, Y., E. Falck, M. Chierici, A. Fransson, and S. Kristiansen, 2019: Marine CO2 system variability in a high arctic tidewater-glacier fjord system, Tempelfjorden, Svalbard. *Continental Shelf Research*, **181**, 1–13, doi:10.1016/j.csr.2019.04.013.

ESA, 2020: Copernicus Open Access Hub. Accessed on: 2020-04-15, URL https://scihub.copernicus.eu/.

Fausto, R. S., D. Van As, J. E. Box, W. Colgan, P. L. Langen, and R. H. Mottram, 2016: The implication of nonradiative energy fluxes dominating Greenland ice sheet exceptional ablation area surface melt in 2012. *Geophysical Research Letters*, **43 (6)**, 2649–2658, doi:10.1002/2016GL067720.

Federman, A., M. Santana Quintero, S. Kretz, J. Gregg, M. Lengies, C. Ouimet, and J. Laliberte, 2017: UAV photgrammetric workflows: A best practice guideline. *International Archives of the Photogrammetry, Remote Sensing and Spatial Information Sciences - ISPRS Archives*, Ottawa, Canada, Vol. 42, 237–244, doi:10.5194/isprs-archives-XLII-2-W5-237-2017.

Fitzpatrick, N., V. Radić, and B. Menounos, 2019: A multi-season investigation of glacier surface roughness lengths through in situ and remote observation. *The Cryosphere*, **13 (3)**, 1051–1071, doi:10.5194/tc-13-1051-2019.

Flink, A. E., R. Noormets, N. Kirchner, D. I. Benn, A. Luckman, and H. Lovell, 2015: The evolution of a submarine landform record following recent and multiple surges of Tunabreen glacier, Svalbard. *Quaternary Science Reviews*, **108**, 37–50, doi:10.1016/j.quascirev.2014.11.006.

Garreau, A., 2020: Validation and Application of Novel Wind Estimation Methods with Quadcopter UAVs in the Arctic. *Master Thesis*, 48.

Gindraux, S., R. Boesch, and D. Farinotti, 2017: Accuracy assessment of digital surface models from unmanned aerial vehicles' imagery on glaciers. *Remote Sensing*, **9 (2)**, 186, doi:10.3390/rs9020186.

Grimmond, C. S. B., and T. R. Oke, 1999: Aerodynamic Properties of Urban Areas Derived from Analysis of Surface Form. *Journal of Applied Meteorology*, **38 (9)**, 1262–1292, doi:10.1175/1520-0450(1999)038<1262:APOUAD>2.0.CO;2.

Groos, A. R., T. J. Bertschinger, C. M. Kummer, S. Erlwein, L. Munz, and A. Philipp, 2019: The Potential of Low-Cost UAVs and Open-Source Photogrammetry Software for High-Resolution Monitoring of Alpine Glaciers: A Case Study from the Kanderfirn (Swiss Alps). *Geosciences*, **9 (8)**, 356, doi:10.3390/geosciences9080356.

Hagen, J. O., O. Liestøl, E. Roland, and T. Jørgensen, 1993: *Glacier Atlas of Svalbard and Jan Mayen*. Norsk polarinstitutt, Oslo, 169 pp.

Hann, R., A. Hodson, and M. Jonassen, 2019: Glacier Mapping and Wind Estimation with UAVs on Svalbard. *Svalbard Science Conference (SSC)*, Oslo.

Hanssen-Bauer, I., and Coauthors, 2019: Climate in Svalbard 2100. *Norwegian Centre for Climate Services (NCCS)*, The Norwegian Centre for Climate Services (NCCS), 105.

Hock, R., 2005: Glacier melt: A review of processes and their modelling. *Progress in Physical Geography*, **29 (3)**, 362–391, doi:10.1191/0309133305pp453ra.

Hodson, A., and Coauthors, 2007: A glacier respires: Quantifying the distribution and respiration CO2 flux of cryoconite across an entire arctic supraglacial ecosystem. *Journal of Geophysical Research: Biogeosciences*, **112 (4)**, 1–9, doi:10.1029/2007JG000452.

Irvine-Fynn, T. D., E. Sanz-Ablanedo, N. Rutter, M. W. Smith, and J. H. Chandler, 2014: Measuring glacier surface roughness using plot-scale, close-range digital photogrammetry. *Journal of Glaciology*, **60 (223)**, 957–969, doi:10.3189/2014JoG14J032.

James, M. R., and S. Robson, 2012: Straightforward reconstruction of 3D surfaces and topography with a camera: Accuracy and geoscience application. *Journal of Geophysical Research: Earth Surface*, **117 (3)**, 1–17, doi:10.1029/2011JF002289.

James, M. R., and S. Robson, 2014: Mitigating systematic error in topographic models derived from UAV and ground-based image networks. *Earth Surface Processes and Landforms*, **39 (10)**, 1413–1420, doi:10.1002/esp.3609.

James, M. R., S. Robson, and M. W. Smith, 2017: 3-D uncertainty-based topographic change detection with structure-from-motion photogrammetry: precision maps for ground control and directly georeferenced surveys. *Earth Surface Processes and Landforms*, **42 (12)**, 1769–1788, doi:10.1002/esp.4125.

Jouvet, G., Y. Weidmann, E. van Dongen, M. P. Lüthi, A. Vieli, and J. C. Ryan, 2019: High-Endurance UAV for Monitoring Calving Glaciers: Application to the Inglefield Bredning and Eqip Sermia, Greenland. *Frontiers in Earth Science*, **7**, 206, doi:10.3389/feart.2019.00206.

Karner, F., F. Obleitner, T. Krismer, J. Kohler, and W. Greuell, 2013: A decade of energy and mass balance investigations on the glacier Kongsvegen, Svalbard. *Journal of Geophysical Research Atmospheres*, **118 (10)**, 3986–4000, doi:10.1029/2012JD018342.

Kraaijenbrink, P., S. W. Meijer, J. M. Shea, F. Pellicciotti, S. M. De Jong, and W. W. Immerzeel, 2016: Seasonal surface velocities of a Himalayan glacier derived by automated correlation of unmanned aerial vehicle imagery. *Annals of Glaciology*, **57 (71)**, 103–113, doi:10.3189/2016AoG71A072.

Lettau, H., 1969: Note on aerodynamic roughness-parameter estimation on the basis of roughness-element description. *Journal of applied meteorology*, **8 (5)**, 828–832.

Liestøl, O., 1993: Satellite image atlas of glaciers of the world: Glaciers of Europe - Glaciers of Svalbard, Norway. *U.S. Geological Survey Professional*, 127–151, doi:10.1017/S0954102089260273.

Luckman, A., 2020: Svalbard 2019 Glacier Velocity Map. Accessed on: 2020-09-14, URL https://adrianluckman.wordpress.com/svalbard-2019-glacier-velocity-map/.

Luckman, A., D. I. Benn, F. Cottier, S. Bevan, F. Nilsen, and M. Inall, 2015: Calving rates at tidewater glaciers vary strongly with ocean temperature. *Nature Communications*, **6 (1)**, 1–7, doi:10.1038/ncomms9566.

Macdonald, R. W., R. F. Griffiths, and D. J. Hall, 1998: An improved method for the estimation of surface roughness of obstacle arrays. *Atmospheric Environment*, **32 (11)**, 1857–1864, doi:10.1016/S1352-2310(97)00403-2.

Mallalieu, J., J. L. Carrivick, D. J. Quincey, M. W. Smith, and W. H. James, 2017: An integrated Structure-from-Motion and time-lapse technique for quantifying ice-margin dynamics. *Journal of Glaciology*, **63 (242)**, 937–949, doi:10.1017/jog.2017.48.

Mansell, D., A. Luckman, and T. Murray, 2012: Dynamics of tidewater surge-type glaciers in northwest Svalbard. *Journal of Glaciology*, **58 (207)**, 110–118, doi:10.3189/2012JoG11J058.

MET Norway, 2020: The Norwegian Meteorological Institute. Accessed on: 2020-08-10, URL https://seklima.met.no/observations/.

Miles, E. S., J. F. Steiner, and F. Brun, 2017: Highly variable aerodynamic roughness length (z0) for a hummocky debris-covered glacier. *Journal of Geophysical Research: Atmospheres*, **122 (16)**, 8447–8466, doi:10.1002/2017JD026510.

Munro, D. S., 1989: Surface roughness and bulk heat transfer on a glacier: comparison with eddy correlation. *Journal of Glaciology*, **35 (121)**, 343–348, doi:10.1017/S0022143000009266.

Nex, F., and F. Remondino, 2014: UAV for 3D mapping applications: A review. *Applied Geomatics*, **6 (1)**, 1–15, doi:10.1007/s12518-013-0120-x.

Nicholson, L. I., M. Pętlicki, B. Partan, and S. MacDonell, 2016: 3-D surface properties of glacier penitentes over an ablation season, measured using a Microsoft Xbox Kinect. *Cryosphere*, **10 (5)**, 1897–1913, doi:10.5194/tc-10-1897-2016.

Nield, J. M., R. C. Chiverrell, S. E. Darby, J. Leyland, L. H. Vircavs, and B. Jacobs, 2013a: Complex spatial feedbacks of tephra redistribution, ice melt and surface roughness modulate ablation on tephra covered glaciers. *Earth Surface Processes and Landforms*, **38 (1)**, 95–102, doi:10.1002/esp.3352.

Nield, J. M., and Coauthors, 2013b: Estimating aerodynamic roughness over complex surface terrain. *Journal of Geophysical Research: Atmospheres*, **118 (23)**, 12 948–12 961, doi:10.1002/2013JD020632.

Nuth, C., J. Kohler, M. König, A. Von Deschwanden, J. O. Hagen, A. Kääb, G. Moholdt, and R. Pettersson, 2013: Decadal changes from a multi-temporal glacier inventory of Svalbard. *Cryosphere*, **7 (5)**, 1603–1621, doi:10.5194/tc-7-1603-2013.

Obleitner, F., 2000: The energy budget of snow and ice at Breidamerkurjokull, Vatnajokull, Iceland. *Boundary-Layer Meteorology*, **97 (3)**, 385–410, doi:10.1023/A:1002734303353.

Obukhov, A. M., 1971: Turbulence in an atmosphere with a non-uniform temperature. *Boundary-Layer Meteorology*, **2 (1)**, 7–29, doi:10.1007/BF00718085.

Quincey, D., M. Smith, D. Rounce, A. Ross, O. King, and C. Watson, 2017: Evaluating morphological estimates of the aerodynamic roughness of debris covered glacier ice. *Earth Surface Processes and Landforms*, **42 (15)**, 2541–2553, doi:10.1002/esp.4198.

Radic, V., B. Menounos, J. Shea, N. Fitzpatrick, M. A. Tessema, and S. J. Déry, 2017: Evaluation of different methods to model near-surface turbulent fluxes for a mountain glacier in the Cariboo Mountains, BC, Canada. *Cryosphere*, **11 (6)**, 2897–2918, doi:10.5194/tc-11-2897-2017.

Rees, W. G., and N. S. Arnold, 2006: Scale-dependent roughness of a glacier surface: Implications for radar backscatter and aerodynamic roughness modelling. *Journal of Glaciology*, **52 (177)**, 214–222, doi:10.3189/172756506781828665.

Rossini, M., B. Di Mauro, R. Garzonio, G. Baccolo, G. Cavallini, M. Mattavelli, M. De Amicis, and R. Colombo, 2018: Rapid melting dynamics of an alpine glacier with repeated UAV photogrammetry. *Geomorphology*, **304**, 159–172, doi:10.1016/j.geomorph.2017.12.039.

Rounce, D. R., D. J. Quincey, and D. C. McKinney, 2015: Debris-covered glacier energy balance model for Imja-Lhotse Shar Glacier in the Everest region of Nepal. *Cryosphere*, **9 (6)**, 2295–2310, doi:10.5194/tc-9-2295-2015.

Ryan, J. C., A. L. Hubbard, J. E. Box, J. Todd, P. Christoffersen, J. R. Carr, T. O. Holt, and N. Snooke, 2015: UAV photogrammetry and structure from motion to assess calving dynamics at Store Glacier, a large outlet draining the Greenland ice sheet. *Cryosphere*, **9 (1)**, 1–11, doi:10.5194/tc-9-1-2015.

Sauter, T., and S. P. Galos, 2016: Effects of local advection on the spatial sensible heat flux variation on a mountain glacier. *The Cryosphere*, **10 (6)**, 2887, doi:10.5194/tc-2016-139.

Schuler, T. V., and Coauthors, 2020: Reconciling Svalbard Glacier Mass Balance. *Frontiers in Earth Science*, **8**, 156, doi:10.3389/feart.2020.00156.

Shepard, M. K., B. A. Campbell, M. H. Bulmer, T. G. Farr, L. R. Gaddis, and J. J. Plaut, 2001: The roughness of natural terrain: A planetary and remote sensing perspective. *Journal of Geophysical Research: Planets*, **106 (E12)**, 32 777–32 795, doi:10.1029/2000JE001429.

Smeets, C. J., P. G. Duynkerke, and H. F. Vugts, 1999: Observed wind profiles and turbulence fluxes over an ice surface with changing surface roughness. *Boundary-Layer Meteorology*, **92 (1)**, 101–123, doi:10.1023/a:1001899015849.

Smith, B. E., C. F. Raymond, and T. Scambos, 2006: Anisotropic texture of ice sheet surfaces. *Journal of Geophysical Research: Earth Surface*, **111 (F01019)**, 1–8, doi:10.1029/2005JF000393.

Smith, M., J. Carrivick, and D. Quincey, 2016a: Structure from motion photogrammetry in physical geography. *Progress in Physical Geography: Earth and Environment*, **40 (2)**, 247–275, doi:10.1177/0309133315615805.

Smith, M. W., 2014: Roughness in the Earth Sciences. *Earth-Science Reviews*, **136**, 202–225, doi:10.1016/j.earscirev.2014.05.016.

Smith, M. W., D. J. Quincey, T. Dixon, R. G. Bingham, J. L. Carrivick, T. D. L. Irvine-Fynn, and D. M. Rippin, 2016b: Aerodynamic roughness of glacial ice surfaces derived from high-resolution topographic data. *Journal of Geophysical Research: Earth Surface*, **121**, 748–766, doi:10.1002/2015JF003759.

Smith, T., and Coauthors, 2020: A scale-dependent model to represent changing aerodynamic roughness of ablating glacier ice based on repeat topographic surveys. *Journal of Glaciology*, 1–15, doi:10.1017/jog.2020.56.

Steiner, J. F., M. Litt, E. E. Stigter, J. Shea, M. F. Bierkens, and W. W. Immerzeel, 2018: The Importance of Turbulent Fluxes in the Surface Energy Balance of a Debris-Covered Glacier in the Himalayas. *Frontiers in Earth Science*, **6**, 144, doi:10.3389/feart.2018.00144.

Uysal, M., A. S. Toprak, and N. Polat, 2015: DEM generation with UAV Photogrammetry and accuracy analysis in Sahitler hill. *Measurement: Journal of the International Measurement Confederation*, **73**, 539–543, doi:10.1016/j.measurement.2015.06.010.

Vacca, G., A. Dessì, and A. Sacco, 2017: The Use of Nadir and Oblique UAV Images for Building Knowledge. *ISPRS International Journal of Geo-Information*, **6 (12)**, 393, doi:10.3390/ijgi6120393.

Van Der Veen, C. J., 1996: Tidewater calving. *Journal of Glaciology*, **42 (141)**, 375–385, doi:10.3189/s0022143000004226.

Verhoeven, G., 2011: Taking computer vision aloft - archaeological three-dimensional reconstructions from aerial photographs with photoscan. *Archaeological Prospection*, **18 (1)**, 67–73, doi:10.1002/arp.399.

Walczykowski, P., K. Siok, and A. Jenerowicz, 2016: Methodology for determining optimal exposure parameters of a hyperspectral scanning sensor. *The International Archives of Photogrammetry, Remote Sensing and Spatial Information Sciences*, Prague, Czech Republic, Vol. XLI-B1, 1065, doi:10.5194/isprsarchives-XLI-B1-1065-201.

Wiernga, J., 1993: Representative roughness parameters for homogeneous terrain. *Boundary-Layer Meteorology*, **63 (4)**, 323–363, doi:10.1007/BF00705357.

Appendix A

Agisoft Metashape Processing Parameters

Processing parameters of Agisoft Metashape to build the DEM of Nordenskiöldbreen 2019 using SfM photogrammetry.

General	
Cameras	4024
Aligned cameras	4022
Coordinate system	WGS 84 (EPSG::4326)
Rotation angles	Yaw, Pitch, Roll
Point Cloud	
Points	1,334,300 of 1,571,748
RMS reprojection error	0.144689 (0.950551 pix)
Max reprojection error	3.61879 (63.1191 pix)
Mean key point size	6.15607 pix
Point colors	3 bands, uint8
Key points	No
Average tie point multiplicity	12.1747
Alignment parameters	
Accuracy	Medium
Generic preselection	Yes
Reference preselection	Source
Key point limit	40,000
Tie point limit	4,000
Guided image matching	No
Adaptive camera model fitting	Yes
Matching time	4 hours 6 minutes
Matching memory usage	2.36 GB
Alignment time	8 hours 1 minutes
Alignment memory usage	5.73 GB
Optimization parameters	
Parameters	f, b1, b2, cx, cy, k1-k4, p1, p2
Adaptive camera model fitting	No
Optimization time	47 minutes 13 seconds
Software version	1.6.2.10247
Depth Maps	
Count	1603
Depth maps generation parameters	
Quality	Medium
Filtering mode	Aggressive
Processing time	1 days 14 hours
Software version	1.6.2.10247
Dense Point Cloud	
Points	158,251,379
Point colors	3 bands, uint8
Depth maps generation parameters	
Quality	Medium
Filtering mode	Aggressive
Processing time	1 days 14 hours
Dense cloud generation parameters	
Processing time	3 hours 47 minutes
Software version	1.6.2.10247
Model	
Faces	25,210
Vertices	13,460

Vertex colors	3 bands, uint8
Reconstruction parameters	
Surface type	Height field
Source data	Sparse cloud
Interpolation	Enabled
Strict volumetric masks	No
Processing time	1 minutes 12 seconds
Software version	1.6.2.10247
DEM	
Size	18,122 x 17,318
Coordinate system	WGS 84 (EPSG::4326)
Reconstruction parameters	
Source data	Dense cloud
Interpolation	Enabled
Processing time	4 minutes 59 seconds
Software version	1.6.2.10247
Orthomosaic	
Size	52,158 x 43,503
Coordinate system	WGS 84 (EPSG::4326)
Colors	3 bands, uint8
Reconstruction parameters	
Blending mode	Mosaic
Surface	DEM
Enable hole filling	Yes
Processing time	1 hours 54 minutes
Software version	1.6.2.10247
System	
Software name	Agisoft Metashape Professional
Software version	1.6.3 build 10732
OS	Windows 64 bit
RAM	127.78 GB
CPU	Intel(R) Core(TM) i9-9900K CPU @ 3.60GHz
GPU(s)	GeForce RTX 2080

Processing parameters of Agisoft Metashape to build the DEM of Tunabreen using SfM photogrammetry.

General	
Cameras	2552
Aligned cameras	1595
Markers	4
Coordinate system	WGS 84 (EPSG::4326)
Rotation angles	Yaw, Pitch, Roll
Point Cloud	
Points	931,296 of 1,037,277
RMS reprojection error	0.132774 (1.03688 pix)
Max reprojection error	0.629585 (44.0592 pix)
Mean key point size	7.00054 pix
Point colors	3 bands, uint8
Key points	No
Average tie point multiplicity	6.58923
Alignment parameters	
Accuracy	Medium
Generic preselection	Yes
Reference preselection	Source
Key point limit	40,000
Tie point limit	4,000
Guided image matching	No
Adaptive camera model fitting	Yes
Matching time	47 minutes 51 seconds
Matching memory usage	939.46 MB
Alignment time	12 minutes 0 seconds
Alignment memory usage	782.41 MB
Optimization parameters	
Parameters	f, b1, b2, cx, cy, k1-k3, p1, p2
Adaptive camera model fitting	No
Optimization time	46 seconds
Software version	1.6.1.10009
Depth Maps	
Count	1595
Depth maps generation parameters	
Quality	Medium
Filtering mode	Aggressive
Processing time	7 hours 21 minutes
Software version	1.6.1.10009
Dense Point Cloud	
Points	140,270,731
Point colors	3 bands, uint8
Depth maps generation parameters	
Quality	Medium
Filtering mode	Aggressive
Processing time	7 hours 21 minutes
Dense cloud generation parameters	
Processing time	1 hours 9 minutes
Software version	1.6.1.10009
Model	
Faces	17,600

Vertices	9,311
Vertex colors	3 bands, uint8
Reconstruction parameters	
Surface type	Height field
Source data	Sparse cloud
Interpolation	Enabled
Strict volumetric masks	No
Processing time	22 seconds
Software version	1.6.1.10009
DEM	
Size	20,015 x 17,819
Coordinate system	WGS 84 (EPSG::4326)
Reconstruction parameters	
Source data	Dense cloud
Interpolation	Enabled
Processing time	2 minutes 55 seconds
Software version	1.6.1.10009
Orthomosaic	
Size	66,723 x 57,247
Coordinate system	WGS 84 (EPSG::4326)
Colors	3 bands, uint8
Reconstruction parameters	
Blending mode	Mosaic
Surface	DEM
Enable hole filling	Yes
Processing time	1 hours 16 minutes
Software version	1.6.3.10732
System	
Software name	Agisoft Metashape Professional
Software version	1.6.3 build 10732
OS	Windows 64 bit
RAM	127.78 GB
CPU	Intel(R) Core(TM) i9-9900K CPU @ 3.60GHz
GPU(s)	GeForce RTX 2080

Processing parameters of Agisoft Metashape to build the DEM of Heuglinbreen using SfM photogrammetry.

General	
Cameras	621
Aligned cameras	620
Coordinate system	WGS 84 (EPSG::4326)
Rotation angles	Yaw, Pitch, Roll
Point Cloud	
Points	243,548 of 284,343
RMS reprojection error	0.147481 (0.914086 pix)
Max reprojection error	0.53496 (24.0897 pix)
Mean key point size	5.96371 pix
Point colors	3 bands, uint8
Key points	No
Average tie point multiplicity	9.55508
Alignment parameters	
Accuracy	Medium
Generic preselection	Yes
Reference preselection	Source
Key point limit	40,000
Tie point limit	4,000
Guided image matching	No
Adaptive camera model fitting	Yes
Matching time	17 minutes 50 seconds
Matching memory usage	375.88 MB
Alignment time	2 minutes 44 seconds
Alignment memory usage	334.07 MB
Optimization parameters	
Parameters	f, b1, b2, cx, cy, k1-k4, p1, p2
Adaptive camera model fitting	No
Optimization time	10 seconds
Software version	1.6.1.10009
Depth Maps	
Count	549
Depth maps generation parameters	
Quality	Medium
Filtering mode	Aggressive
Processing time	3 hours 16 minutes
Software version	1.6.1.10009
Dense Point Cloud	
Points	50,761,120
Point colors	3 bands, uint8
Depth maps generation parameters	
Quality	Medium
Filtering mode	Aggressive
Processing time	3 hours 16 minutes
Dense cloud generation parameters	
Processing time	17 minutes 9 seconds
Software version	1.6.1.10009
Model	
Faces	7,724
Vertices	4,261

Vertex colors	3 bands, uint8
Reconstruction parameters	
Surface type	Height field
Source data	Sparse cloud
Interpolation	Enabled
Strict volumetric masks	No
Processing time	10 seconds
Software version	1.6.1.10009
DEM	
Size	15,334 x 9,358
Coordinate system	WGS 84 (EPSG::4326)
Reconstruction parameters	
Source data	Dense cloud
Interpolation	Enabled
Processing time	1 minutes 10 seconds
Software version	1.6.1.10009
Orthomosaic	
Size	43,284 x 26,167
Coordinate system	WGS 84 (EPSG::4326)
Colors	3 bands, uint8
Reconstruction parameters	
Blending mode	Mosaic
Surface	DEM
Enable hole filling	Yes
Processing time	12 minutes 16 seconds
Software version	1.6.1.10009
System	
Software name	Agisoft Metashape Professional
Software version	1.6.3 build 10732
OS	Windows 64 bit
RAM	127.78 GB
CPU	Intel(R) Core(TM) i9-9900K CPU @ 3.60GHz
GPU(s)	GeForce RTX 2080

Processing parameters of Agisoft Metashape to build the DEM of Fridtjovbreen using SfM photogrammetry.

General	
Cameras	1198
Aligned cameras	1198
Markers	3
Coordinate system	WGS 84 (EPSG::4326)
Rotation angles	Yaw, Pitch, Roll
Point Cloud	
Points	701,262 of 832,456
RMS reprojection error	2.32841 (12.0113 pix)
Max reprojection error	3628.6 (13754.9 pix)
Mean key point size	8.47778 pix
Point colors	3 bands, uint8
Key points	No
Average tie point multiplicity	5.4151
Alignment parameters	
Accuracy	Medium
Generic preselection	Yes
Reference preselection	Source
Key point limit	40,000
Tie point limit	4,000
Guided image matching	No
Adaptive camera model fitting	Yes
Matching time	33 minutes 21 seconds
Matching memory usage	599.27 MB
Alignment time	13 minutes 56 seconds
Alignment memory usage	523.17 MB
Optimization parameters	
Parameters	f, b1, b2, cx, cy, k1-k3, p1, p2
Adaptive camera model fitting	No
Optimization time	17 seconds
Software version	1.6.3.10732
Depth Maps	
Count	653
Depth maps generation parameters	
Quality	Medium
Filtering mode	Aggressive
Processing time	9 minutes 43 seconds
Software version	1.6.3.10732
Dense Point Cloud	
Points	48,218,254
Point colors	3 bands, uint8
Depth maps generation parameters	
Quality	Medium
Filtering mode	Aggressive
Processing time	9 minutes 43 seconds
Dense cloud generation parameters	
Processing time	12 minutes 32 seconds
Software version	1.6.3.10732
Model	
Faces	13,281

Vertices	7,056
Vertex colors	3 bands, uint8
Reconstruction parameters	
Surface type	Height field
Source data	Sparse cloud
Interpolation	Enabled
Strict volumetric masks	No
Processing time	7 seconds
Software version	1.6.3.10732
DEM	
Size	10,965 x 9,546
Coordinate system	WGS 84 (EPSG::4326)
Reconstruction parameters	
Source data	Dense cloud
Interpolation	Enabled
Processing time	54 seconds
Software version	1.6.3.10732
Orthomosaic	
Size	32,948 x 32,155
Coordinate system	WGS 84 (EPSG::4326)
Colors	3 bands, uint8
Reconstruction parameters	
Blending mode	Mosaic
Surface	DEM
Enable hole filling	Yes
Processing time	37 minutes 15 seconds
Software version	1.6.3.10732
System	
Software name	Agisoft Metashape Professional
Software version	1.6.3 build 10732
OS	Windows 64 bit
RAM	127.78 GB
CPU	Intel(R) Core(TM) i9-9900K CPU @ 3.60GHz
GPU(s)	GeForce RTX 2080

Processing parameters of Agisoft Metashape to build the DEM of Nordenskiöldbreen 2020 using SfM photogrammetry.

General	
Cameras	2028
Aligned cameras	2028
Markers	5
Coordinate system	WGS 84 (EPSG::4326)
Rotation angles	Yaw, Pitch, Roll
Point Cloud	
Points	901,913 of 1,104,521
RMS reprojection error	0.129253 (0.862926 pix)
Max reprojection error	0.603684 (39.2067 pix)
Mean key point size	6.11689 pix
Point colors	3 bands, uint8
Key points	No
Average tie point multiplicity	7.67305
Alignment parameters	
Accuracy	Medium
Generic preselection	Yes
Reference preselection	Source
Key point limit	40,000
Tie point limit	4,000
Guided image matching	No
Adaptive camera model fitting	Yes
Matching time	9 minutes 56 seconds
Matching memory usage	1.06 GB
Alignment time	24 minutes 42 seconds
Alignment memory usage	999.07 MB
Optimization parameters	
Parameters	f, b1, b2, cx, cy, k1-k3, p1, p2
Adaptive camera model fitting	No
Optimization time	48 seconds
Software version	1.6.3.10732
Depth Maps	
Count	1141
Depth maps generation parameters	
Quality	Medium
Filtering mode	Aggressive
Processing time	18 minutes 1 seconds
Software version	1.6.3.10732
Dense Point Cloud	
Points	107,510,109
Point colors	3 bands, uint8
Depth maps generation parameters	
Quality	Medium
Filtering mode	Aggressive
Processing time	18 minutes 1 seconds
Dense cloud generation parameters	
Processing time	21 minutes 49 seconds
Software version	1.6.3.10732
Model	
Faces	15,778

Vertices	8,628
Vertex colors	3 bands, uint8
Reconstruction parameters	
Surface type	Height field
Source data	Sparse cloud
Interpolation	Enabled
Strict volumetric masks	No
Processing time	7 seconds
Software version	1.6.3.10732
DEM	
Size	10,936 x 18,575
Coordinate system	WGS 84 (EPSG::4326)
Reconstruction parameters	
Source data	Dense cloud
Interpolation	Enabled
Processing time	1 minutes 49 seconds
Software version	1.6.3.10732
Orthomosaic	
Size	33,117 x 64,534
Coordinate system	WGS 84 (EPSG::4326)
Colors	3 bands, uint8
Reconstruction parameters	
Blending mode	Mosaic
Surface	DEM
Enable hole filling	Yes
Processing time	28 minutes 41 seconds
Software version	1.6.3.10732
System	
Software name	Agisoft Metashape Professional
Software version	1.6.3 build 10732
OS	Windows 64 bit
RAM	127.78 GB
CPU	Intel(R) Core(TM) i9-9900K CPU @ 3.60GHz
GPU(s)	GeForce RTX 2080

Appendix B

Digital Elevation Models

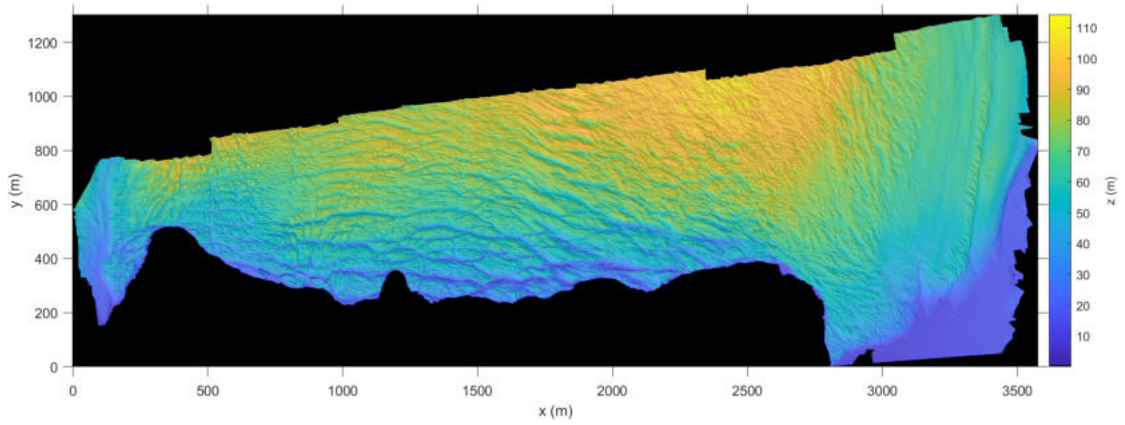

(a) Tunabreen

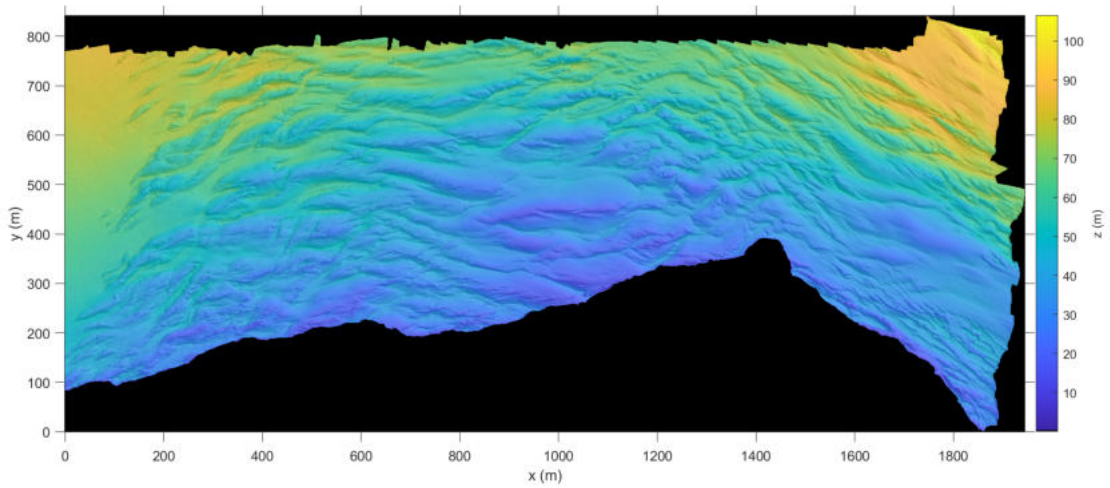

(b) Heuglinbreen

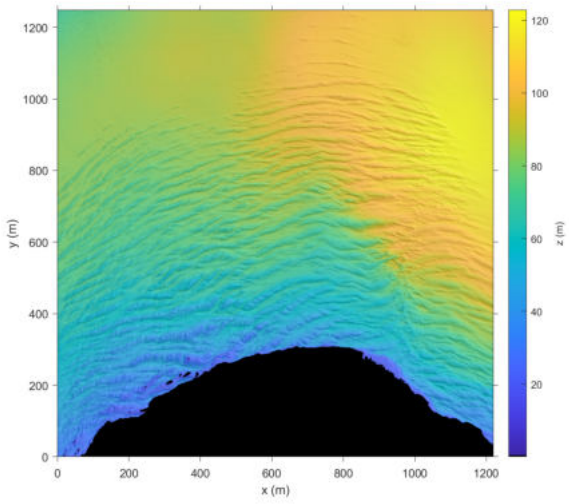

(c) Fridtjovbreen

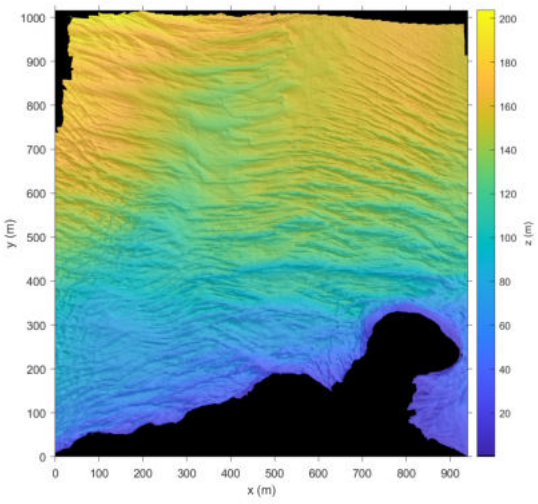

(d) Nordenskiöldbreen 2020

Figure B.1: DEM of the mapped glaciers Tunabreen (a), Heuglinbreen (b) Fridtjovbreen (c) and Nordenskiöldbreen 2020 (d) used for the z_0 calculation. The DEMs were built with a SfM approach using drone-based high resolution images. A hillshade layer was laid under the DEMs for a better visualization of the roughness elements.

Appendix C

Aerodynamic Roughness Length

Table C.1: Summary of z_0 values for each glacier and model in a down-glacier wind direction. The standard deviation (Std) and the interquantile-range (IQR) are two common parameters to estimate the spread of the z_0 values within the mapped area.

Glacier	Parameter	Smith	Chambers	Fitzpatrick	Munro	Lettau
Nordenskiöldbreen 2019	Mean (m)	0.129	0.151	0.126	0.393	0.496
	Std (m)	0.178	0.203	0.224	0.519	0.740
	IQR (m)	0.161	0.199	0.148	0.501	0.619
Tunabreen	Mean (m)	0.223	0.271	0.196	0.709	0.883
	Std (m)	0.272	0.331	0.273	0.87	1.157
	IQR (m)	0.293	0.346	0.253	0.932	1.184
Heuglinbreen	Mean (m)	0.150	0.187	0.175	0.415	0.424
	Std (m)	0.125	0.157	0.188	0.345	0.519
	IQR (m)	0.163	0.202	0.176	0.42	0.363
Fridtjovbreen	Mean (m)	0.082	0.098	0.115	0.248	0.276
	Std (m)	0.092	0.114	0.228	0.27	0.543
	IQR (m)	0.117	0.144	0.118	0.339	0.319
Nordenskiöldbreen 2020	Mean (m)	0.231	0.276	0.213	0.706	0.867
	Std (m)	0.229	0.273	0.277	0.644	0.856
	IQR (m)	0.239	0.289	0.209	0.774	0.953

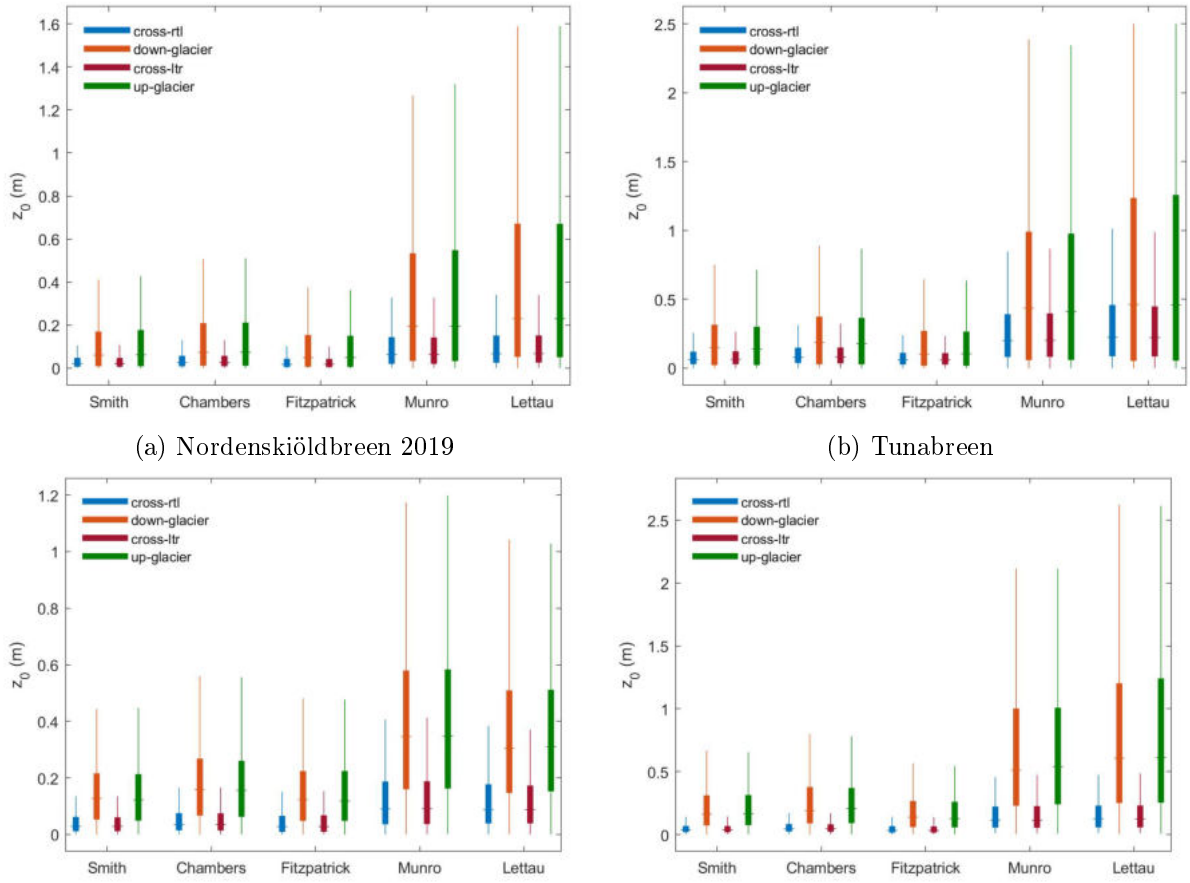

(a) Nordenskiöldbreen 2019

(b) Tunabreen

(c) Heuglinbreen

(d) Nordenskiöldbreen 2020

Figure C.1: Boxplot visualization of z_0 values for all four wind directions and each applied model determined on the glaciers Nordenskiöldbreen 2019 (a), Tunabreen (b), Heuglinbreen (c) and Nordenskiöldbreen 2020 (d).

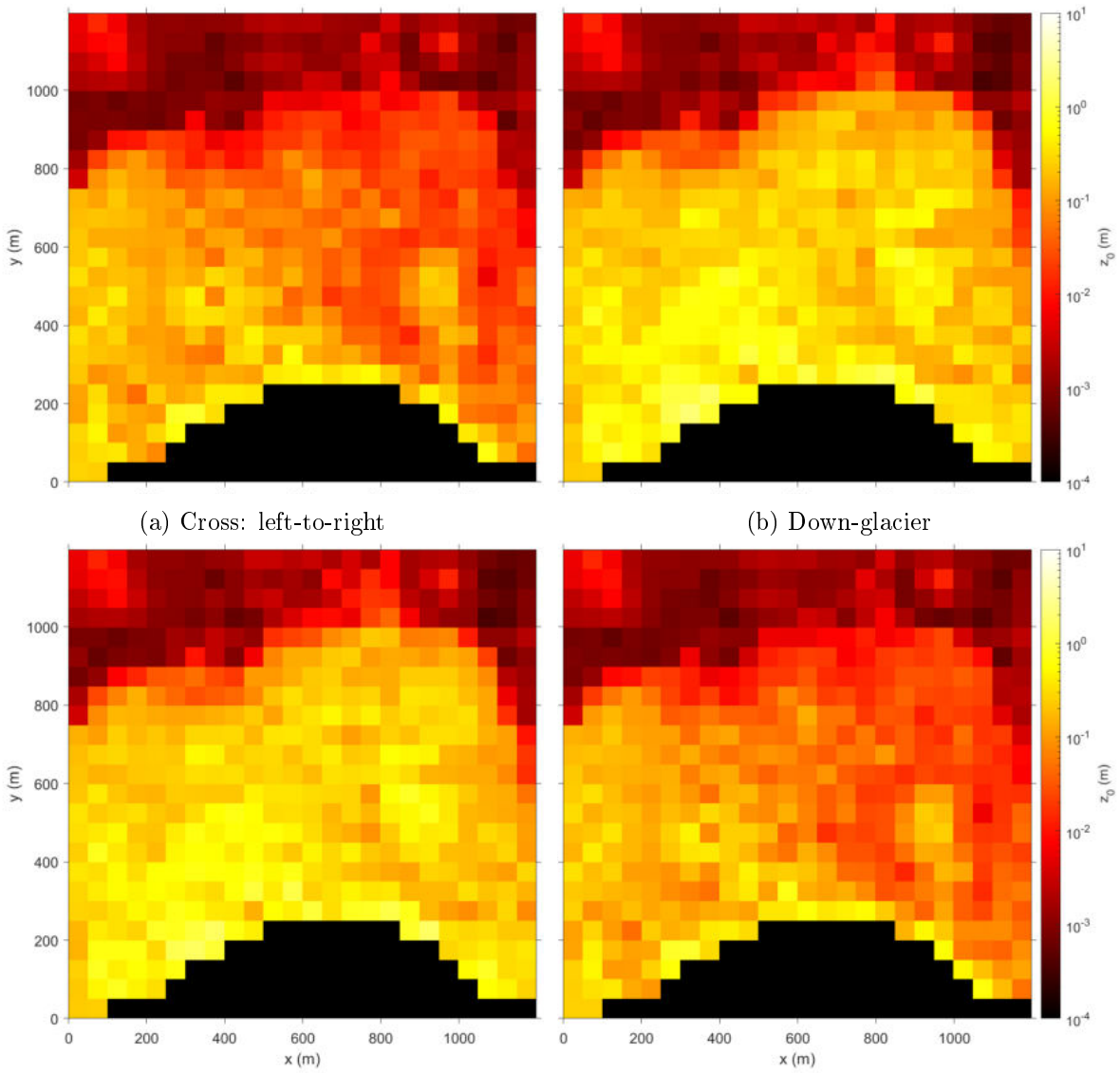

(a) Cross: left-to-right

(b) Down-glacier

(c) Up-glacier

(d) Cross: right-to-left

Figure C.2: Variability of z_0 values for Fridtjovbreen depending on the wind direction for a subarea grid size of 50 m calculated with the Munro model. Winds blowing across the glacier either from the left to right (a) or right to left (d) produce smaller z_0 values than down- (b) or up-glacier (c) winds.

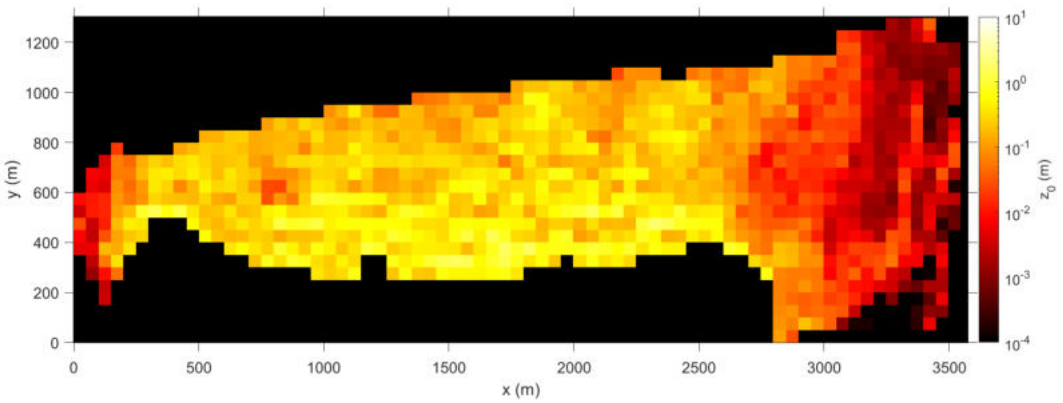

(a) Smith

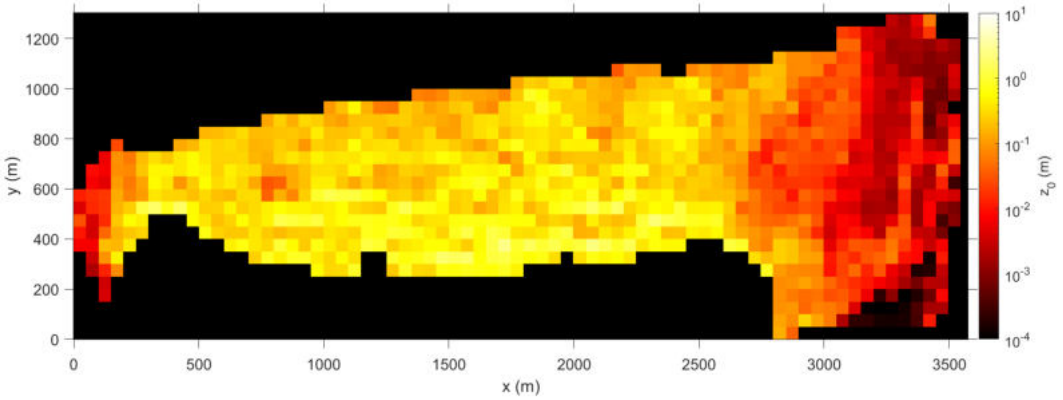

(b) Chambers

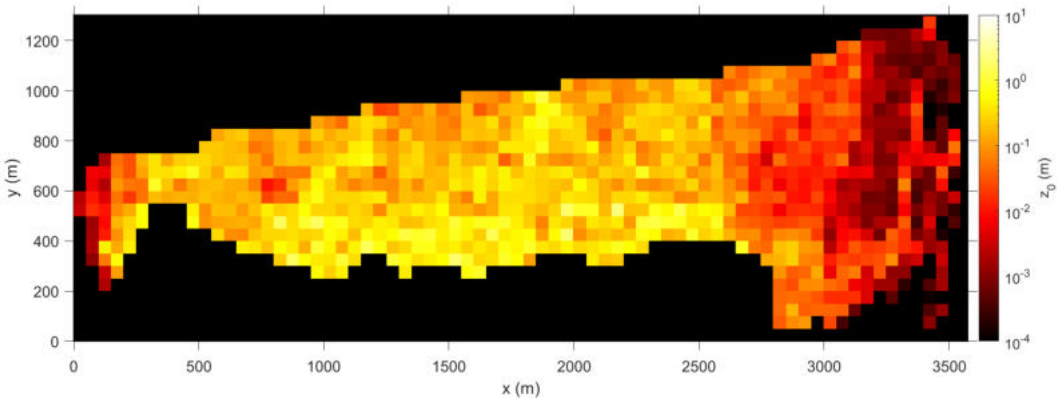

(c) Fitzpatrick

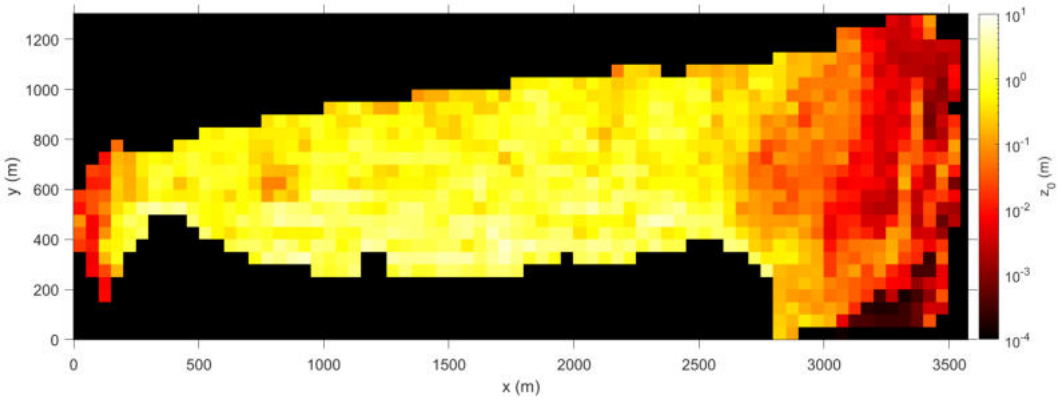

(d) Munro

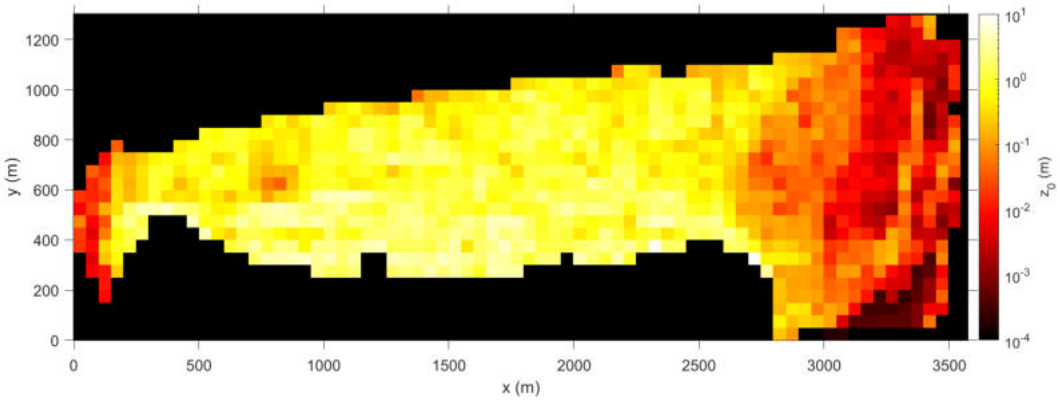

(e) Lettau

Figure C.4: Variability of z_0 values for Tunabreen depending on the calculation models Smith (a), Chambers (b), Fitzpatrick (c), Munro (d) and Lettau (e) for a subarea grid size of 50 m and a down-glacier wind direction.

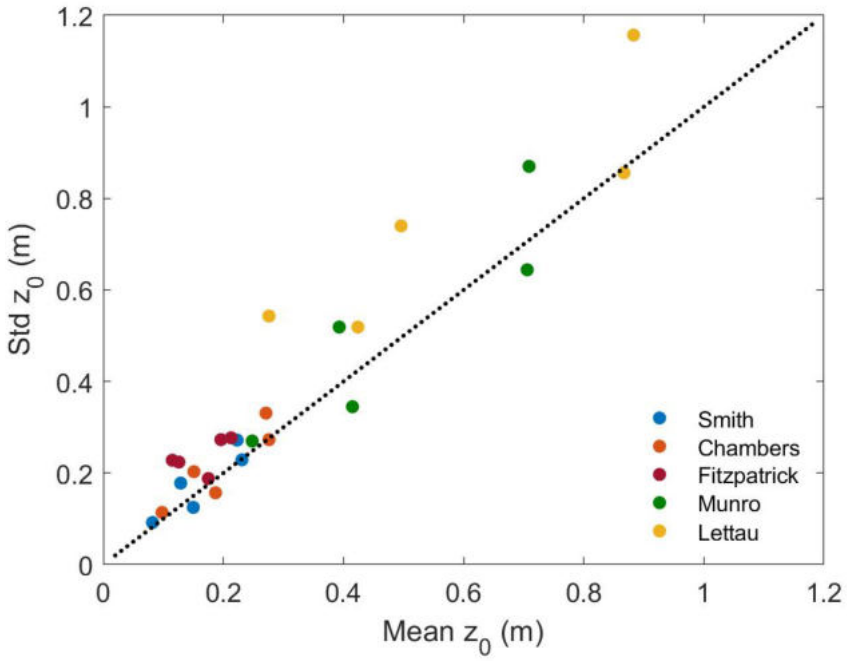

Figure C.5: Illustration of the relationship between the mean z_0 values (down-glacier wind direction) and the according standard deviation of all mapped glaciers for each model. The black dotted line refers to the 1:1 line.

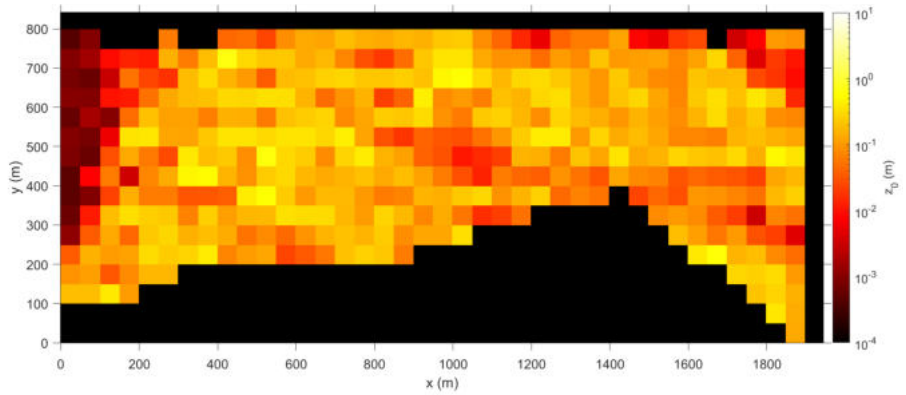

(a) Smith

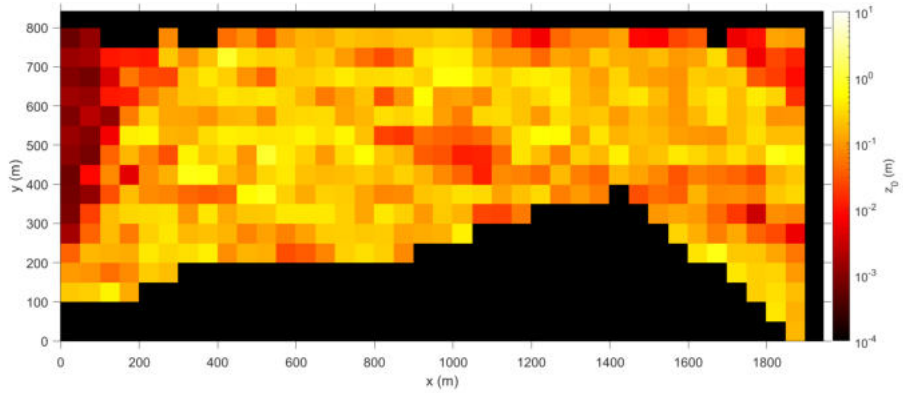

(b) Chambers

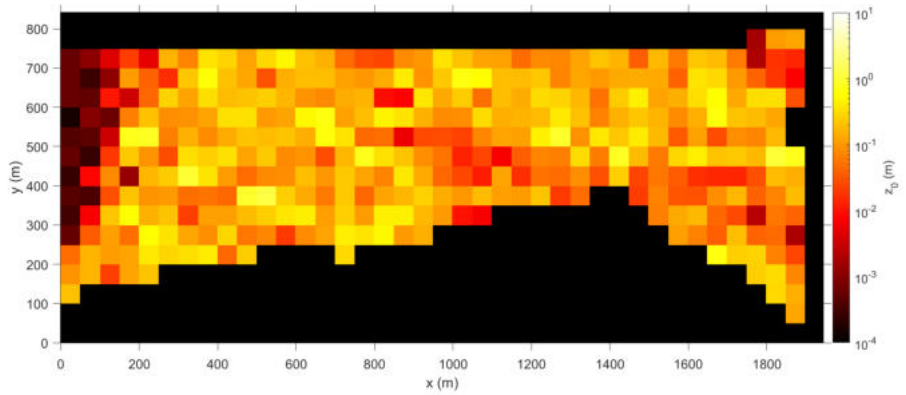

(c) Fitzpatrick

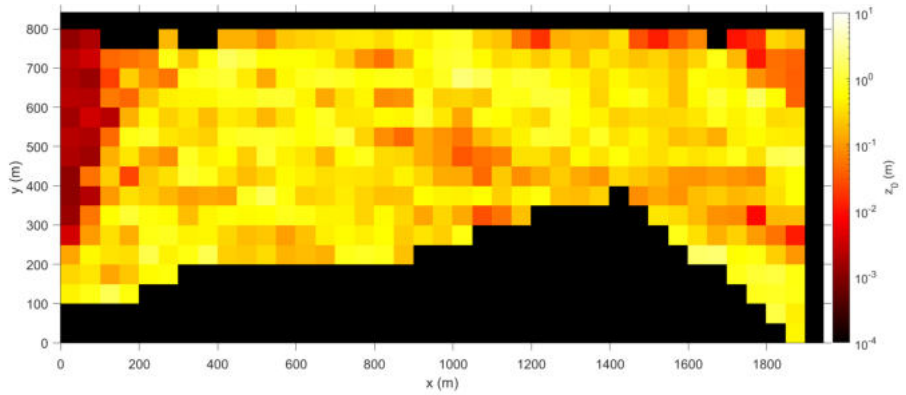

(d) Munro

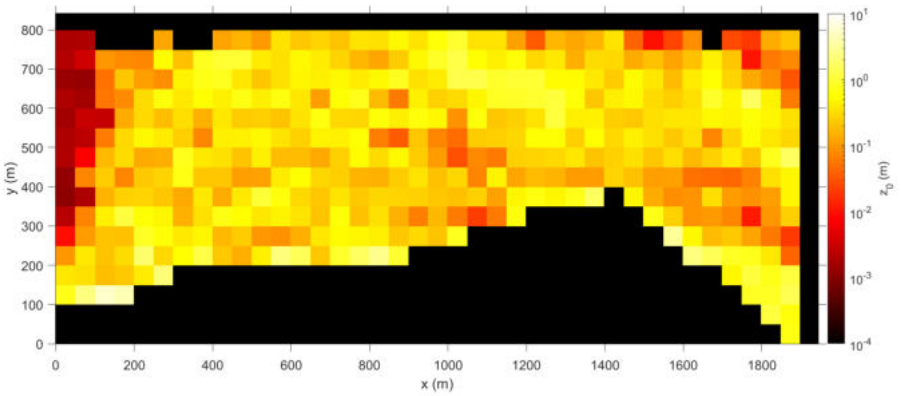

(e) Lettau

Figure C.7: Variability of z_0 values for Heuglinbreen depending on the calculation models Smith (a), Chambers (b), Fitzpatrick (c), Munro (d) and Lettau (e) for a subarea grid size of 50 m and a down-glacier wind direction.

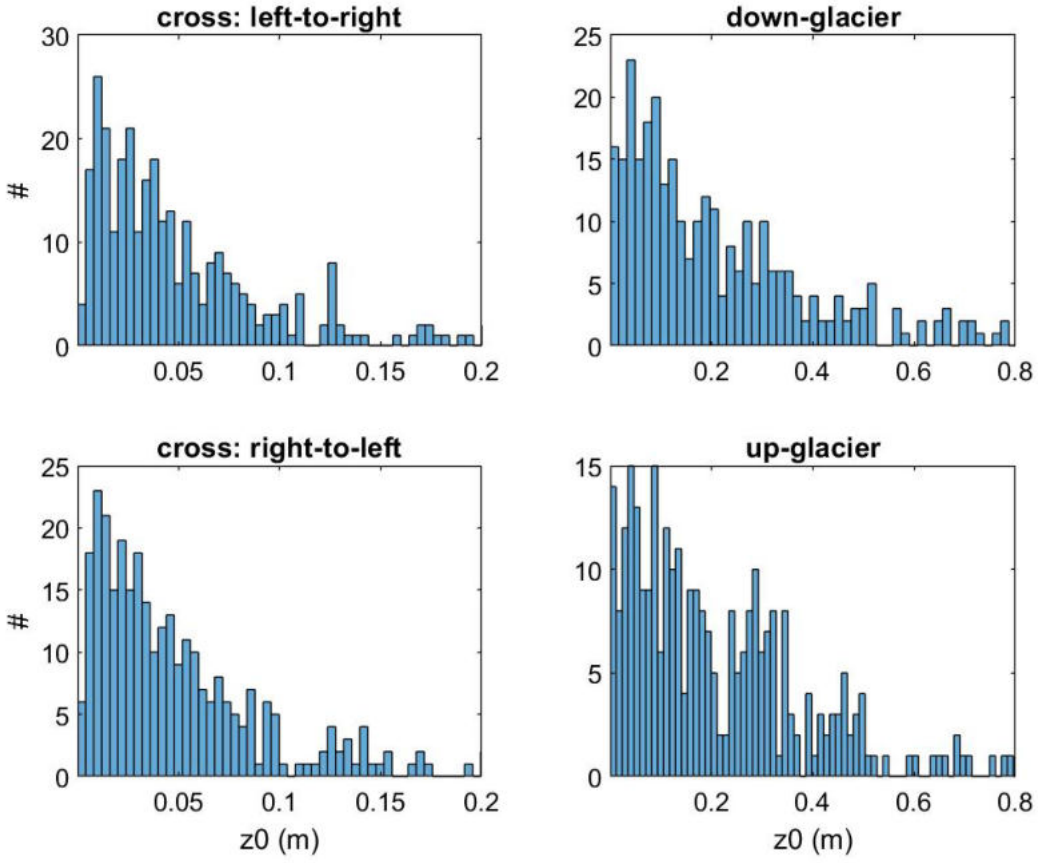

Figure C.8: Histogram of subarea z_0 values on Nordenskiöldbreen 2020 for each cardinal wind direction calculated with the Smith model.

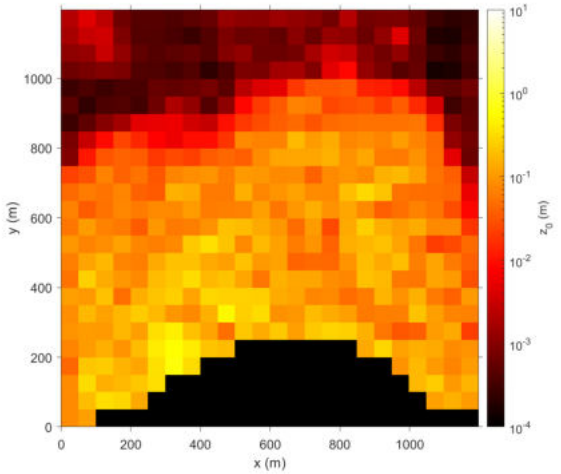

(a) Smith

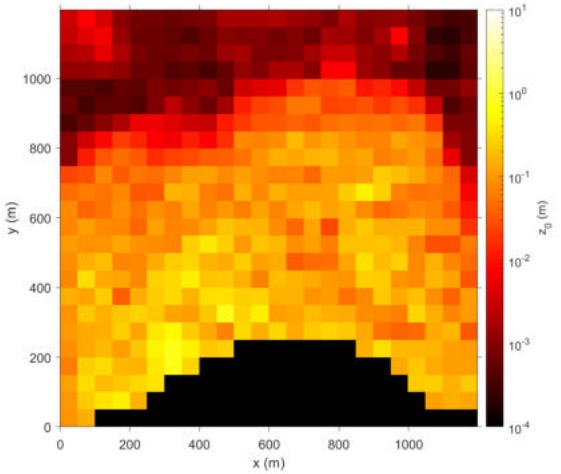

(b) Chambers

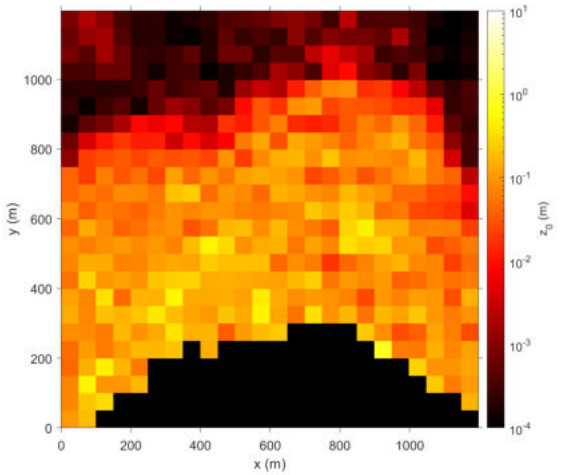

(c) Fitzpatrick

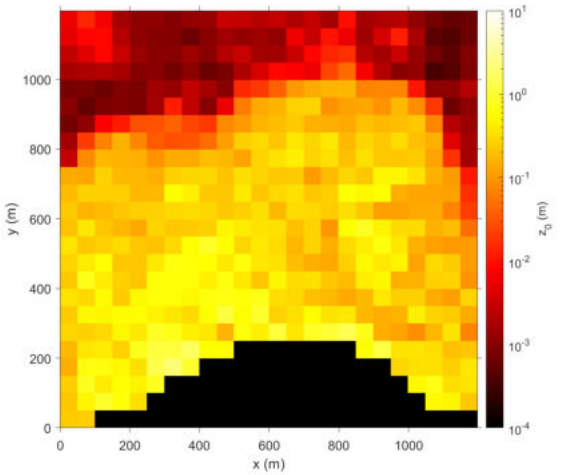

(d) Munro

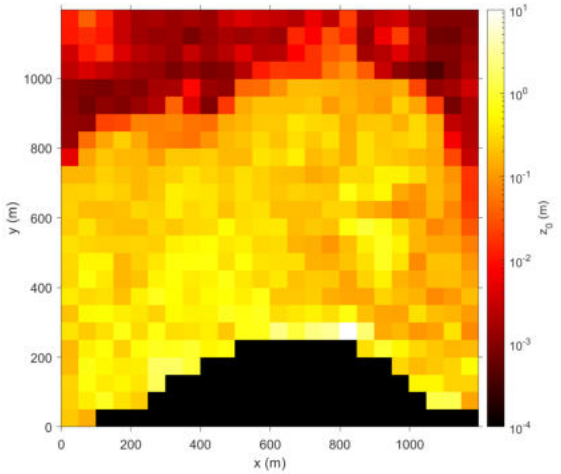

(e) Lettau

Figure C.9: Variability of z_0 values for Fridtjovbreen depending on the calculation models Smith (a), Chambers (b), Fitzpatrick (c), Munro (d) and Lettau (e) for a subarea grid size of 50 m and a down-glacier wind direction.

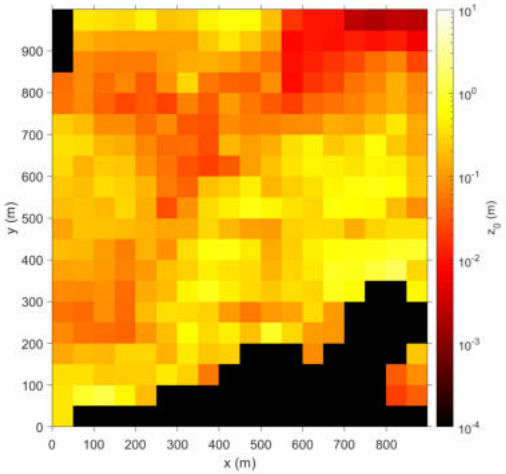

(a) Smith

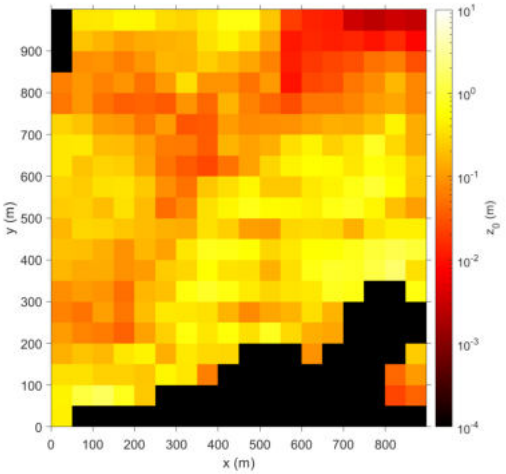

(b) Chambers

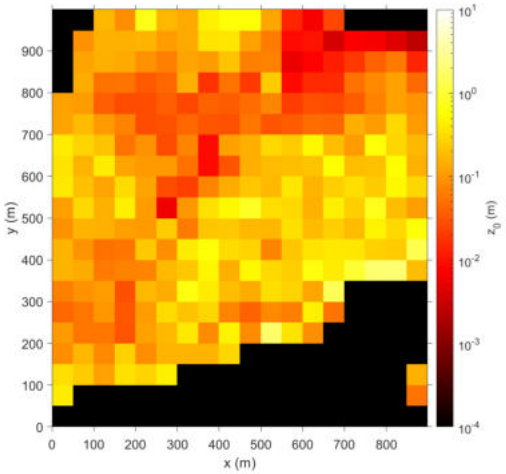

(c) Fitzpatrick

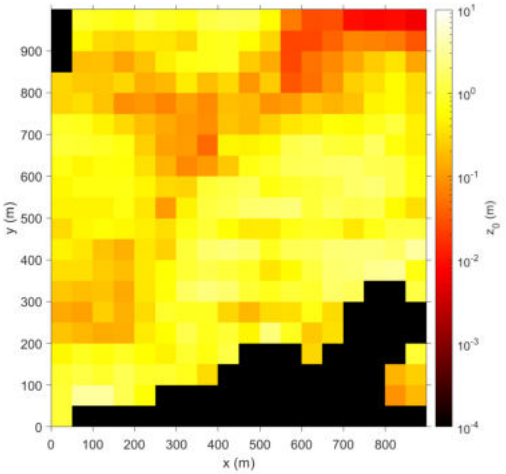

(d) Munro

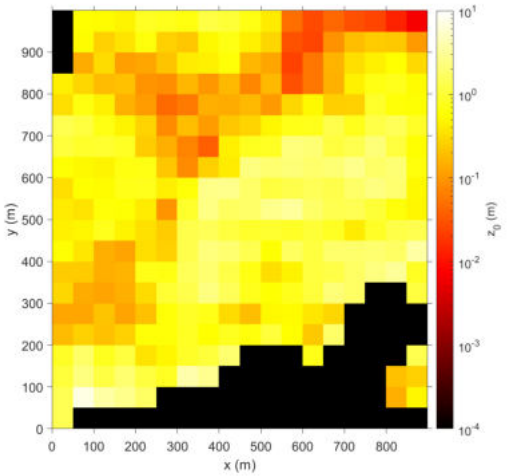

(e) Lettau

Figure C.10: Variability of z_0 values for Nordenskiöldbreen (2020) depending on the calculation models Smith (a), Chambers (b), Fitzpatrick (c), Munro (d) and Lettau (e) for a subarea grid size of 50 m and a down-glacier wind direction.

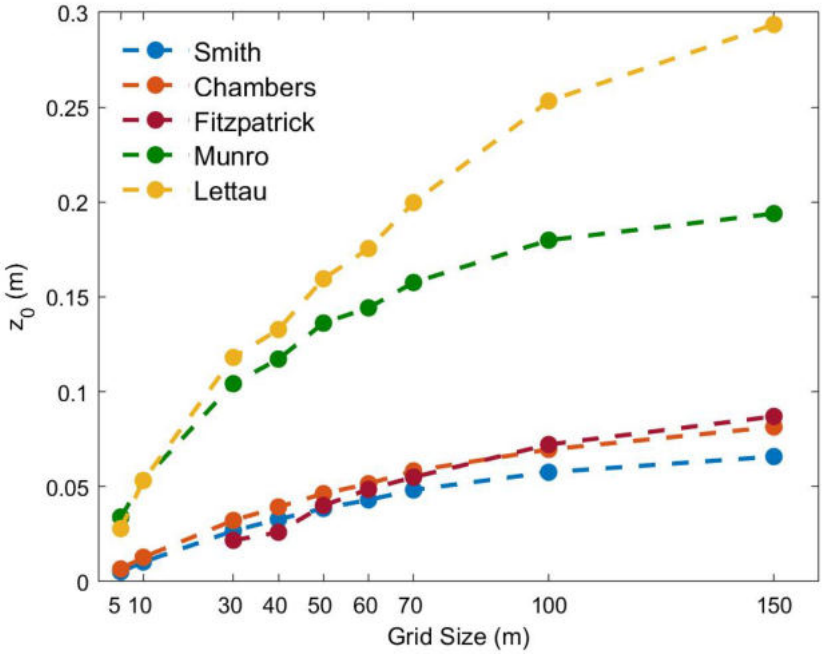

Figure C.11: Scale dependency of mean z_0 values of all five models for the cross-glacier wind direction (left-to-right) on Fridtjovbreen with chosen grid sizes from 5 m to 150 m. The z_0 values are increasing with larger subarea grid size independent of the chosen model.

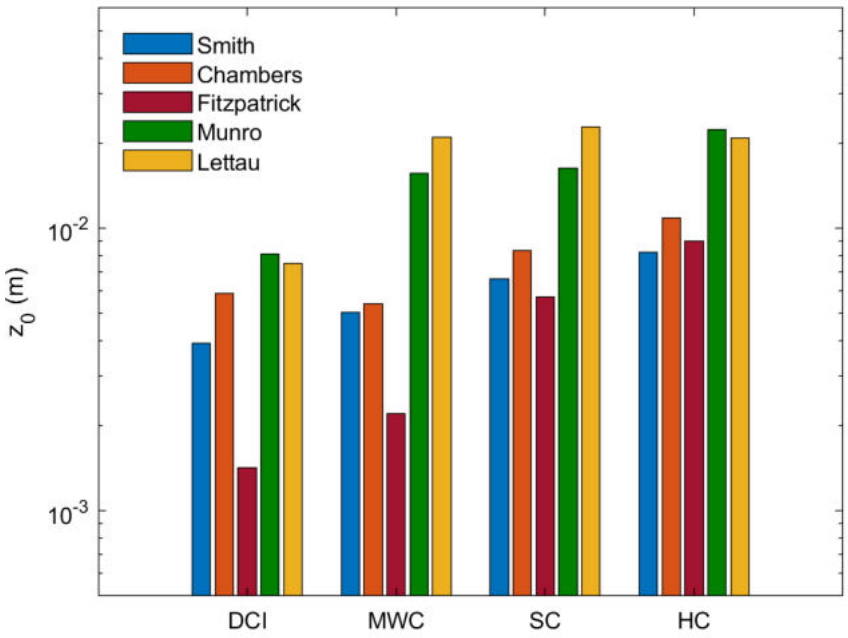

Figure C.12: Spatial variability of z_0 values for different surface features (plots of 50 m x 50 m) on Nordenskiöldbreen. For each model and for a cross-glacier (left-ro-right) wind direction the following surface characteristics were measured: debris-covered ice (DCI), melt water channel (MWC), slightly crevassed (SC) and heavily crevassed (HC) areas. Note the logarithmic scale on the y-axis.

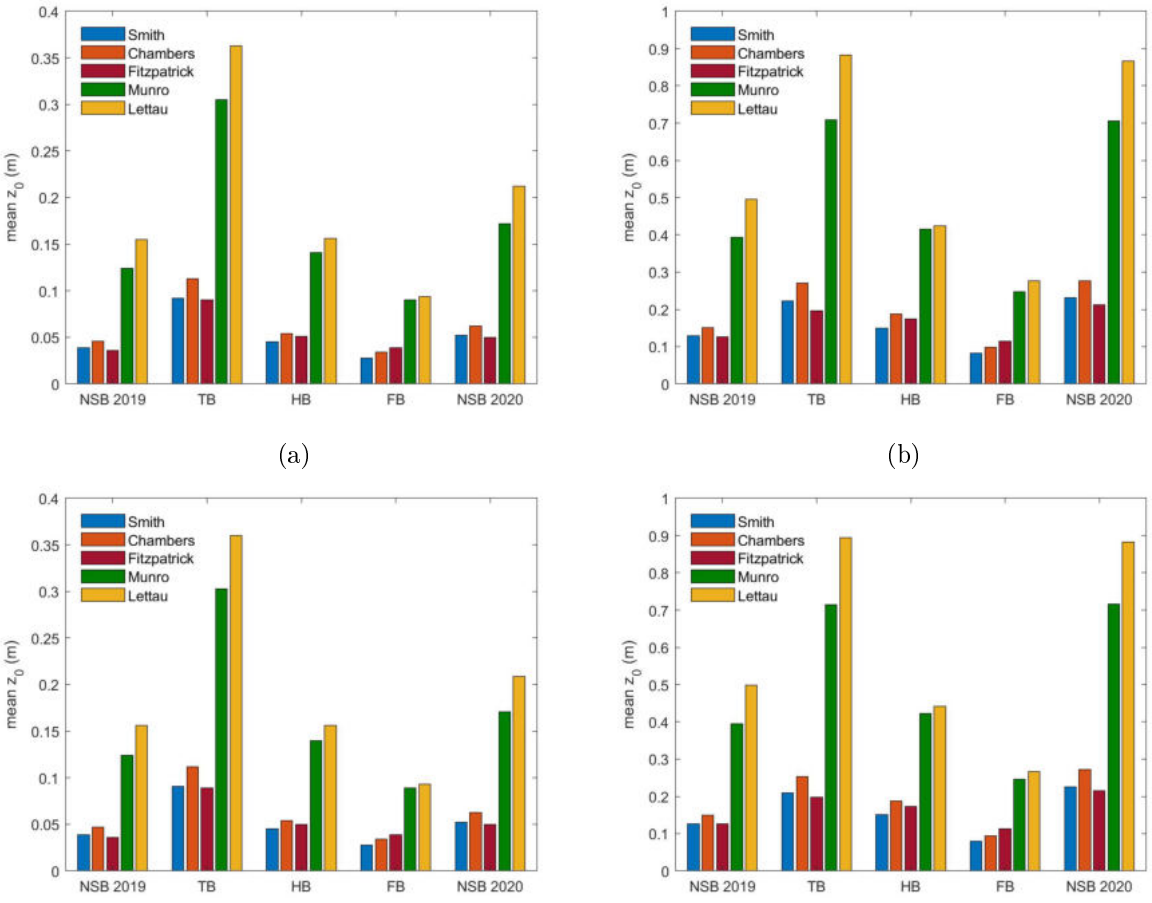

(a) (b)

(c) (d)

Figure C.13: Mean values of z_0 for the down-glacier wind direction applied for each model on Fridtjovbreen (FB), Heuglinbreen (HB), Tunabreen (TB) and Nordenskiöldbreen (NSB) in 2019 and 2020, respectively. The graphs ordered in cross-glacier left-to-right (a), down-glacier (b), cross-glacier right-to-left (c) and up-glacier (d) wind direction.

(a) (b)

Figure C.14: Drone picture of Heuglinbreen (a) and Nordenskiöldbreen 2020 (b) taken during fieldwork by Richard Hann.

Eidgenössische Technische Hochschule Zürich
Swiss Federal Institute of Technology Zurich

Declaration of originality

The signed declaration of originality is a component of every semester paper, Bachelor's thesis, Master's thesis and any other degree paper undertaken during the course of studies, including the respective electronic versions.

Lecturers may also require a declaration of originality for other written papers compiled for their courses.

I hereby confirm that I am the sole author of the written work here enclosed and that I have compiled it in my own words. Parts excepted are corrections of form and content by the supervisor.

Title of work (in block letters):

Authored by (in block letters):
For papers written by groups the names of all authors are required.

Name(s):	**First name(s):**

With my signature I confirm that

- I have committed none of the forms of plagiarism described in the 'Citation etiquette' information sheet.
- I have documented all methods, data and processes truthfully.
- I have not manipulated any data.
- I have mentioned all persons who were significant facilitators of the work.

I am aware that the work may be screened electronically for plagiarism.

Place, date	**Signature(s)**

For papers written by groups the names of all authors are required. Their signatures collectively guarantee the entire content of the written paper.